Micromechanical resonators with sub-micron gaps filled with high-k dielectrics

PAR

Mariazel de la Candelas MAQUEDA LÓPEZ

(EPFL

ÉCOLE POLYTECHNIQUE
FÉDÉRALE DE LAUSANNE

Suisse
2017

To the memory of my father.

To the memories with my mother.

Our hours are minutes when we think to know,
and centuries when we know what can be learnt.
— Antonio Machado

Nuestras horas son minutos cuando esperamos saber,
y siglos cuando sabemos lo que se puede aprender.
— Antonio Machado

Acknowledgements

First and foremost, I would like to thank my thesis advisor Prof. Adrian Mihai Ionescu for giving me the opportunity to pursue my Ph.D thesis in the NanoLab. During these years he has been always able to keep me on the right track with his guidance, support and kindness.

My gratitude also goes to Dr. Montserrat Fernández-Bolaños Badía, my thesis co-advisor. The enthusiasm that she has always shown towards every new challenge of this project has been a great lesson in motivation and perseverance. Without her advices and her will for excellence, this work would not have been possible.

I am also thankful to the members of my thesis committee, Prof. Jean-Michel Sallese and Prof. Guillermo Villanueva from EPFL, Dr. Fabio Coccetti and Dr. Daniel Grogg for reviewing the thesis and for their insightful comments and the interesting discussion on various aspects of my work that took place during its evaluation. Also, I would like to thank the members of my candidacy thesis committee, Prof. Alan Vachoux and Prof. Julian Perrusseau-Carrier from EPFL, who enlightened this work with their useful suggestions more than three years ago.

A special thank you goes to Prof. Noel Rodríguez Santiago from UGR, the first person who spoke me about Nanotechnology and involved me with research in the very far 2009, and to Prof. Mario Fernández Pantoja from UGR, who has always encouraged and advised me wisely. All my admiration goes to these two models of scientific researchers and human beings.

Another special and great thank goes to Dr. Igor Stolichnov and Dr. Hoël Maxime Guérin, who have always been helpful, kind and patient, willing to discuss with me in front of a paper and clear my doubts at any improvised moment, to Raymond Sutter, Karin Jaymes, Isabelle Buzzi and Lucie Auberson for their never-sufficiently-thanked logistic and administrative job and to my student Valliappan.

Acknowledgements

A large part of my work has been carried out at EPFL CMI cleanroom. There I have found a team of excellent professionals, able to look untiringly for fabrication solutions with me, and excellent persons, who often were able to remind me the intrinsic beauty that takes place between the walls of the cleanroom. My thoughts go especially to Dr. Zdenek Benes, Dr. Cyrille Hilbert and Giovanni Monteduro.

Sometimes Andrea. Most of the time Emanuele. Emanuele Andrea Casu. I have had the amazing luck to have shared my complete Ph.D journey with him. He has been synonym of work discussions, but also sense of humour and *savoir faire*. This important period of my life will be always intrinsically linked to him, and I could not be happier that it was like that.

I would like to thank all my colleagues at the NanoLab and our nanolunch partners, who have supported my research and/or myself during this work. Special mentions go to Dr. Livio Lattanzio, who mentored me during my first year (*arìsc vov ca l'erie ie fresch!*) and the years beyond our shared office term, and Nicolò Oliva, with whom I am lucky to share an astonishing affinity since we met in September.

I find no words to thank the unconditional support of my friends Cosimo, José Antonio, Lisa and Maria Teresa, whose presence in my life have blessed me during years, illuminating my bad days and making shining my good ones. You are my muses.

I would like to thank my amazing flatmates Antonio and Mathilde. Living together has made me happier and wiser, making possible the motto *these are the old good times*. There will be always a virtual Palud's window to share our confidences.

I feel lucky to have so many friends spread all over the world to whom I have the chance to render my thanks. Blanca, Borch, Chema, Danila, Espi, Eu, Fabian, Fedele (*il mio conoscente preferito*), Fernan (and Risky), Isabel, Jacopo, José, Jury, Marco, Massimo, Mino, Peppe, Rachele, Rena, Rodrigo (*el maestro*), Santi, Vlado and Xexu.

Thanks to the members of the ImproPas and the GTEL, I feel honoured to have shared with you so many stages. A special mention goes to Dr. Mauro Manassi, who, being close or far, is always able to make me start a laugh.

Abstract

Scaled microelectromechanical (MEMS) resonating devices have generated a great interest for their use in RF front-end architectures for wireless communication, channel-select filters, on-chip signal processing and timing and extreme mas sensing applications thanks to their robustness, low power consumption, easy integration with CMOS and multimode reconfigurability. Therefore, MEMS resonators are a promising alternative to various discrete electrical components, offering excellent figures of merit at in the HF/VHF frequency range. However, there are many remaining open challenges for the research on MEMS resonators such as high quality factor at high frequency, thermal stability, reduced motional resistance, frequency precision and stability, low phase noise and appropriate hermetical and low cost packaging.

Many advanced MEMS resonators use deep sub-micron air gaps (<100 nm) in order to improve the electrostatic coupling and, thus, to obtain low motional impedance levels. The lower limit to the gap size is set by fabrication methods, by vibration amplitude and/or by nonlinear effects such as intermodulation distortion. The free space electrode gap offers the advantage to nearly achieve perfect acoustic isolation due to large impedance discontinuity.

To overcome the inherent limitations of capacitive transductions, the use of gaps filled with high permittivity materials has been proposed as a way to enhance the electrostatic coupling. Solid and partially-filled high-k dielectric gap resonators have attracted a certain interest in comparison to the air-gap electrostatic transduction since they enhance the transduction efficiency and the electrical resonance current, reduce motional resistance and may even strengthen the suspended structures, making them more reliable for mass sensing applications.

During the course of this work, diverse microfabrication processes have been developed and realized in order to obtain air and partially-filled flexural and bulk resonators working in the

Abstract

HF/VHF range from frequencies between 5 MHz and 70 MHz. Benefiting from gap transduction enhancement coming from the gap-filling with high-k material such as hafnium oxide, the motional resistance has been reduced up to hundreds of Ohms and f_0xQ products of the order of $5 \cdot 10^{11}$ have been accomplished. A remarkable improvement in output signals has been obtained by the novel combination of high-k dielectric gap-filling and piezoresistive detection. We have reported some of the first experiments with partially-filled gaps flexural double-ended tuned fork (DETF) resonators and bulk wine-glass disk (WGD) resonators, piezoresistively sensed. Moreover, mass sensing experiments have been carried out by means of resonator mass loading with controlled Atomic Layer Deposition (ALD) of HfO_2 and experimental point mass sensitivities up to 4.816 kHz/pg have been derived. These preliminary results suggest that partially-filled gap MEMS resonators can be utilized to realize mass sensors in large range of masses and frequencies.

Key words: Micromechanical resonator, MEMS resonator, MEMS, microsystems, microfabrication, silicon on insulator, quality factor, resonance frequency, mass sensing, mass sensor, Atomic Layer Deposition (ALD), high-k dielectric, hafnium oxide.

Résumé

Les dispositifs microelectro-mécaniques (MEMS) résonants ont généré un grand intérêt pour leur utilité dans les architectures face avant RF pour la communication sans fil, les filtres sélecteurs de canaux, le traitement de signal sur puce, le chronométrage et leurs applications dans la détection de masses extrêmes grâce à leur robustesse améliorée, leur faible consommation électrique, leur intégration plus aisée au sein de circuits intégrés et leur reconfigurabilité multimode. Par conséquent, les résonateurs MEMS sont une alternative prometteuse à divers composants électriques discrets, qui offre d'excellents facteurs de mérite dans le domaine de fréquences HF/VHF. Cependant, ils reste de nombreux défis pour la recherche sur les résonateurs MEMS tels que le facteur de qualité en haute fréquence, la stabilité thermique, la réduction de la résistance au mouvement, la précision et stabilité fréquentielles, le bruit de phase et la création d'un emballage approprié, hermétique et peu coûteux.

Beaucoup de résonateurs MEMS utilisent des espaces d'air d'épaisseur inférieure au micron (<100 nm) afin d'améliorer le couplage électrostatique et par conséquent afin d'obtenir de faibles niveaux d'impédance. La finesse de l'espace est limitée par des difficultés de fabrication, par l'amplitude de vibration du résonateur et/ou par des effets non linéaires tels que la distorsion d'intermodulation. L'espace libre de l'électrode à espace présente l'avantage de presque atteindre une isolation acoustique parfaite grâce à une grande discontinuité dans l'impédance.

Pour dépasser les limitations inhérentes aux transductions capacitives, l'utilisation d'un matériau à permittivité élevée a été proposée comme un moyen d'améliorer le couplage électrostatique. Les résonateurs à espace solide et partiellement rempli de diélectrique à haut k ont suscité l'intérêt comparés aux transducteurs électrostatiques à espace d'air puisqu'ils améliorent l'efficacité de transduction et le courant de résonance électrique, réduisent la

résistance au mouvement et peuvent aussi renforcer les structures, les rendant plus fiables pour les applications de détection de masse.

Au cours de ce travail, plusieurs procédés de microfabrication ont été développés et réalisés afin d'obtenir des résonateurs à espace, à flexion partiellement remplis et des résonateurs massifs fonctionnants dans le domaine HF/VHF pour des fréquences comprises entre 5 MHz et 70 MHz. Bénéficiant de l'amélioration de la transduction de l'espace provenant du remplissage de l'espace par un matériau à constante diélectrique élevée tel que l'oxyde d'hafnium, la résistance au mouvement a été réduite jusqu'à quelques centaines d'Ohms et des produits f_0xQ de $5 \cdot 10^{11}$ ont été accomplis. Une amélioration remarquable dans les signaux de sortie a été obtenu par la nouvelle combinaison de remplissage d'espace avec un diélectrique à k élevé et la détection piézorésistive. Nous avons rendu compte de certaines des premières expériences avec des résonateurs à diapason à deux extrémités (DETF) flexibles à espace partiellement rempli et des résonateurs massifs en disque *verre de vin* à espace partiellement rempli mesurés de manière piézorésistive. De plus, des expériences de détection de masse ont été réalisées en chargeant en masse le résonateur par un procédé contrôlé de dépôt par couche atomique (ALD) de HfO_2 et des sensibilités de masse expérimentales jusqu'à 4.816 kHz/pg ont été obtenues. Ces résultats préliminaires montrent que les résonateurs MEMS à espace partiellement rempli peuvent être utilisés pour la réalisation de capteurs de masse pour de vastes domaines de masses et fréquences.

Mots clés: Résonateur micromécanique, résonateur MEMS, MEMS, microsystèmes, micro-fabrication, silicium sur isolant, facteur de qualité, fréquence de résonance, détection de masse, capteur de masse, déposition par couche atomique (ALD), diélectrique à k élevé, oxyde d'hafnium.

Contents

Contents

Contents

List of Figures

List of Tables

Glossary

AC   Alternate Current

AFM   Atomic Force Microscopy

AKE   Akhiezer Effect

ALD   Atomic Layer Deposition

BAW   Bulk Acoustic Wave

BOX   Buried Oxied

BVD   Butterworth-Van Dyke

BW   Bandwith

CCB   Clamped-Clamped Beam

CMOS   Complementary Metal-Oxide Semiconductor

CMR   Contour Mode Resonator

CNT   Carbon Nano Tube

CTE   Coefficient Thermal Expansion

DC   Direct Current

DETF   Double-Ended Tuning Fork

DMS   Distributed Mass Sensitivity

DMR   Distributed Mass Resolution

EMS   Experimental Mass Sensitivity

EPMS   Experimental Distributed Mass Sensitivity

EPMS   Experimental Point Mass Sensitivity

FBAR   Film Bulk Acoustic Resonator

FET   Field Effect Transistor

FEM   Finite Elements Method

FIB   Focused Ion Beam

FM   Frequency Modulated

FOM   Figure Of Merit

GND   Ground

GSG   Ground-Signal-Ground

HARS   High Aspect Ratio Structure

HF   High Frequency

IC   Integrated Circuit

IOT   Internet of Things

QCM   Quartz Crystal Microbalance

LI   Lock In

MEK   Methyl Ethyl Ketone

MEMS	Micro Electro Mechanical System
MOSFET	Metal Oxide Field Effect Transistor
NEMS	Nano Eletro Mecahnical System
PBR	Parallel Beam Resonator
PLL	Phase Lock Loop
PMM	Pulse Mode Mechanism
PMR	Point Mass Resolution
PMS	Point Mass Sensitivity
PVDF-TrFE	Polyvinylidene Fluoride-Trifluoroethylene
SAW	Surface Acoustic Wave
SEM	Scanning Electron Microscopy
SNR	Signal-to-Noise Ratio
SOI	Silicon On Insulator
SPD	Sensitive Photo Detector
SPR	Square Plate Resonator
RE	Relative Error
RF	Radio Frequency
RIE	Reactive Ion Etching
RLC	Resistance-Inductance-Capacitance
RT	Room Temperature
SEM	Scanning Electron Microscope
SMR	Solidly Mounted Resonator

SNR   Signal To Noise Ratio

SOI   Silicon On Insulator

SPR   Squared Plate Resonator

TCF   Temperature Coefficient of Frequency

TEMAH   etrakis(ethylmethylamino)hafnium

TFBAR   Thin-Film Acoustic Wave Resonator

TED   Thermo-Elastic Damping

UHF   Ultra High Frequency

VHF   Very High Frequency

VNA   Vector Network Analyser

WGD   Wine-Glass Disk

Symbols and Units

AC Bias Voltage	v_{ac}	V
Actuation Area	A	m^2
Air Damping	$\frac{1}{Q_{air}}$	-
Air Gap Width	g_{air}	m
AKE Damping	$\frac{1}{Q_{AKE}}$	-
Anchors Damping	$\frac{1}{Q_{anchors}}$	-
Anchor Length	l_a	m
Anchor Width	w_a	m
Angular Resonance Frequency	w_0	$\frac{rad}{s}$
Bandwidth	BW	Hz
Beam Length	l_b	m
Beams Number	N	-
Beam Width	w_b	m

Bessel's Function (first order)	$J_{(x)}$	-
Capacitance	C	F
Capacitive Output Current	i_{cap}	A
Charge	q	C
Characteristic Impedance	Z_0	Ω
Current	I	A
Damped Angular Resonance Frequency	w_d	$\frac{rad}{s}$
Damping	b	$\frac{kg}{s}$
Damping Ratio	ζ	-
DC Bias Voltage	V_{bias}	V
DC Bias Voltage (probe 1)	V_{DC1}	V
DC Bias Voltage (probe 2)	V_{DC2}	V
DC Bias Voltage (probe 3)	V_{DC3}	V
DC Bias Voltage (probe 4)	V_{DC4}	V
Dielectric Constant	ϵ	$\frac{F}{m}$
Displacement	x	m
Driving Force	F_d	N
Effective Area	A_{eff}	m^2
Effective Mass	m_{eff}	kg
Effective Spring Constant	k_{eff}	$\frac{N}{m}$
Elastic Force	$F_{elastic}$	N
Electrical Damping	$\frac{1}{Q_{electrical}}$	-

Electrical Spring Constant	k_{el}	$\frac{N}{m}$
Electrical Spring Constant (first order)	k_{el1}	$\frac{N}{m}$
Electrical Spring Constant (third order)	k_{el1}	$\frac{N}{m}$
Electrode Length	$l_{electrode}$	m
Electrode Length Factor	f_e	-
Electrostatic Force	$F_{electrostatic}$	N
Experimental Coefficient (CCB)	β_{CCB}	-
Experimental Coefficient (PBR)	β_{PBR}	-
Feedthrough Capacitance	C_0	F
Force	F	N
Force Amplitude	A_f	V
Fringing Field Correction Factor	c_f	-
Gap Capacitance	C_{gap}	F
Gap Width	g	m
Gauge Factor	GF	-
HfO$_2$ Gap Width	g_{HfO2}	m
Holes Width	w_h	m
Inductance	L	H
Input Coupling Factor	η_e, η_1	$\frac{C}{m}$
Inter-Beams Connection Length	l_m	m
Inter-Beams Connection Width	w_m	m
Inter-Holes Spacing	s	m

Internal Damping	$\frac{1}{Q_{internal}}$	-
Quality Factor	Q	-
Quality Factor (phase approximation)	Q_{ph}	-
Load Mass	m_{load}	kg
Longitudinal Piezoresistive Coefficient	π_L	$\frac{1}{Pa}$
Longitudinal Stress	σ_L	Pa
Magnetic Flux Linkage	λ	Wb
Mass	m	kg
Mass Density	ρ	$\frac{kg}{m^3}$
Mechanical Spring Constant	k_m	$\frac{N}{m}$
Mechanical Spring Constant (first order)	k_{m1}	$\frac{N}{m}$
Mechanical Spring Constant (third order)	k_{m3}	$\frac{N}{m}$
Moment of Inertia	I	$kg \cdot m^2$
Moment of Inertia of a CCB	I_{CCB}	$kg \cdot m^2$
Moment of Inertia of a DETF	I_{DETF}	$kg \cdot m^2$
Momentum	p	$\frac{kg \cdot m}{s}$
Motional Capacitance	C_m	F
Motional Inductance	L_m	H
Motional Resistance	R_m	Ω
Output Coupling Factor	η_r, η_2	$\frac{C}{m}$
Output Current	i_0	A
Phase	ϕ	$^\circ$

Piezoresistive Output Current	i_{res}	A
Plate Side	l_p	m
Poison's Ratio	ν	-
Pull-In Voltage	$V_{pull-in}^{two-port}$	V
Radius	R	m
Relative Dielectric Constant	ϵ_r	-
Resistance	R	Ω
Resistivity	ρ	$\Omega \cdot m$
Resonator Admittance	Y_{res}	S
Resonance Frequency	f_0	Hz
Resonator Resistance	R_{res}	Ω
Resonator Length	l_{res}	m
Shear Modulus	G	Pa
Shunt Capacitance	C_p	F
Spring Constant (Stiffness)	k	$\frac{N}{m}$
Stored Energy	E_{stored}	J
Surface Damping	$\frac{1}{Q_{surface}}$	-
TED Damping	$\frac{1}{Q_{TED}}$	-
Thickness	t	m
Tines Width	w_h	m
Tines Separation	l_h	m
Total Area	A_{total}	m^2

Total Force	F_{total}	N
Transmission Scattering Parameter	S_{21}	dB
Transversal Piezoresistive Coefficient	π_T	$\frac{1}{Pa}$
Transversal Stress	σ_L	Pa
Vacuum Permittivity	ϵ_0	$\frac{F}{m}$
Variable Gap Capacitance	C_{drive}	F
Velocity	u	$\frac{m}{s}$
Vertical-Collapse Voltage	$V_{vertical-collapse}$	V
Voltage	V	V
Wavelength	λ	m
Young's Modulus	E	Pa

1 Introduction

1.1 Motivation and Scope of the Thesis

Microelectromechanical systems (MEMS) technology enables the batch fabrication of miniature mechanical structures, devices and systems. It leverages the existing state-of-the-art of integrated circuits (ICs) fabrication technologies and exhibits dimensional downscaling and power consumption saving. In addition, by using materials such as silicon and fabrication techniques compatible with IC technology, MEMS devices can be monolithically integrated with electronics, giving rise to complete system-on-a-chip devices.

More specifically, MEMS resonators for radio frequency (RF) play an outstanding role among MEMS devices thanks to their very high resonance frequency versus quality factor Figure-of-Merit (FOM) , good temperature stability, low aging, tuneable capabilities and low power consumption. RF MEMS resonators have generated a tremendous interest for the development of fundamental building blocks in applications that include frequency reference, mixing, filtering and sensing.

RF MEMS resonators transform electrical signals into mechanical energy, perform a filtering function, and then transform the remaining mechanical energy into an electrical form. One of the most popular electromechanical transduction mechanism is based on capacitive air-gap transduction.

To overcome the inherent limitations of electromechanical coupling in air, the use of high dielectric materials in the gap has been proposed as a way to enhance the electrostatic coupling in the gaps. In addition, dielectric electrostatic transduction has benefits over common air-gap transduction, including the possibility to achieve smaller capacitance gaps and to prevent pull-in, stiction and dust or moisture issues present in air-gap devices. As gap-filling with a solid material would introduce acoustic losses because the solid material does not provide ideal impedance mismatch, partially-filled gap resonators have been proposed as a performance compromise.

During this work, the design, fabrication and characterization of air and partially-filled gap MEMS resonators has been undertaken, focusing on the study of flexural and bulk MEMS resonators with ALD HfO_2 as high-k gap-embedded material. The devices benefit from enhanced capacitive actuation due to the better coupling transduction in the partially-filled gaps and capacitive-piezoresistive readout with the aim of (a) improve the transduction coupling; (b) amplify the output capacitive current and (c) reduce the motional resistance. Furthermore, the fabricated MEMS could satisfy the demanding sensitivity and robustness requirements of mass sensors devices for consumer use in a close future.

1.2   Outline of the Manuscript

CHAPTER 2: MEMS RESONATORS BASIS AND STATE-OF-THE-ART

Chapter 2 presents a short introduction to MEMS devices, emphasizing the fundamental materials, fabrication processes and functionalities that this kind of devices have shown along the last years. A brief discussion about the main application fields where MEMS devices, and more specifically MEMS resonators, play a dominant role is included. A summary of the main characteristics and FOMs, modes of resonance and actuation and detection methods completes the introduction. The most recent state-of-the-art for flexural and bulk MEMS resonators with air, partially-filled and solid transduction gaps is reviewed and compared with the performances of the devices of this work. To finish, some examples of commercial MEMS resonators are included.

CHAPTER 3: ANALYTICAL MODELS AND SIMULATIONS

Chapter 3 details the analytical and Finite-Element-Methods (FEM) models that are used in the preliminary study of the flexural and bulk MEMS resonators that have been fabricated and whose characterization is described in Chapter 4. An exhaustive discussion about the existing agreement between them is fulfilled. Main resonators FOMs and actuation and detection methods are qualitatively studied, jointly with the nonlinearities generally present in MEMS resonators.

CHAPTER 4: DESIGN, FABRICATION AND CHARACTERIZATION

Chapter 4 reports the five flexural and bulk designs of the fabricated MEMS resonators (clamped-clamped beams, double-ended tuning forks, parallel-beams, disks and square plates resonators), providing the fabrication processes used to accomplish sub-micron air-gap and gaps partially-filled with high-k materials, which is based in Atomic Layer Deposition (ALD) of HfO_2. The complete characterization of the proposed designs is fulfilled for air-gap resonators, extracting and discussing their main motional parameters and their dependencies with the applied bias. Optical, capacitive and piezoresistive detection methods are compared to conclude that piezoresistive detection is the best readout. Finally, the impact of the gap-filling is detailed for flexural and bulk designs, and their performances are compared with their counterparts in air.

CHAPTER 5: MASS SENSING

Chapter 5 provides an analysis of the mass sensing performance shown by the MEMS resonators that have been theoretically studied and simulated (Chapter 3) and fabricated and characterized (Chapter 4). Comparisons between flexural and bulk resonators mass sensitivities extracted by means of FEM simulations and experimentally are discussed, revealing the promising perspective of partially-filled gap MEMS resonators for mass sensing.

CHAPTER 6: CONCLUSIONS

The last chapter of this manuscript summarises the major achievements obtained during this work and gives the expected future perspectives for partially-filled gap MEMS resonators in mass sensing applications.

2 MEMS Resonators Basis and State-of-the-art

During the last years, MEMS resonators have profited from the maturity of the existing fabrication techniques coming from the silicon industry and they have become fundamental devices in application fields as varied as communications, automotive, defence or bioapplications.

An extensive outlook on MEMS devices and more specifically MEMS resonators evolution is detailed in this chapter, taking into consideration materials, fabrication processes, modes of resonance, actuation and detection methods and main Figures-of-Merit (FOMs). The most recent state-of-the-art for flexural and bulk capacitive MEMS resonators present in academy are reviewed and compared with the devices presented in this work, revealing that the fabricated devices have FOMs comparable or beyond the recent published devices.

To finish, some of the current commercial RF MEMS resonators are discussed.

2.1 Microelectromechanical Systems (MEMS)

The acronym for microelectromechanical systems (MEMS) as it is used nowadays was officially adopted in 1989 in the Tele-Operated Robotics Workshop in Salt Lake City (Utah, USA)[1]. MEMS were defined as a process technology used to create miniaturised integrated devices that combine mechanical and electrical components in synergy. MEMS have the ability to sense, control and actuate on the micro scale, and generate effects on the macro scale. They are fabricated using integrated circuit (ICs) batch processing techniques and can range in size from a few micrometers to millimetres as it is illustrated in Figure 2.1.
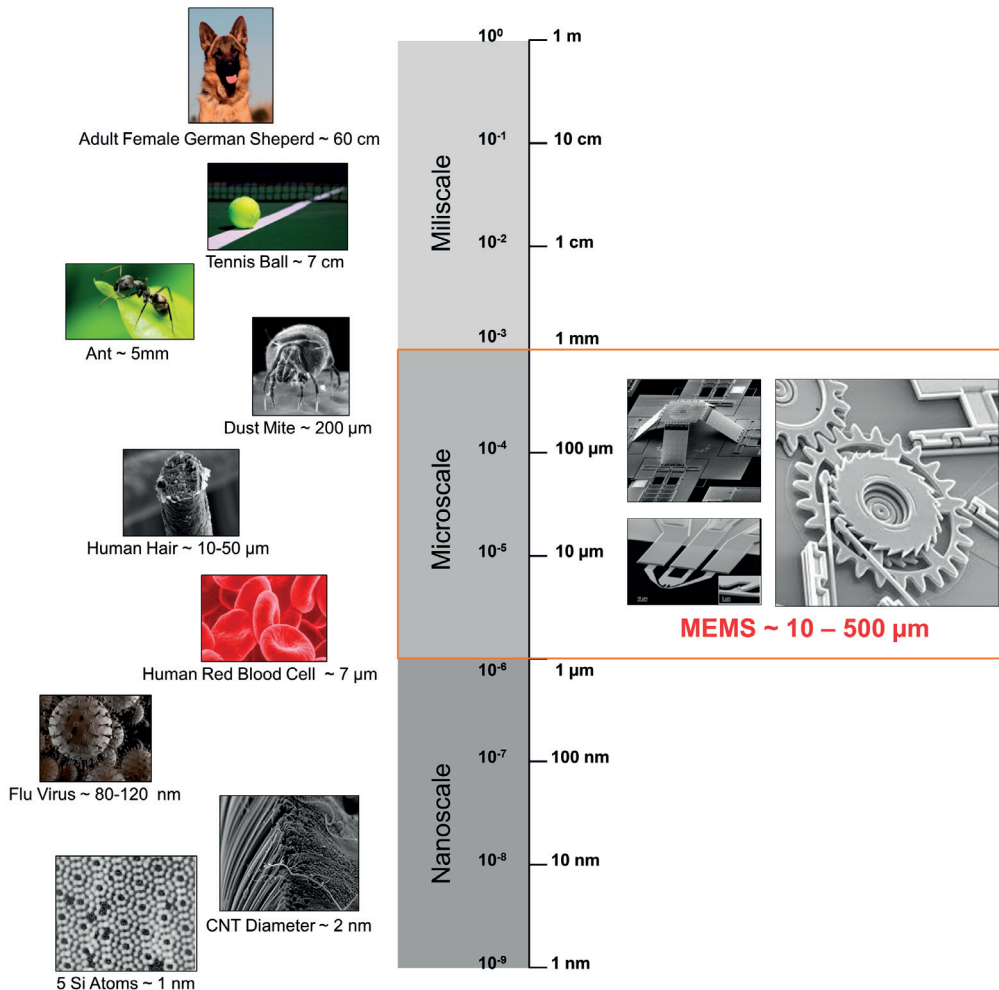
Figure 2.1 – Dimensional scale of MEMS devices.

The first microelectromecanical device was named *resonant gate transistor* and was presented in 1964 by Nathanson [2]. It was a suspended beam set into vibration by an electrostatic force

that modulated the current of a Field Effect Transistor (FET) by means of the displacement of its body (see Figure 2.2).
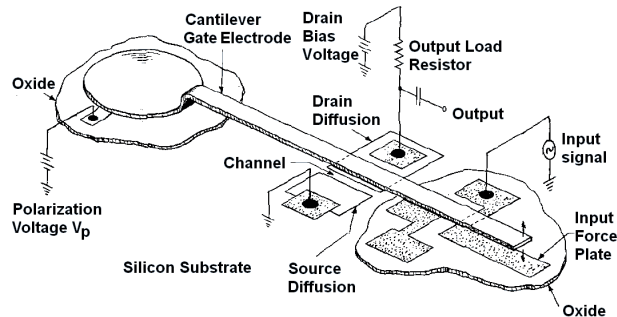
Figure 2.2 – Sketch of Nathanson's resonant gate transistor device [2].

From their birth, MEMS applications have profited from the maturity of the already existing fabrication techniques coming from the silicon industry. MEMS progress is resulted from the integration of electronics with mechanical components to produce high performance, low cost and high functionality integrated microsystems. Some of the advantages of MEMS devices are: 1) very small size, mass and volume; 2) very low power consumption; 3) low cost; 4) ease to be integrated into systems; 5) small thermal constant; 6) resistance to vibration, shock and radiation; 7) large fabrication batches; 8) improved thermal expansion tolerance and 9) parallelism. MEMS devices can vary from relatively simple structures having no moving elements to extremely complex electromechanical systems with multiple moving elements under the control of integrated microelectronics. The one main criterion of MEMS is that there are at least some elements having some sort of mechanical functionality whether or not these elements can move.

The complexity of MEMS resides in its natural interdisciplinarity that makes converge the design, engineering and manufacturing expertises from a wide range of technical areas. It includes not only electrical and mechanical engineering but integrated circuit fabrication technology, material science, optics, fluidics, biology, instrumentation and packaging, among others (see Figure 2.3).

The majority of MEMS devices must be combined with ICs for operation in larger electronic systems. ICs typically provide functionalities related to the signals of these transducers, such as analog-to-digital conversion, amplification, filtering and information processing as well as
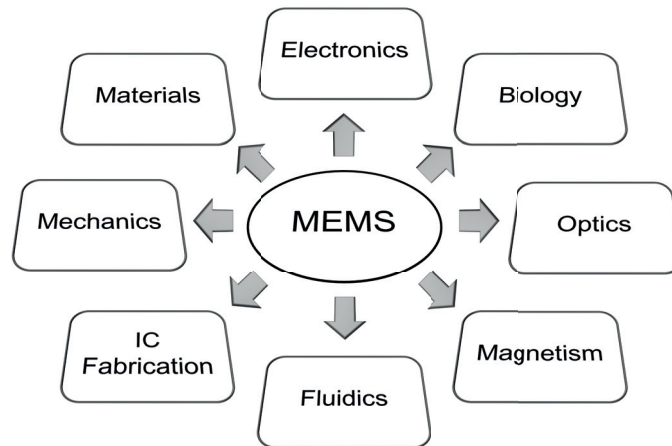
Figure 2.3 – Sciences for MEMS development.

communication between the MEMS transducer and their environment. Thus, the vast majority of commercial MEMS products, such as accelerometers, gyroscopes and micro-mirror arrays, are integrated and packaged together with ICs. This modular multichip implementation allows independent optimisation of MEMS and ICs. Nevertheless, cofabricated MEMS and ICs benefit from enhanced performance (noise, crosstalk and parasitics coming from interconnects, among others), smaller size and potentially lower cost. The main differences between ICs and MEMS technologies are listed in Table 2.1.

Table 2.1 – Comparison betweeen Intergrated Circuits and MEMS.

MEMS	Integrated Circuits
3D structures	2D structures
Ad hoc building blocks	Transistors in basic building blocks
May have moving parts	No moving parts
Interface with environment	Isolated
Multiple functions	Only electrical functions
Very complex packaging	Well developed packaging

2.1.1 Materials used in MEMS Fabrication

Single-crystal silicon is the most widely used substrate material in MEMS fabrication. The popularity of silicon for such application is primarily due to: 1) its mechanical stability, which makes possible their integration with electronics on the same substrate; 2) its linear relationship between the applied load and the induced deformations; 3) its high melting

point (1400°C), which makes silicon dimensionally stable even at elevated temperature; 4) its coefficient of thermal expansion (CTE) is about 8 times smaller than that of steel and more than 10 times smaller than that of aluminium; 6) its virtually zero mechanical hysteresis; 7) silicon wafers are extremely flat and accept coatings and additional thin-film layers for building microstructural geometry or conducting electricity; 8) treatments and fabrication processes for silicon substrates are well established and documented. In MEMS fabrication, silicon can be chemically etched into various shapes and associated thin-film materials.

2.1.2 Fabrication Processes

Most fabrication steps of MEMS devices are derived from standard IC processing and they are classified into *bulk micromachining* and *surface micromachining*. The term micromachining refers to the fabrication of micromechanical structures with the aid of etching techniques to remove part of the substrate or a thin film.

Bulk Micromachining

It is the oldest technology used in the MEMS fabrication. In this, mechanical structures are created within the boundaries of single-crystal silicon wafer by selectively removing parts of a wafer material by using orientation-dependant etching. The etching approaches used can be compatible with on-chip circuitry, which has allowed bulk micromachining to be combined with complementary metal–oxide–semiconductor (CMOS) circuitry. As it is depicted in Figure 2.4, the geometries of etched features lie along between fully isotropic (rounded, due to equal etch rates in all directions) to anisotropic (flat surfaces and well-defined, sharp angles). These properties are mainly defined by the nature of the chemical reactions (wet, dry or vapor etchants), the diffusion of reactants and products [3]. Bulk micromachining utilizes the etch selectivity between the orientation planes 111, 100 and/or 110 to fabricate structures. High aspect ratio devices are defined by etching into a substrate, usually monocrystalline silicon.
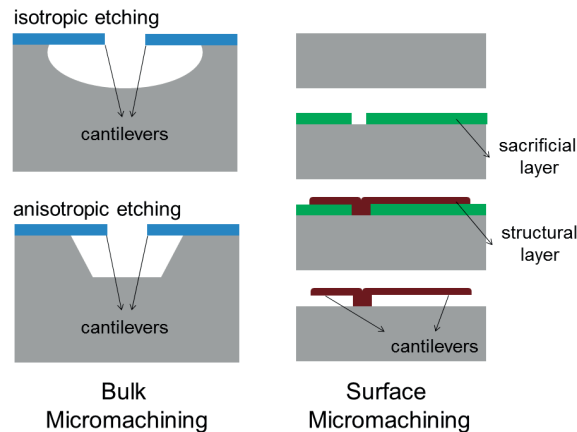
Figure 2.4 – Illustration of (left) bulk-micromachining and (right) surface-micromachining.

Surface Micromachining

It is a method of producing MEMS by depositing, patterning and etching a sequence of thin films typically in the range 1-100 micrometer thick. In contrast to the bulk micromachining, surface micromachining builds the structures on the silicon surface by depositing thin films of sacrificial layers and structural layers and eventually the mechanical structures are formed by removing the sacrificial layers. The major advantage of surface micromachining is that there is no constraint on the miniaturization of the devices fabricated other than those raised by the limitation in the lithography technology. Also, structurally complex mechanical systems, including free-standing or movable parts can be created by stacking multiple layers of material. In addition, surface micromachining offers a high degree of compatibility with IC processing.

2.1.3   Prime functions, Applications and Markets

Prime Functions

In the most general form, the prime MEMS consist of mechanical *sensors* and *actuators* (these are also called as transducers because they help in conversion of one form of the energy into another) and *microelectronic systems*, all integrated onto the same silicon chip. Sensors detect changes in the environment of the microsystems and actuators react and create changes to the environment of the microsystems. Both sensors and actuators carry out transduction by measuring either mechanical, electrical, piezoresistive, piezoelectric, thermal, optical,

magnetic or chemical phenomena. Microelectronic systems receive, process and send the acquired information to other areas of the chip.

The integration on chip of several of these microstuctures lead to the possibility of creating new distributed control systems. For example, the force or displacement sensors of a MEMS system convert a mechanical signal into an electrical one; the analog electrical signal from the sensor is then passed to the controller and is amplified, conditioned, converted into digital format, processed, converted back to analog and finally, the electrical signal is converted back into a mechanical signal by a force or displacement actuator.

MEMS Applications

Taking into account the natural interdisciplinarity and versatility of MEMS, a large amount of applications have been developed since their inception. From a very early vision in the early 1950's, MEMS have gradually made its way out of research laboratories and into everyday products. In the mid-1990's, MEMS components began appearing in numerous commercial products and applications including accelerometers used to control airbag deployment in vehicles, pressure sensors for medical applications, and inkjet printer heads. Later, also other products were developed, like oscillators, microphones, displays and lab-on-a-chip devices.

Due to their enhanced performance and reduced cost, MEMS have ended by address the severe and often conflicting requirements for modern applications in mostly all the industrial areas, such as automotive, communications, defence, aeronautics, industrial process control, consumer and medical applications.

MEMS Markets

MEMS devices development is currently experimenting a real change of paradigm. Previously, their design cycle followed the well-known power-size-cost reduction in order to reach a greater volume of consumers. Nowadays, MEMS devices are already well entrenched in the markets and accordingly they are now facing new design challenges.

The user-friendliness of the devices has become so important to expand the markets to new

consumers that the design cycle has been inverted: nowadays the final applications mark the route downwards to the chips needed to support them, looking for a better fusion between what the silicon and software industries can offer if they are put together.

Therefore, power consumption has become the most relevant design trend in order to fabricate hybrid applications (MEMS and software) able to make survive the user-friendly features linked to the MEMS for long periods on battery while they are interacting with the environment. Actually, the combination of MEMS devices with other MEMS sensors and other features (like software functions) is helping to increase margins of benefit of MEMS production.

2.2 MEMS Resonators

RF MEMS are designed specifically for use within the electronics in mobile phones and other wireless communication applications such as radar, global positioning satellite systems (GPS) and steerable antennae. The main advantages gained from RF MEMS include higher isolation and thus less power loss and better integrability with other electronics. RF MEMS provide performance and reliability to these applications while driving down simultaneosly their size and cost [4].

RF MEMS technology includes passive devices such as capacitors, inductors, filters and transmission lines but also active devices such as switches or resonators. MEMS resonators have been developed for decades and are today on the verge of replacing the existing mechanical resonators [5]. Silicon MEMS resonators generally work in the lower range of frequencies and aim to replace quartz resonators in the low frequency range [5].

2.2.1 Main Characteristics and Figures-of-Merit (FOMs)

In this section the main characteristics for MEMS resonators are introduced, as well as their classification in terms of modes of resonance and excitation and detection transduction mechanisms.

The most referred ones are:

- **Resonance frequency, (f_0):** frequency at which a vibrating system is driven to the greatest amplitude of oscillations. At resonance frequencies, small periodic driving forces have the ability to produce large amplitude oscillations.

- **Quality factor, (Q-factor, Q):** sharpness of the frequency response of a resonator (ideally infinite). It can also be described as the ability to retain energy with less dissipation. Resonant circuits are used to respond selectively to signals at a given frequency (f_0) while discriminating signals at other frequencies. If the response of the device is more narrowly peaked around the resonance frequency, the circuit has higher selectivity. Quality factor is a measure of that selectivity.

- **f_0xQ product:** product of the resonance frequency and the Q-factor is a typical indication of the quality of the resonator.

- **Motional resistance, (R_m):** ratio of the input voltage to the output current. It represents the efficiency of transduction from input to output at resonance.

- **Temperature coefficient of frequency, (TCF):** sensitivity of the resonant frequency to changes in temperature. Smaller values lead to an improved frequency stability in the presence of thermal fluctuations [6].

- **Signal-To-Noise Ratio, (SNR)**: is a measure that compares the level of a desired signal to the level of background noise. It is defined as the ratio of signal power to the noise power. Intrinsic signal amplification in RF MEMS resonators is still matter of extreme importance in order to have good levels of signals at the output of the systems without needing extra circuitry.

Other factors like the power handling capacity (ability of withstand large input power and deformations while behaving linearly), easy tuning of the frequency and scalability are also important properties to be considered in resonators design and comparison.

The most quoted FOM for MEMS resonators, are the f_0xQ product jointly with the motional resistance.

2.2.2 Modes of Resonance

Intuitively, the most general way to classify RF MEMS resonators is by taking into consideration the relation to the direction in which vibrations are produced with respect to the plane where the resonator is built.
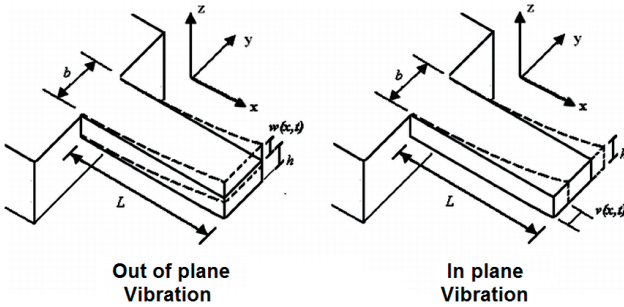
Figure 2.5 – RF MEMS Classification considering plane vibrations: (left) out-of-plane and (right) in-plane vibrations [7].

The modes of resonance that can be obtained are: 1) out-plane (or vertical), in which the vibrations follow a direction transversal to the plane; and 2) in-plane (horizontal), where the vibrations are produced in a lateral direction parallel to the plane. A mock-up view of these general modes of resonance is included in Figure 2.5.

Additionally, taking into account the geometry of the resonator (cantilevers, plates, disks, rings, interleaved fingers,...), the location of the driving electrodes and the anchors, different resonance modes can be achieved. Broadly, they are three resonance modes for RF MEMS: 1) flexural; 2) torsional and 3) bulk mode (see Figure 2.6) [7].
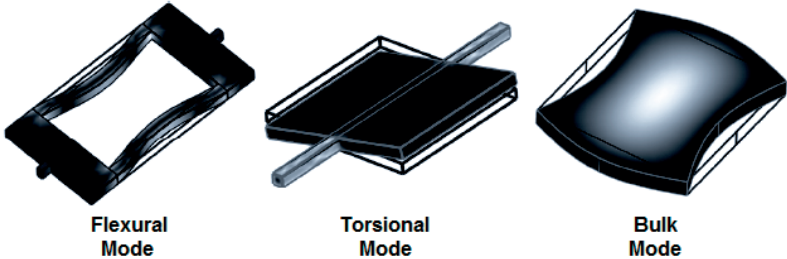
Figure 2.6 – Typical Modes of Resonance for RF MEMS: (left) flexural; (middle) torsional and (right) bulk modes [7].

In devices vibrating in flexural mode, the displacement of the structures is orthogonal to the bending stress in the structure [8]. The most spread geometries for flexural mode of resonance are clamped-clamped beams and free-free beams (see Figure 2.7), depending on where the nodal points are considered (in the extremes of the structure or in intermediate points).
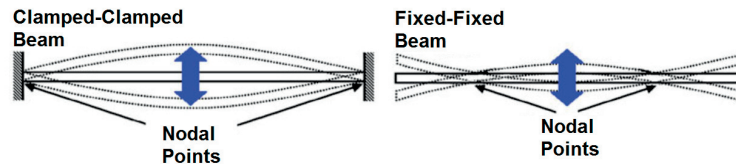
Figure 2.7 – Typical modal shapes for beams resonators in flexural mode: (left) clamped-clamped and (right) fiex-fixed beam [8].

In resonators vibrating in the torsional mode, the dominant stress is shear-stress and the displacement produced is rotational in nature [8]. The usual geometries that show torsional modes of resonance are squared plates fixed by air bridges that undergo the maximum shear-stress in their junction with the moveable plate (see Figure 2.6).

The most common modal shapes for a square-plate bulk mode device are extensional (or contour) and Lamé modes as they are depicted in Figure 2.8.
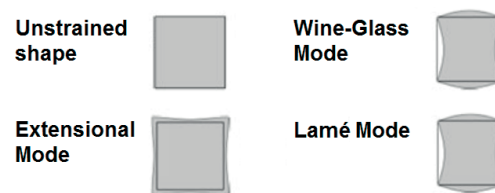
Figure 2.8 – Typical modal shapes for square-plates resonators in bulk mode [8].

As it is illustrated in Figure 2.9, the common modal shapes for a bulk mode device in a circular-disk resonator are radial-contour (or, extensional or breathing) mode, where the shape of the disk expands and contracts equally in all the lateral surface and elliptical (or, wine-glass) mod,e where the disk expands along one axis and contracts in the orthogonal axis forming two alternate and perpendicular ellipses per cycle of vibration with four nodal points at the perimeter.
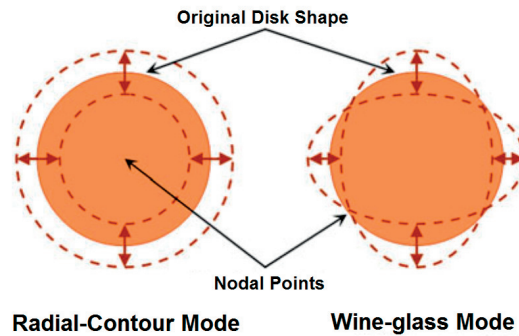
Figure 2.9 – Typical modal shapes for disks resonators in bulk mode: (left) radial and (right) wine-glass modes [8].

2.2.3 Transduction Mechanisms

RF MEMS resonators can be classified taking into consideration the actuation mechanism as: 1) capacitive (or electrostatic) and 2) piezoelectric.

- **Capacitive actuation**: The body of the resonator is driven to resonance by means of an input AC signal applied to the electrodes that surround the resonator at a certain distance (gap). The capacitance existing between the resonator body and the electrodes is periodically charged and discharged as a function of the effective motional changes of the gap. Depending on the material that fills the gap, air or a high-k dielectric , some of the figures of merit will increase to the detriment of the others (see Section 3.2.5). A DC voltage can be applied to increase the capacitive coupling in the gap by respecting the breakdown phenomena in the gap [5]. The measured output current results from the change of charges on the capacitor (capacitive read-out).

- **Piezoelectric actuation**: The most typical piezoelectric resonators are *Surface Acoustic Wave* (SAW) and *Bulk Acoustic Wave* (BAW) resonators. In SAW resonators devices, a surface acoustic wave travels on the surface of a piezoelectric material. Piezoelectric materials are used to transform the electrical signals into surface acoustic waves. BAW resonators are electromechanical devices in which a standing acoustic wave is generated by an electrical signal in the bulk of a piezoelectric material. In the simplest configuration, a device consists of a piezoelectric material (typically quartz, AlN, or ZnO) sandwiched between two metallic electrodes [9]. Depending on the mode of resonance

that is excited, BAW resonators can be *Film Bulk Acoustic Resonators* (FBARs) or *Thin Film Bulk Acoustic Resonators* (TFBARs), when resonators exploit width-extensional mode shapes, or *Contour Mode Resonators* (CMRs), when resonators exploit length-extensional mode shapes. FBARs/TFBARs resonance modes depend on the thickness of the deposited piezoelectric material. As it is shown in Figure 2.10, the stack can be suspended on a cavity (free FBAR/TFBAR) or mounted on a Bragg reflector to decouple the acoustic wave from the substrate (Solidly Mounted Resonator, SMR). In CMRs, the electric field is configured to cause the resonator to have a in-plane lateral displacement (in the plane of the planar surface of the resonator), wherein the fundamental frequency for the displacement of the piezoelectric resonator is set in part lithographically by the planar dimension of the bottom electrode, the top electrode and the piezoelectric layer. Typically, admittance changes are measured at the output of piezoelectric resonators to detect the resonance peak (maximum amplitude of admittance) and antiresonance peak (minimum amplitude of admittance) of the resonators.
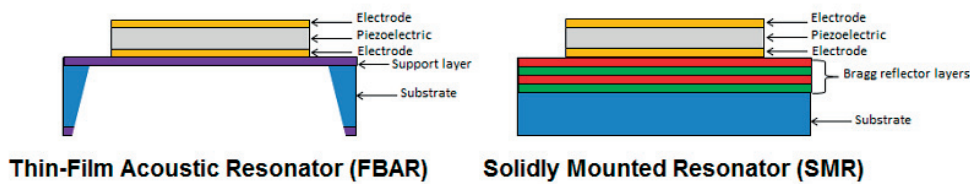
Figure 2.10 – Representation of (left) free Thin-Film Bulk Acoustic Resonators (TFBAR) and (right) Solidly Mounted Resonators (SMR) [5].

Regarding to the read-out mechanism, RF MEMS resonators can be classified into 1) capacitive (or electrostatic); 2) piezoelectric (mechanisms that can be derived from the excitation mechanisms listed above); 3) piezoresistive and 4) based on Filed-Effect transistor. The latter two mechanisms have been proven to increase the output signal gain, what offers alternative solutions for high frequency resonators, where displacements and output current become small.

- *Piezoresistive read-out*: this approach combines electrostatic actuation with piezoresistive read-out. As it is depicted in Figure 2.11, resonators consist of masses suspended by springs (arms) that are compressed and stretched along their axis at resonance. The

resulting mechanical strain is detected by measuring the change in the electrical resistance of the resonator arms caused by the piezoresistive effect [10]. Piezoresistive sensing has been proven to lower the motional impedance [11] as well as being capable of a signal amplification [10].
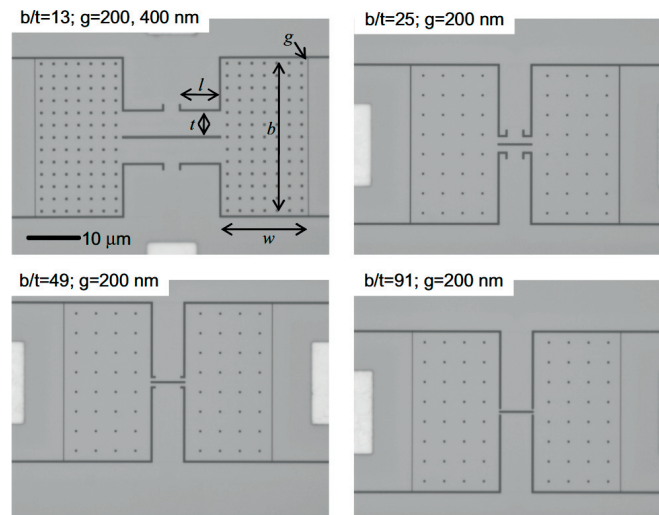
Figure 2.11 – Resonators based on capacitive actuation and piezoresistive read-out [10].

- **Based-on-FET read-out**: this approach combines electrostatic actuation with both electrostatic and FET read-out. An additional amplification is achieved by means of the channel modulation of a transistors embedded on the body of the resonator. Flexural [12] and bulk [13] resonators based on FET read-out have been proven to achieved an enhancement in the signal level up to +30 dB [5] [14] [15] [16] (see Figure 2.12).
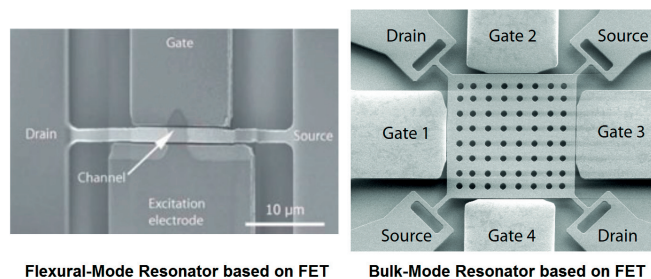
Figure 2.12 – Flexural (left) and bulk (right) resonators based on capacitive actuation and FET read-out [12] [13].

2.2.4 State-of-the-Art of MEMS Resonators

Some of the most relevant devices that have been published in the last years and have inspired this work are listed in Tables 2.2, 2.3 and 2.4. Due to the scope of the present work, MEMS resonators based on solid or partially-solid transduction gap are independently highlighted in Table 2.5.

Capacitive coupling is one of the most refered transduction methods in MEMS gyroscopes [17] and has been a particularly revisitited transduction method in the design of MEMS resonators [18] [19] [20]. MEMS resonatos based on capacitive transduction are compatible with ICs and provice flexible designs, achieving self-switching capabilities, voltage-control reconfigurability and better good stability than piezoelectric transductions. In combination with this method, piezoresisitive transduction has been more and more often addressed due to additional transconductance gain induced by the strain changes in the vibrating body of a resonator that is proportional to the current through the resonator in combination with the bias voltage that is applied over the transduction gap [21] [22] [23]. Moreover this method is very suitable for use in high frequency resonators since the associated transconductance has been proven not to change when resonator dimensions are scaled down [24].

VB-FETs have been reported to have a built-in amplification of more than +30 dB over the pure capacitive response of the electrostatic transduction [13]. In comparison with capacitive resonators, vibrating body FET (VB-FET) resonators require more complex and expensive fabrication processes.

By virtue of VB-FET transduction method, flexural MEMS resonators based on beam-type structures that vibrate in flexural-lateral (or flexural-vertical) modes of resonance have reported a f_0xQ product of the order of up to $\sim 10^{12}$ [25] with motional resistances in the range of kΩ. Outstandingly, motional resistance as low as 31 Ω has been reported in clamped-clamped (CC) VB-FETs by means of FET detection mechanisms [26] for V_{bias} = 12 V.

Eventually, optical detection is used to characterize MEMS resonators [27], and more particularly NEMS resonators, with the aim of having ultrahigh mass sensing and spectrometry applications.

Recently, alternative semiconductor materials as polymorphs of silicon carbide (4H-SiC) have been proposed to enlarge the filtering and sensing in harsh environments [28] applications of MEMS resonators. Nevertheless, in order to have larger f_0xQ product, high frequency and/or narrow bandwidth devices have to be fabricated by means of bulk MEMS resonators (mainly disks and plates). f_0xQ as high as 10^{13}-10^{14} have been obtained with diamond as structural material [19] or with MEMS resonators based on transduction gaps partially-filled with a high-k material, which additionaly have larger equivalent capacitance in the gap and lower motional resistance [29].

Solid and partially-filled dielectric gap resonators started to attract a certain interest in comparison to the air-gap electrostatic transduction as the gap could be reduced and the device is more robust and reliable. In addition, solid-gaps are preferable to air-gaps since solid-filled gaps enhance the transduction efficiency and the electrical resonance current, and reduce the motional resistance [30], but they are more difficult to fabricate and can betray additional damping (see Appendix B).

In this work, flexural and bulk MEMS resonators have been designed, fabricated and characterized in order to show the effect of the transduction gap-filling by means of the Atomic Layer Deposition (ALD) of a high-k dielectric (HfO$_2$) in the motional performance of the devices, i. e. capacitive coupling in the gap and motional resistance (see Chapter 4). The implementation of the fabricated devices as mass sensors is reported in Chapter 5. Contrary to what has been reported in [30] [31], HfO$_2$ ALD method to close the gap, not only reduces the motional resistance and improves the coupling coefficient and the output response of the device, but also it helps to improve the Q-factor of our devices, increasing the magnitude peak and making the phase transition steeper as a result of the fabrication process (probably the annealing during the ALD step). An improvement in the f_0xQ product up to 10 times has been achieved for 5 nm covered double-ended tuned forks vibrating in their lateral mode and up to 8 times the one of bulk wine-glass disk (WGD) resonators.

To finalize, some examples of commercial MEMS resonators are presented in Table 2.6. SiTime proposed the ultra-small and ultra-low power MEMS oscillator specifically designed for wearable, Internet-of-Things (IoT) and mobile applications where space and power are critical.

They are up to 90% lower in power consumption and up to 80% smaller in size than quartz oscillators working in a frequency range between 1 - 26 MHz. Other two examples of MEMS oscillators are the ultra miniature pure silicon clock presented by Abracon with resonance frequency between 1 and 150 MHz and the low-jitter precision CMOS oscillator made by Microchip (see Table 2.6).

Maxim Integrated has developed the industry's first temperature-compensated Real-Time Clock (RTC) with an internal MEMS resonator. This allows the device to be used in high-vibration environments, removing malfunctions due to crystal mechanical failures, enhancing the long-term accuracy of the device and reducing the piece-part count in a manufacturing line.

These devices have proven silicon MEMS technology to provide excellent jitter and stability over a wide range of supply voltages and temperatures. By eliminating the need for quartz or SAW technology, MEMS oscillators significantly enhance reliability and accelerate product development, while meeting stringent clock performance criteria for a variety of communications, storage and networking applications.

Table 2.2 – Capacitive MEMS resonators II: beams.

Device	Ionescu 2008 [25]	Barniol 2009 [32]	Ionescu 2011 [33]	Ionescu 2011 [26]	Lee 2015 [21]	Xie 2016 [18]	Zhao 2016 [28]	This work	This work	This work
Type	PBR	CCB	DETF	CCB	DETF	DETF	CCB	CCB	DETF	PBR
Resonance Mode	Flexural-Lateral	Flexural-Lateral	Flexural-Lateral	Flexural-Lateral	Flexural-Lateral	Flexural-Lateral	Flexural-Vertical	Flexural-Lateral	Flexural-Lateral	Flexural-Lateral
Mode	Fund.	Fund.	Fund.	Fund.	Fund.	3rd 4th 6th	Fund.	Fund.	Fund.	Fund.
Material	Si	PolySi	Si	Si	Si	Si	4H-SiC	Si	Si	Si
Readout	Capacitive	Capacitive	FET	FET	Piezores.	Capacitive	Optical	Capacitive	Capacitive	Capacitive
f_0 (MHz)	24.48	22	113	2.375	0.609	0.35 0.385 0.677	3.463	5.59	10.81	23.59
Q	122000	4400	1300	6790	12360	-	25000	201 [a]	1020	4247
f_0xQ (Hz)	$2.98 \cdot 10^{12}$	$9.68 \cdot 10^{10}$	$1.5 \cdot 10^{11}$	$1.61 \cdot 10^{10}$	$7.5 \cdot 10^{9}$	-	$8.66 \cdot 10^{10}$	$1.12 \cdot 10^{9}$	$1.1 \cdot 10^{10}$	$1 \cdot 10^{11}$
R_m (Ω)	59k	-	100k	31	-	-	-	212.9k	3.3k	14.15k
V_{bias} (V)	12	5	10	12	10	10	-	60	100	100

[a]Quality factors calculated with the phase-slope approximation.

23

Device	Ayazi 2004 [34]	Ionescu 2009 [35]	Suzuki 2010 [27]	Seshia 2011 [36]	Nguyen 2011 [37]	Nguyen 2012 [38]	Legrand 2013 [22]	Nguyen 2013 [19]	This work
Type	Disk	Disk	Ring	Disk	Disk	Ring	Ring	Disk	Disk
Resonance Mode	Elliptical	WG	Radial	WG	Radial	Radial	WG	Radial	WG
Mode	Fund.	Fund.	Fund.	Fund.	Fund. 3rd 6th	Fund.	Fund.	Fund.	Fund.
Material Readout	Si Capacitive	Si Capacitive	Si Optical	Si Capacitive	PolySi Capacitive	Diamond Capacitive	Si Piezores.	Diamond Capacitive	Si Piezores.
f_0 (MHz)	149.3	30.79	1.62	5.44	115.4 178.5 329.36	$2.97 \cdot 10^3$	0.96	$1.51 \cdot 10^3$	41.09
Q	45700	20000	30062	$1.52 \cdot 10^6$	29309 73240 56061	42900	53000	11555	1482
$f_0 \times Q$ (Hz)	$6.82 \cdot 10^{12}$	$6.16 \cdot 10^{11}$	$4.87 \cdot 10^{10}$	$8.26 \cdot 10^{12}$	$3.38 \cdot 10^{12}$ $1.31 \cdot 10^{13}$ $1.85 \cdot 10^{13}$	$1.27 \cdot 10^{14}$	$5.1 \cdot 10^{10}$	$1.74 \cdot 10^{13}$	$6 \cdot 10^{10}$
R_m (Ω)	43.3k	131k	-	-	-	81k	-	-	4.49k
V_{bias} (V)	17	32	-	60	9 5 3	8	25	10	160

Table 2.3 – Capacitive MEMS resonators II: disks and rings.

24

Table 2.4 – Capacitive MEMS resonators III: Plates.

Device	Ionescu 2007 [12]	Ionescu 2008 [13]	Ollier 2010 [39]	Seshia 2010 [40]	Pourkamali 2011 [23]	Caillat 2011 [41]	Seshia 2011 [42]	Li 2012 [20]	This work
Type	Plate	Plate	Plate	Plate	DogBone	Plate	Plate	Plate	Plate
Resonance Mode	Lamé	Lamé	Lamé	Lamé	Lat.-Ext.	Lamé	Lamé	Lamé	-
Mode	Fund.	Fund.	Fund.	2nd	Fund.	Fund.	Fund.	Fund.	Fund.
Material	Si	Si	Si	Si	Si	Si	Si	Si	Si
Readout	FET	Capacitive	Capacitive	Piezores.	Piezores.	Capacitive	Capacitive	Capacitive	Capacitive
f_0 (MHz)	32	71.04	97.68	2.2	4.5	78	5.17	47.9	14.64
Q	4000	15400	58000	6771	40000	3000	$1.78 \cdot 10^6$	10696	784
f_0xQ (Hz)	$1.28 \cdot 10^{11}$	$1.09 \cdot 10^{12}$	$5.67 \cdot 10^{12}$	$1.49 \cdot 10^{10}$	$1.8 \cdot 10^{11}$	$2.3 \cdot 10^{11}$	$9.2 \cdot 10^{12}$	$5.1 \cdot 10^{11}$	$1.15 \cdot 10^{10}$
R_m (Ω)	-	55.2k	50k	-	3985k	-	101.5k	205k	11.3k
V_{bias} (V)	30	40	4.6	2	-	60	60	70	120

Table 2.5 – Solid or partially-filled gap capacitive MEMS resonators.

Device	Nguyen 2004 [30]	Nguyen 2005 [31]	Nguyen 2007 [43]	Bhave 2010 [29]	Howe 2010 [44]	**This work**	**This work**	**This work**
Type	Disk	Disk	Ring	Plate	CCB	DETF	PBR	Disk
Resonance Mode	WG	WG	WG	Longitud.	Lamé	Flexural	Flexural	WG
Solid-Gap Material	HfO_2	Si_3N_4	Si_3N_4	HfO_2	Si_3N_4	HfO_2	HfO_2	HfO_2
Structural Material	PolySi	PolySi	PolySi	PolySi	PolySi	Si	Si	Si
Readout	Capacitive	Capacitive	Capacitive	Capacitive	Capacitive	Capacitive	Capacitive	Piezores.
f_0 (MHz)	58.85	61.67	979.6	222.86	128.15	5.5022	10.8516	41.2412
Q	7368	25300	3160	67920	12000	409	8433	12163
$f_0 \times Q$ (Hz)	$4.34 \cdot 10^{11}$	$1.56 \cdot 10^{12}$	$3.1 \cdot 10^{12}$	$1.51 \cdot 10^{13}$	$1.53 \cdot 10^{12}$	$2.25 \cdot 10^9$	$9.15 \cdot 10^{10}$	$5.02 \cdot 10^{11}$
R_m (Ω)	685	$1.51 \cdot 10^3$	-	1256	$30 \cdot 10^3$	42.3k	8.7k	874
V_{bias} (V)	19	8	4	5	20	60	90	80

Table 2.6 – Some examples of commercial MEMS resonators.

Device	**SiTime** Oscillator SiT1532	**Abracon** Oscillator ASDMB	**Microchip** Oscillator DSC1101	**Maxim Integrated** RT Clock DS3232M
Footprint (mm^2)	1.2	5	8	-
Material	Si	Si	Si	-
f_0 (Hz)	32.768k	24M	40M	-
Power	$< 1 \mu A$	< 10 mA	-	-
V_{supply} range (V)	1.5 - 3.63	-0.3 - 4	2.25 - 3.6	2.3 - 5.5
Applications	Mobile Phones Tablets Watches	Peripherals MP3 Games	Communications Storage Networking	Internal Resonator [a]

[a]Internal MEMS Resonator to reduce crystal mechanical failure

2.3 Summary

In this chapter, we have fulfilled an introduction to MEMS devices and MEMS resonators, taking into consideration materials, main fabrication processes and major fields of application. The fundamentals of MEMS resonators devices have been acquainted in terms of their FOMs (mainly resonance frequency, quality factor and motional resistance), modes of resonance (depending on vibration-plane, geometry and modal shape) and main actuation and detection transduction mechanisms.

To conclude, a thorough comparison between the most recent capacitive MEMS devices that vibrate in flexural (beam-type devices) and bulk modes (disk and plate devices) is accomplished, highlighting f_0xQ products up to $\sim 10^{12}$ for parallel beam resonators (PBR) [25] and between 10^{10} and 10^{14} for bulk resonators. A special attention has been brought to capacitive solid and partially-filled resonators, which have been reported to have quality factors as high as 67920 for plates vibrating at their longitudinal resonance mode with motional resistances around 1 kΩ. The highest f_0xQ reported for the devices that have been designed, fabricated and characterized during this work is $5 \cdot 10^{11}$ for a wine-glass disk (WGD) resonator with HfO_2 partially-filled gap.

3 Analytical Models and Simulations

The combination of analytical and Finite Elements Methods (FEM) base on COMSOL®Multiphysics modelling presented in this chapter provides preliminary studies for the ulterior design, fabrication and characterization of the flexural and bulk capacitive MEMS resonators presented in Chapter 4.

In this chapter, reduction of the motional resistance up to a factor of 600 times have been analytically extracted for capacitive MEMS resonators based on high-k solid-gaps (Si_3N_4 and HfO_2), enlightening the possibility of explore gap-filling in order to reduce the motional resistance.

By applying and comparing analytical and FEM models, the approximative resonance frequencies for the designed MEMS resonators and the existing absolute error between theory and simulations have been extracted for each designed device. The absolute errors between analytical and FEM models have been observed to be up to 0.5 MHz for clamped-clamped beams, 1.43 MHz for double-ended tuning forks, 28.86 MHz for wine-glass disks and 6.6 MHz for square plate resonators, revealing that the inclusion of the needed releasing holes for the fabrication of bulk resonators is underestimated in the analytical models and thus FEM models should be considered for the preparatory design phase before fabrication. Variabilities coming from geometry, elastic properties of the structural material, realising holes influence and anchors clamping are included and they will help to read better into the experimental results presented in Chapter 4.

3.1 Introduction

In this chapter, in the first place the fundamental theoretical concepts for capacitive MEMS resonators are analysed, including equivalent models, actuation and detection methods, transduction mechanisms for air and filled gaps, and emphasizing their nonlinear dynamics effects and essential FOMs. Then, analytical and FEM models for the resonators that are case of study (clamped-clamped beam, double-ending tuning fork, parallel beam, bulk disk and square plate resonators) are included and compared.

3.2 Capacitive MEMS Resonators

Capacitive, dielectric or electrostatic MEMS resonators are devices composed by a vibrating part, the body of the resonator (normally suspended), and one or several fixed parts that consist of the electrodes and the supporting structure. As a resonator body has infinitive number of resonant modes, in order to preferentially favour the natural resonant frequency and modal shape, the number of electrodes and their emplacement around the resonator body need to be strategically chosen [45].

In Figure 3.1 a capacitive clamped-clamped beam resonator is sketched: the beam body is actuated by two fixed electrodes, the excitation and detection (or readout) ones, that operate as the two input-output ports of the device. Signal amplification based on multi-gate actuation was reported in [35].

As it is studied in Section 3.2.6, the resonator body and the substrate bulk are normally grounded in order to avoid vertical collapse. Capacitive transduction is carried out by means of a time-varying AC signal (v_{ac}) in combination with a DC signal (V_{bias}) applied to the excitation electrode. This excitation generates an electrostatic force (F) on the resonator body at the same frequency as the (v_{ac}) signal that drives the displacement of the resonator body whereas it is close to its natural resonance frequency, deforming it in certain shape (modal shape). This movement changes the gap spacing existing between the body and the readout electrode, resulting in a variable gap capacitor that generates a current in the readout electrode. Vibrations at higher frequencies than the natural resonance frequency do not normally
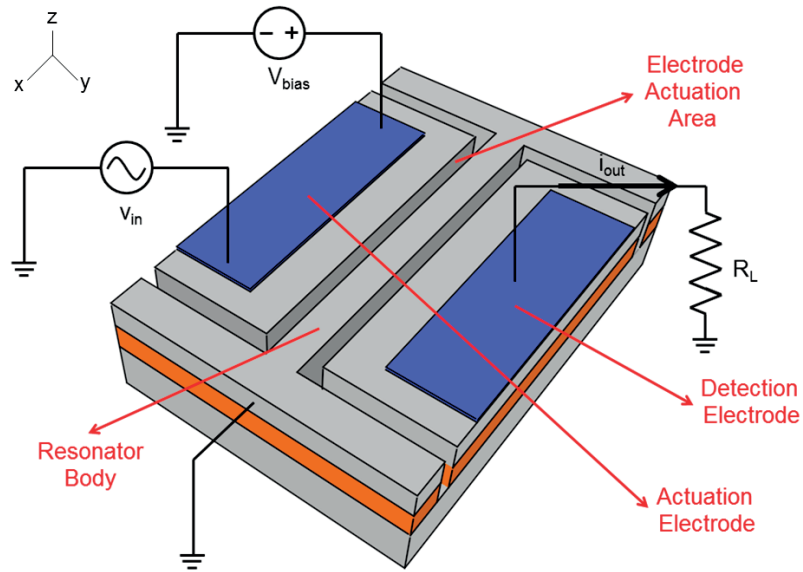
Figure 3.1 – Two-ports clamped-clamped beam resonator with applied signals for capacitive actuation and detection. With this electrodes configuration the vibrations are performed preferentially in parallel to the xy-plane.

generate considerable deflection along the structures, as a result, the current induced in the detection electrode is the one driven by the natural resonance frequency of the resonator.

The stored energy in each gap capacitor is expressed as:

$$E_{stored} = \frac{1}{2}C(V_{bias} + v_{ac}^{j\omega t})^2 \tag{3.1}$$

Capacitive transduction employs electrostatic forces to convert energy from the electrical to the mechanical domain and vice versa. The driving force between the capacitor plates (conformed by the sidewalls of both the electrode and the resonator body) can be calculated as the variation in time of the energy stored in the capacitors:

$$\begin{aligned}
F_d &= \frac{1}{2}\frac{\partial C}{\partial x}(V_{bias} + v_{ac}^{j\omega t})^2 = \\
&= \frac{1}{2}\frac{\partial C}{\partial x}(V_{bias}^2 + 2V_{bias}v_{ac}^{j\omega t} + v_{ac}^{j2\omega t})
\end{aligned} \tag{3.2}$$

As it has been introduced in Equation 3.2, if a very small displacement is considered, the driving force between the capacitor plates has three components: (1) a DC component proportional to V_{bias}^2; (b) a component of frequency depending on the product $V_{bias}v_{ac}$ and (c) an AC component proportional to v_{ac}^2.

3.2.1 Motion Equation

Due to the existing analogies between the equations governing the behaviour of electrical systems and mechanical systems [46], MEMS resonators can be represented by a lumped electrical circuit as it is described in Table 3.1.

Table 3.1 – Mechanical and electrical analogies for MEMS devices.

Mechanical Parameter	Electrical Parameter
Mass, m	Inductance, L
Damping, b	Resistance, R
Compliance (or Stiffness), 1/k	Capacitance, C
Velocity, u	Current, I
Displacement, x	Charge, q
Momentum, p	Magnetic Flux Linkage, λ
Force, F	Voltage, V

Hence, instead of considering the displacement and velocity for each particle of the resonator at every point of time, its motional behaviour can be modelled using an effective mass m (also named m_{eff}), connected to a spring with stiffness k (spring constant) and a dashpot b (damping coefficient) as it is depicted in Figure 3.2 [47].
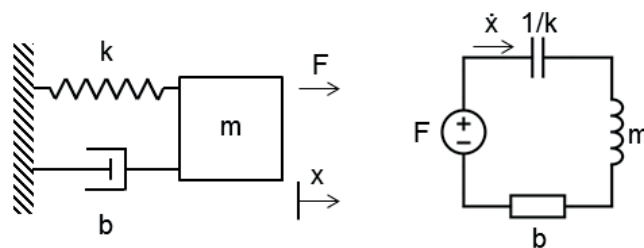
Figure 3.2 – (Lumped model of a spring-mass-dashpot system representing (left) a mechanical resonator and (right) its equivalent electrical circuit.

Applying the lumped model shown in Figure 3.2 to a capacitive MEMS resonator actuated by an external time-dependant force F(t) [48] (forced harmonic oscillation) as it is introduced in

Section 3.2, an ordinary differential equation relating the driving force to the displacement is given by:

$$F(t) = A_f \cos \omega t$$
$$F = m\ddot{x} + b\dot{x} + kx =$$
$$= m\frac{\partial^2 x}{\partial t^2} + b\frac{\partial x}{\partial t} + kx$$
(3.3)

where A_f is the magnitude of the applied sinusoidal force. Assuming the Laplace domain, force is of the form $F = F(s)e^{st}$ and displacement function of the form $x = X(s)e^{st}$, Equation 3.3 turns into:

$$F(s) = X(s)(ms^2 + bs + k)$$
(3.4)

which gives the transfer function relating the input force and the output displacement as:

$$\frac{X(s)}{F(s)} = \frac{1}{ms^2 + bs + k}$$
(3.5)

Then, by solving Equation 3.5 [49] the undamped resonance frequency ω_0 and damping ratio ζ for an actuated MEMS resonator are obtained:

$$\omega_0 = \sqrt{\frac{k}{m}} \qquad \zeta = \frac{b}{2\sqrt{km}}$$
(3.6)

For the case in which the damping ratio is not neglected, the damped resonance frequency is defined by:

$$\omega_d = \omega_0\sqrt{1 - \zeta^2}$$
(3.7)

Note that the damped natural frequency is less than its undamped counterpart, however, for small-to-moderate values of the damping ratio ($\zeta < 0.2$), the damped natural frequency is approximately the same as the undamped resonance frequency.

Equations 3.6 give useful information about how to obtain an alternative way to characterize the energy dissipation inherent to the device by means of the following Q factor definition:

$$Q = \frac{1}{2\zeta} = \frac{\sqrt{km}}{b} \tag{3.8}$$

Regarding the previous expression it is concluded that in order to obtain MEMS resonators with high Q-factors it is needed: (a) high k (i.e. stiff devices); (b) high m (i.e. large, and therefore low frequency, devices) and (c) low damping.

3.2.2 Butterworth-Van Dyke Model

By means of the equivalences presented in Table 3.1, it is straightforward to turn the circuit based on mechanical parameters to its counterpart electrical circuit based on a resistance-inductance-capacitance (RLC) tank. This series RLC branch driven by a AC voltage at the natural resonance frequency of the resonator is depicted in Figure 3.3 [50].
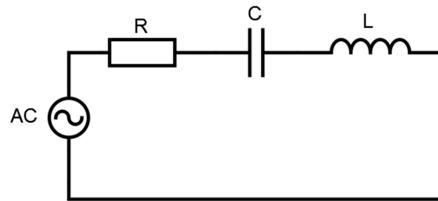
Figure 3.3 – Series (left) and parallel (right) resonance.

Resonance occurs because energy is stored in two different ways: in an electric field as the capacitor is charged and in a magnetic field as current flows through the inductor. Energy can be transferred from one to the other within the circuit and this can be oscillatory. Resonance of a series RLC circuit occurs when the inductive and capacitive reactances are equal in magnitude but cancel each other because they are 180° apart in phase. Introducing the resistor increases the decay of these oscillations, which is also known as damping. Here, the equivalent undamped resonance frequency (see Equation 3.6) can be expressed as:

$$\omega_0 = \frac{1}{\sqrt{LC}} \tag{3.9}$$

In order to add to the RLC equivalent circuit the characteristic parasitics capacitances linked

to the device, the Butterworth-Van Dyke (BVD) model includes input and output parallel shunt capacitances (C_p), and direct input to output feedthrough capacitance in parallel with the RLC branch (C_0) [51]. The resulting circuit is shown in Figure 3.4.
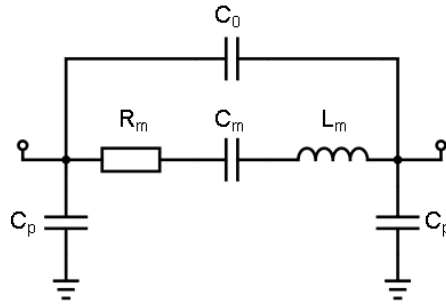
Figure 3.4 – Simplified electrical circuit of a two-port capacitive MEMS resonator with feedthrough capacitance C_0.

The signal feedthrough between the electrodes has different origins: (a) part of the energy is transferred through the air due to the bending of the electrical field between the electrodes named fringing field [52] and (b) another part is transferred through the substrate parasitic capacitors [53].

To convert the motion equation presented in Equation 3.3 into its electrical equivalent definition, voltage and current are used as variables analogous to force and velocity (see Table 3.1), then obtaining the electrical domain expression:

$$V = L\frac{dI}{dt} + RI + \frac{1}{C}\int Q\, dt \tag{3.10}$$

where V is the voltage and I is the current. This may be represented in the Laplace domain as:

$$\frac{I}{V} = \frac{1}{Ls + R + \frac{1}{Cs}} \tag{3.11}$$

Thus the equivalent circuit values for the mechanical system is given by:

$$R = b \qquad C = \frac{1}{k} \qquad L = m \tag{3.12}$$

and Q is given by the relation:

$$Q = \frac{L\omega_0}{R} = \frac{1}{R}\sqrt{\frac{L}{C}} \qquad (3.13)$$

which is an expression analogous to Equation 3.6 in the mechanical domain.

In order to define a measure of the efficiency of the transduction mechanism that converts the electric driving voltage into the equivalent mechanical force, the ratio between the applied excitation force and the input signal applied is expressed by means of the coupling factor η_e. By ignoring the DC and 2ω components in Equation 3.3, the coupling factor results in the expression:

$$\eta_e = \frac{F}{v_{in}} = \frac{\partial C_{drive}}{\partial x}V_{DC} \approx \frac{C_{gap}}{g}V_{bias} \qquad (3.14)$$

where C_{drive} is the capacitance in the gap that varies with the position of the vibrating structure and C_{gap} is the approximated fixed capacitance in the gap. The equivalent RLC motional parameters can be related with the coupling factor as in Equations 3.15. Effective mass and stiffness have been previously named as m and k in this section, henceforth they will be renamed as m_{eff} and k_{eff} as a matter of concordance with literature [48] [54] [46].

$$
\begin{aligned}
R_m &= \frac{\sqrt{k_{eff}m_{eff}}}{Q\eta_e^2} = \frac{1}{Q}\frac{kg^4}{\epsilon^2\omega_0 A^2 V_{bias}^2} \\
C_m &= \frac{\eta_e^2}{k_{eff}} = \frac{1}{k}\frac{\epsilon^2 A^2}{g^4}V_{bias}^2 \\
L_m &= \frac{m_{eff}}{\eta_e^2} = \frac{mg^4}{\epsilon^2 A^2 V_{bias}^2}
\end{aligned}
\qquad (3.15)
$$

where A is the actuation area of the electrode facing the resonator body (see Figure 3.1).

Considering the circuit shown in Figure 3.4, at resonance the series motional values C_m and L_m cancel each other and the resulting admittance is:

$$Y_{res} = \frac{1}{R_m} + j\omega_0 C_0 \qquad (3.16)$$

In the ideal case, $R_m \ll 1/\omega C_0$ and the measured transmission S_{21} parameter can be related with the motional resistance. Assuming a loss-free (transmission $C_p = 0$), S_{21} can be expressed as a function of the power reflection as:

$$S_{21} = 20 log \left(\frac{2Z_0}{2Z_0 + R_m} \right) \tag{3.17}$$

where Z_0 is the characteristic impedance. A further analysis about the motional resistance extraction from measurements is provided in Appendix C.

3.2.3 Capacitive Detection

A complete equivalent electrical circuit representation of a two-port capacitively excited and detected MEMS resonator is provided in Figure 3.5.
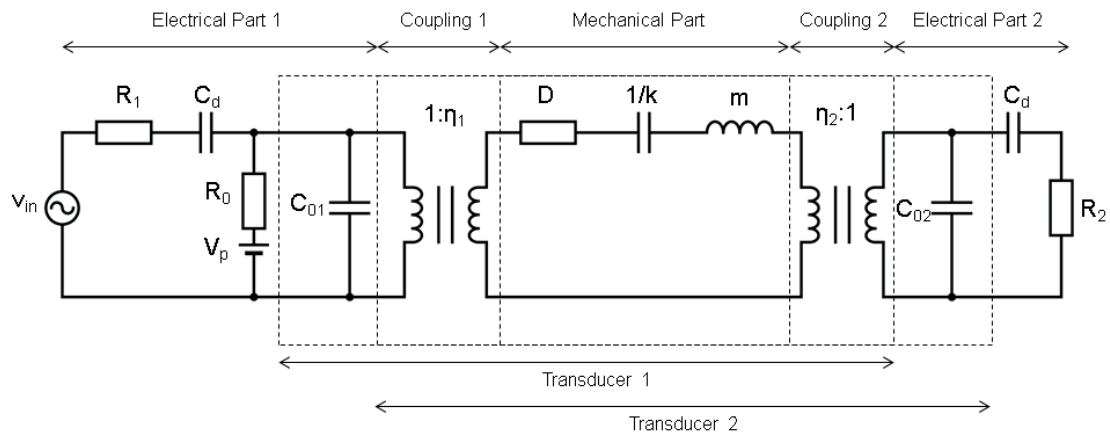
Figure 3.5 – Equivalent electrical circuit of a two-port MEMS resonator.

The drive capacitor is represented by C_0 while the RLC components model the mechanical mass-spring-damper system of the resonator. The movement of the resonator causes the gap capacitor to change its value, consequently inducing a current in the output read-out electrode that can be calculated as:

$$i_0 = \frac{\partial V_{bias} C}{\partial t} = C \frac{\partial V_{bias}}{\partial t} + V_{bias} \frac{\partial C}{\partial t} = V_{bias} \frac{\partial C}{\partial x} \frac{\partial x}{\partial t} \tag{3.18}$$

The derivative of the bias voltage vanished because V_{bias} is not time-dependent. A similar electromechanical coupling factor to the one introduced in Equation 3.14, can be defined for the readout coupling:

$$\eta_r = \frac{i_0}{\frac{\partial x}{\partial t}} \approx \frac{C_{gap}}{g} V_{bias} \tag{3.19}$$

The coupling factor states the relation between the output current and the displacement of the resonator. Normally, a symmetric coupling between the two domains is accomplished through the capacitive gap:

$$\eta_1 = \eta_e = \eta_2 = \eta_r \tag{3.20}$$

This symmetry is the reason why the squared coupling factor is normally introduced for calculations with equivalent RLC motional parameters (see Equation 3.15).

3.2.4 Piezoresistive Detection

Piezoresistive Effect

The electrical resistance (R) of a homogeneous structure is a function of its dimensions and resistivity (ρ):

$$R = \frac{\rho l}{a} \tag{3.21}$$

where l is the length and a is the average cross-sectional area. The change in resistance due to applied stress is a function of geometry and resistivity changes. The cross-sectional area of a bulk material reduces in proportion to the longitudinal strain by its Poisson's ratio, ν.

The gauge factor (GF) is defined as:

$$GF = \frac{\Delta R / R}{\epsilon} \tag{3.22}$$

where ϵ is strain and $\Delta R/R$ is the fractional resistance change with strain. Piezoresistance arises from the deformation of the energy bands as a result of an applied stress. In turn,

the deformed bands affect the effective mass and the mobility of electrons and holes, hence modifying the resistivity. The change in resistance is due to both the geometric effects $(1 + 2\nu)$ and the fractional change in resistivity $(\Delta\rho/\rho)$ of the material with strain [55]:

$$\frac{\Delta R}{R} = (1 + 2\nu)\epsilon + \frac{\Delta\rho}{\rho} \tag{3.23}$$

As it is shown in Equation 3.24, the fractional change in resistivity is to a first order linearly dependent on the two stress components parallel (longitudinal stress) and orthogonal (transversal stress) to the direction of the resistor, σ_L and σ_T, respectively. The direction of the resistor is defined as that of the current flow.

$$\frac{\Delta\rho}{\rho} = \pi_L\sigma_L + \pi_T\sigma_T \tag{3.24}$$

where π_L and π_T are the so-called longitudinal and transversal piezoresistive coefficients, respectively, and are related to GF by the Young's modulus of the material.

In silicon, the piezoresistive coefficients are dependent on crystal orientation and can change significantly from one orientation to the other. They also depend on the dopant type (n-type versus p-type) and concentrations [56]. Tensile strain causes the silicon atoms to be pulled further apart making it easier for electrons to move through the silicon. On the other hand moving the atoms further apart makes it harder for holes to move because holes require bound electrons to move from a silicon atom to a neighboring silicon atom in the opposite direction, which is more difficult if they are further apart. Thus tensile strain increases mobility in n-type silicon and compressive strain increases mobility in p-type silicon.

An interesting graphical representation of the piezoresisitance coefficients in silicon can be found in [57]. The piezoresistance coefficients for n-type silicon ($\rho = 11.7$ Ω·cm) and p-type silicon ($\rho = 7.8$ Ω·cm) are listed in Table 3.2 (carrier flow in <110> direction) and 3.3 (carrier flow in <100> direction).

Taking into consideration the piezoresistive coefficients shown above, mobility can be increased or decreased depending on the type of strain (tensile, compressive) and the direction of strain relative to crystal orientation and current flow. For p-type (100) wafers (which are the

Table 3.2 – Piezoresistance coefficients in the <110> direction for n-type and p-type silicon [57].

<110> direction	π_L (10^{-11}/Pa)	π_L (10^{-11}/Pa)
n-type	-31.6	-17.6
p-type	71.8	-66.3

Table 3.3 – Piezoresistance coefficients in the <100> direction for n-type and p-type silicon [57].

<100> direction	π_L (10^{-11}/Pa)	π_L (10^{-11}/Pa)
n-type	-102	53.4
p-type	6.6	-1.1

ones used for the fabrication presented in Chapter 4) and current flow in <110> direction: (1) compressive strain in the direction of current flow enhances mobility of holes and (2) tensile strain transverse to current flow enhances mobility of holes.

Piezoresisitive detection in MEMS resonators

MEMS resonators can be designed taking into consideration the crystalographic directions of silicon in order to maximize piezoresisitive coefficients when the devices are vibrating in a certain in-plain direction (and hence undercoming tensile and compressive strain).

In [40], an approximate analytical model was developed to relate the stresses in the resonator bulk (i.e. suspended square plate) for the square extensional mode to the change in resistance between the two diagonal corners of the square plate. The side edge of the square is aligned to the <110> direction, with the current flow diagonally across two anchors in the <100> direction, where π_L is maximized for n-type silicon. The square can be thought of as numerous resistors connected in parallel and series diagonally as illustrated in Figure 3.6.

Output currents for capacitively actuated MEMS resonators have been proven to be of orders of magnitude larger for capacitive-piezoresistive detection than for capacitive detection depending on the biasing conditions [11].

As it is depicted in Figure 3.7 for a beam-type resonator, the total output current obtained from a device at resonance has two contributions: (a) a capacitive current depending on the capacitance changes in the transduction gap i_{cap} and (b) a piezoresistive current tuned by
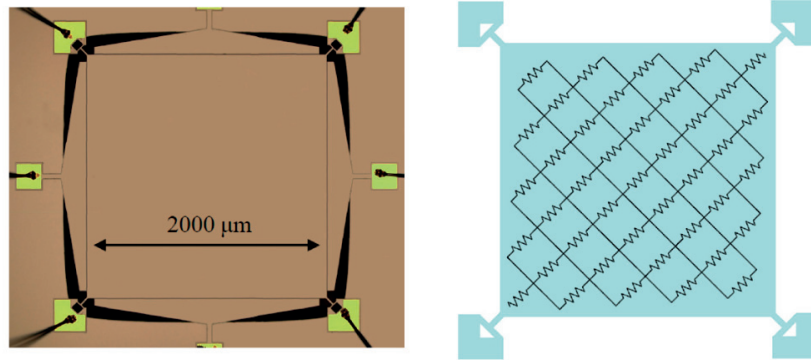
Figure 3.6 – (Left) Optical micrograph of the square resonator fabricated b and (rigt) diagram illustrating the parallel and series resistance in the square resonator [40].

mechanical strain changes biased by the stretching of the resonator body i_{res}.
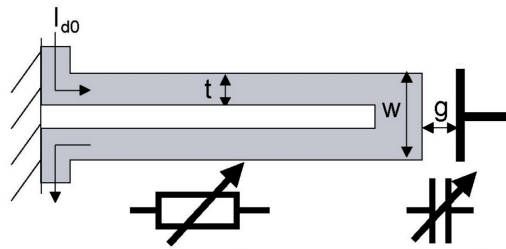
Figure 3.7 – Schematic of a beam-type resonator capacitively actuated and capacitively-piezoresistively sensed [11].

From Figure 3.7 it can be seen that the two components to the output current are proportional to [11]:

$$i_{cap} \propto v_{in} h w^2 \frac{w}{tg^4} \qquad i_{res} \propto v_{in} \frac{w}{tg^2} \qquad (3.25)$$

where w and t are the beam dimensions, h is the thickness and g is the gap as indicated in Figure 3.7.

3.2.5 Transduction Gap: Air and Filled-Gap Discussion

Taking into account Equation 3.15, it is evident that in order to reduce the motional resistance and adjust it to the 50 Ω characteristic impedance standard, the main ways to accomplish it are: (1) reducing the stiffness of the structure, that mainly depends on the material and the

device dimensions for the desired resonance frequency; (2) increasing the Q-factor, which depends on damping nonlinearities that are difficult to control (see Sections 3.2.7 and 3.2.6); (3) increasing the actuation area, that depends on the device dimensions and the structural material thin layer; (4) increasing the bias, that is highly discouraged to keep low the power consumption of the resonator; (5) increasing the resonance frequency, that is a intrinsic parameter of the final application of the device and finally (6) decreasing the gap dimension or (7) filling the transduction gap with a material whose dielectric constant is greater than air ($\epsilon_r > 1$).

Focussing on (6), as it is shown in Equations 3.14, 3.18 and 3.15, by scaling the gap the coupling factor and the resulting output capacitive current are increased (gap dimension dependence elevated to the second power) and therefore the motional resistance decreases (gap dimension elevated to the fourth power).

Nevertheless, achieving sub-micron gaps might not be so straightforward due to the limits coming from the fabrication technology itself [58] [59] [60]. Some authors proposed solid-gap MEMS resonators mainly to low the motional resistance, better stabilize the structure against shock and microphonics and eliminate the possibility of particles getting inside of the gap [61].

Table 3.4 – Dimensions and resonance frequency of the resonators of Figure 3.8.

Device	Radius, R (μm)	Thickness, t (μm)	Gap, g (nm)	f_0 (MHz)
WGD1	10	2	200	189
WGD2	5	1	50	394

Two silicon WGD resonators analytically design to vibrate in the VHF and UHF ranges have been simulated with COMSOL®Multiphysics and their simulated resonance frequencies have been extracted (see Table 3.4). Figure 3.8 depicts the analytical calculations that have been performed to study the theoretical motional resistance R_m, (as introduced above in Equation 3.48) with respect to the supply bias, V_{bias}, and two chosen Q-factors for air and solid transduction gaps based in different high-k materials (HfO_2 and Si_3N_4).

If we compare WGD1 with WGD2 by taking into account solid-gaps of Si_3N_4, same Q-factor (Q = 1000) and V_{bias} range from 1 to 40 V, (cyan diamonds and cyan squares), we can see a
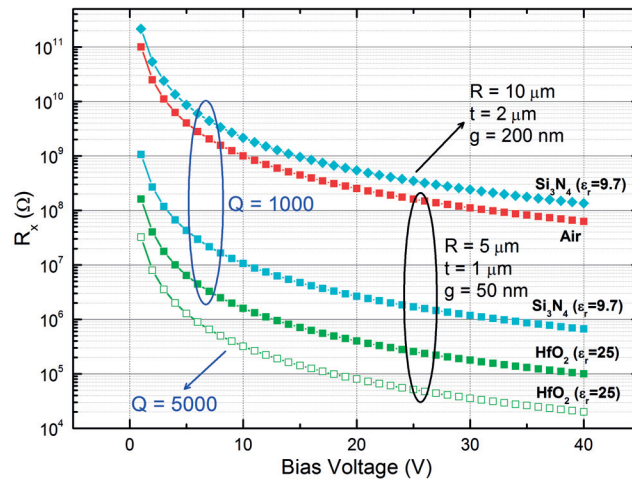
Figure 3.8 – Motional resistance, R_m, in function of the bias voltage, V_{bias}, from analytical calculations for different air and solid-gap WGD resonators. Cases from up to bottom lines: (cyan diamonds) WGD1 with Si_3N_4 solid-gap and considered Q = 1000; (red squares) air-gap and considered Q = 1000; (cyan squares) WGD1 with Si_3N_4 solid-gap and considered Q = 1000; (green solid squares) WGD1 with HfO_2 solid-gap and considered Q = 1000 and (green empty squares) WGD1 with HfO_2 solid-gap and considered Q = 5000.

theoretical reduction in the extracted R_m larger than two orders of magnitude mainly due to the gap scaling (from 200 nm to 50 nm). An enhancement in R_m up to three orders of magnitude can be theoretically obtained due to gap-filling can be observed for Q = 1000 by comparing the resulting calculations obtained for WGD2 with air (red squares), Si_3N_4 (cyan squares) and HfO_2 (green solid squares) gaps. The experimental effect of high-k gap-filling is widely studied in Chapter 4.

The equivalent capacitance of the gap for different gap-filling options as (a) air, (b) partially-filled and (c) solid gaps, have been analytically calculated and they are shown in Figure 3.9. The output current enhancement for partially-filled and solid gaps (b-c) can be clearly observed by taking into consideration Equations 3.18, 3.14 and 3.19.

3.2.6 Nonlinear Dynamics Effects

There are many sources of nonlinearities in MEMS, which are due to forcing, damping, and stiffness, (see Figure 3.10). They are detailed below [48].
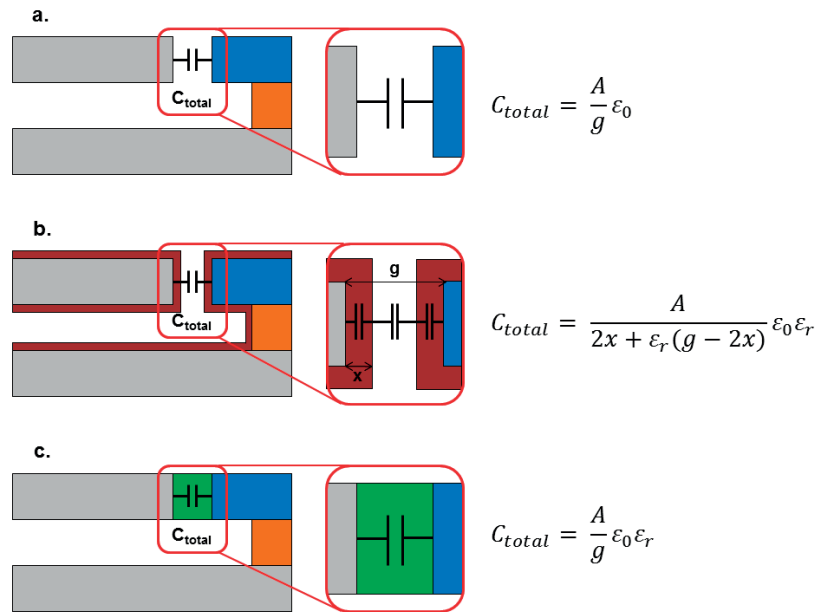
Figure 3.9 – Section view of the resonator-electrode gap. Total capacitance have been analytically calculated for (a) air (b) partially-filled and (c) solid transduction gap.
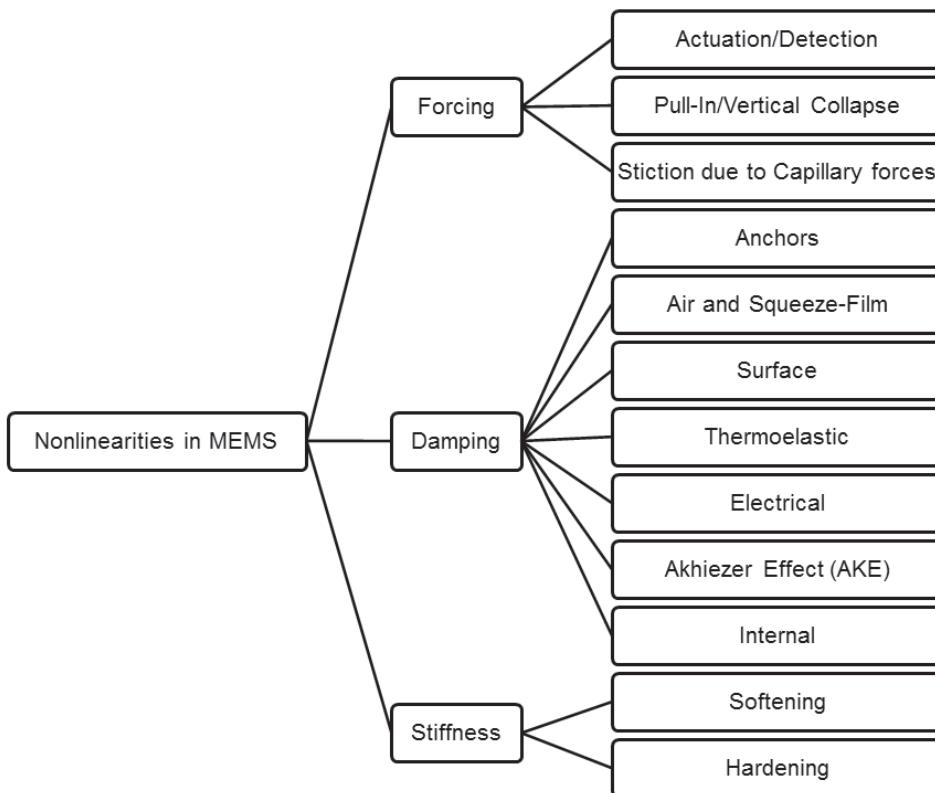
Figure 3.10 – Common sources of nonlinearities in MEMS.

Forcing

- **Pull-In Instability**

  An important effect that must be taken into account with in-plane resonators with capacitive excitation is the stiction of the resonator body with the electrodes (effect that is known as lateral pull-in) or to the substrate (vertical collapse) [62].

  For a two-port capacitively actuated resonator, the sum of the total forces presented in the system comes from the addition of the electrostatic force ($F_{electrostatic}$) and the elastic recovery force ($F_{elastic}$):

  $$F_{total} = F_{electrostatic} + F_{elastic} =$$
  $$= \frac{1}{2}\epsilon A V_{bias}^2 \left(\frac{1}{(s-x)^2} - \frac{1}{(s+x)^2}\right) + kx \tag{3.26}$$

  For a two-port resonator x = 0 is the stable equilibrium point in which F_{total} = 0 . In normal operation, the mechanical elastic force is larger than the electrostatic elastic force and therefore the resonator displaces until the condition $F_{elastic}$ = $F_{electrostatic}$ is reached. When the electrical force becomes larger than the mechanical one, the resonator is attracted to the electrode untill it collapses. In order to find the maximum applicable voltage, the stability condition $\frac{\partial F_{total}}{\partial x}$ can be applied [63]. For simplicity, stability is computed at x = 0 and the extracted pull-in voltage is [64]:

  $$V_{pull-in}^{two-port} = \sqrt{\frac{kg^3}{2\epsilon A}} \tag{3.27}$$

- **Vertical Collapse**

  Vertical collapse can be produced either by the technological fabrication process (specially during the release of the structure) or by the application of external forces (acceleration or electrostatic attraction). By biasing the necessary DC voltage for the actuation of the device, the resonator is affected by a vertical electrostatic attraction to the substrate. In the case of a clamped-clamped beam (CCB) resonator, the maximum applicable voltage to the resonator for preventing vertical collapse of the movable structure is given

by [62]:

$$V_{vertical-collapse} = \sqrt{11.9 \frac{D^3 t^3}{\epsilon l_b^4}} \tag{3.28}$$

where D is the vertical distance to the substrate and l_b is the length of the beam. A standard way to avoid vertical collapse is to keep the suspended body of the resonator always at the same potential as the bulk substrate.

- **Stiction due to Capillary Forces**

  Wet etching of sacrificial layers to release microstructures from the substrate is an important step in the fabrication of many MEMS structures and devices. During drying, the rinse liquid trapped underneath the microstructures creates strong capillary forces pulling them toward the substrate. Humidity can also cause condensation of liquid in working devices. Because of their large surface areas, some microstructures can collapse against the substrate if the capillary forces are greater than their restoring forces.

Damping

In this section, we are going to discuss the dissipation mechanisms (including damping due to air, anchors, surface phenomena, electronic and thermoelastic dissipation and phonon scattering (Akheizer dissipation).

- **Anchors Damping**

  Structural losses are caused by damping effects in the coupling between the resonator structure and the surrounding solid. One important way to reduce the energy loss through the anchors is to minimize the forces applied to the anchors during the oscillation cycle. To minimize anchors damping several measures can be taken, such as: (1) decoupling of the resonator and its supporting structure, using the nodal points to anchor the resonator and to design a balanced system [49] [65]; (2) designing the anchors length with quarter-wavelength dimensions so as to affect an impedance transformation that isolates the device from the rigid anchors [66] and (3) considering anchors geometries that reduce the anchors clamping [67] [68].. Minimizing the structural losses

provides also the advantages of having a good frequency resolution, a good immunity against environmental influences and therefore an improved long-term stability of the system.

Regarding to (2), the anchors length (l_a) is defined as:

$$l_a = \frac{\lambda}{4} = \frac{1}{4f_0}\sqrt{\frac{E}{\rho}} \tag{3.29}$$

where f_0 is the resonance frequency of the device and E and ρ are the Young's modulus and density of the structural material, respectively.

- **Air Damping**

  Because of the small size of the resonating structure in an MEMS resonator, there can be a relatively large amount of surface area relative to the volume. Unless the resonator is packaged at extremely low pressure, the ambient gas surrounding the resonator impedes the motion of the resonating element. Because of the movement of the resonating element relative to the surrounding air molecules, energy can be transferred from the resonator to the surrounding air, leading to a loss mechanism known as air damping. As a result, air damping is generally proportional to the air pressure. Depending on the resonator motion being normal to or parallel to the nearby surfaces, damping may be described as *squeeze film damping* (see Figure 3.11) or *shear film damping*, respectively [49].
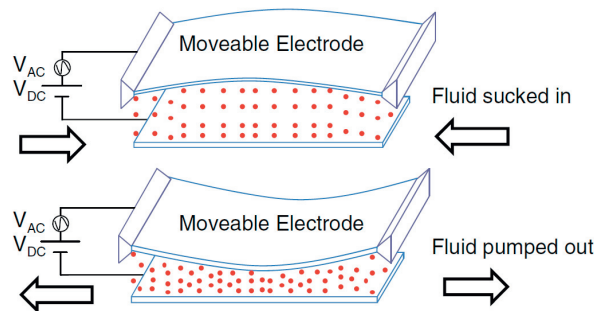
Figure 3.11 – Squeeze-film damping in a parallel-plate capacitor. This phenomenon occurs as a result of the massive movement of the fluid underneath the plate, which is resisted by the viscosity of the fluid, giving rise to a pressure distribution underneath the plate [48].

- **Surface Damping**

  With increasing surface-to-volume ratio of small resonators the surface effects increase causing energy dissipation. This mainly results from atoms and molecules on the surface of the resonator interacting with the surrounding medium. This damping mechanism counts as internal and is also material related. This effect can be influenced by treating the surface of the resonator to have desired properties to minimize the surface damping effect. [49].

- **Thermoelastic Damping (TED)**

  This is caused by scattering of acoustic phonons with thermal phonons, while the resonator is taken out of its equilibrium state and the material is elastically compressed and decompressed. In the process a thermal gradient is created increasing the entropy of the system and leading to energy dissipation, because the compressed areas heats up and the decompressed areas of the resonator cools down. This damping mechanism is influenced by the material, its impurity level and grain boundaries. It can only be controlled in a limited way by choosing the appropriate material with certain impurity level for the desired application [48] [69].

- **Akhiezer Effect (AKE)**

  During the actuation of the microstructure, the crystal lattice undergoes expansion. This expansion leads to an increase in the wavelength for all the phonon modes of the crystal, and anharmonicity of the lattice bonds leads to a slight reduction in the frequencies and the energies of all these modes. Therefore, the applied electrostatic field modulates the frequency of the thermal phonons. The resulting temperature difference between different phonon modes tends to relax toward a mean temperature value. This results in an intramode heat flow and hence in dissipation.

- **Electrical Damping**

  Whenever a structure with some trapped charges is positioned near a conductive surface, there are image charges induced on the conductive surface. If the structure is moving, such as a micromechanical resonator, the movement of the trapped charges will cause a corresponding movement of the image charges in the adjacent surface. If there is finite electrical resistivity in that adjacent surface, the movement of the charges will be

resisted by ohmic losses, and these losses will reduce the Q-factor of the resonator. This general mechanism can be important anytime there are trapped charges in a resonating structure or in a nearby structure. The trapped charges always induce image charges, and the movement of the trapped charges will induce movement of the image charges, leading to ohmic losses.

- **Internal Damping**

  It is associated with the dislocations, purity and microfabrication defects of the material used. As the top silicon layer of the SOI wafer is an ideal monocrystalline material, the dislocations and the impurity are negligible in comparison with the other sources of damping described above.

Stiffness

When actuated, microstructures undergo relatively large motion, which amplifies the so-called geometric nonlinearities. When the relative motion is comparable to the thickness and size of the structure, geometric nonlinearities lead to significant changes in its stiffness and dynamical behaviours.

- **Spring Softening and Hardening**

  Two recognized nonlinear phenomena existing in electrostatically actuated MEMS resonators are spring softening (electrostatic nonlinearity) and spring hardening (mechanical nonlinearity). Taking as example the cantilever-nanotube shown in Figure 3.12 [70], spring softening exhibits a resonance frequency decrease when amplitude of oscillation increases, contrary to spring hardening, which shows a resonance frequency increase with increasing oscillation amplitudes [71].

  These two phenomena occur simultaneously, but generally one of them dominates the other depending on the conditions dictated on the structure (i.e., excitation voltage, resonator structure and dimensions, etc.). These nonlinear effects can be used in order to tune the detected frequency to match with the designed one, that may have changed due to the fabrication imperfections.

(a) Spring softening
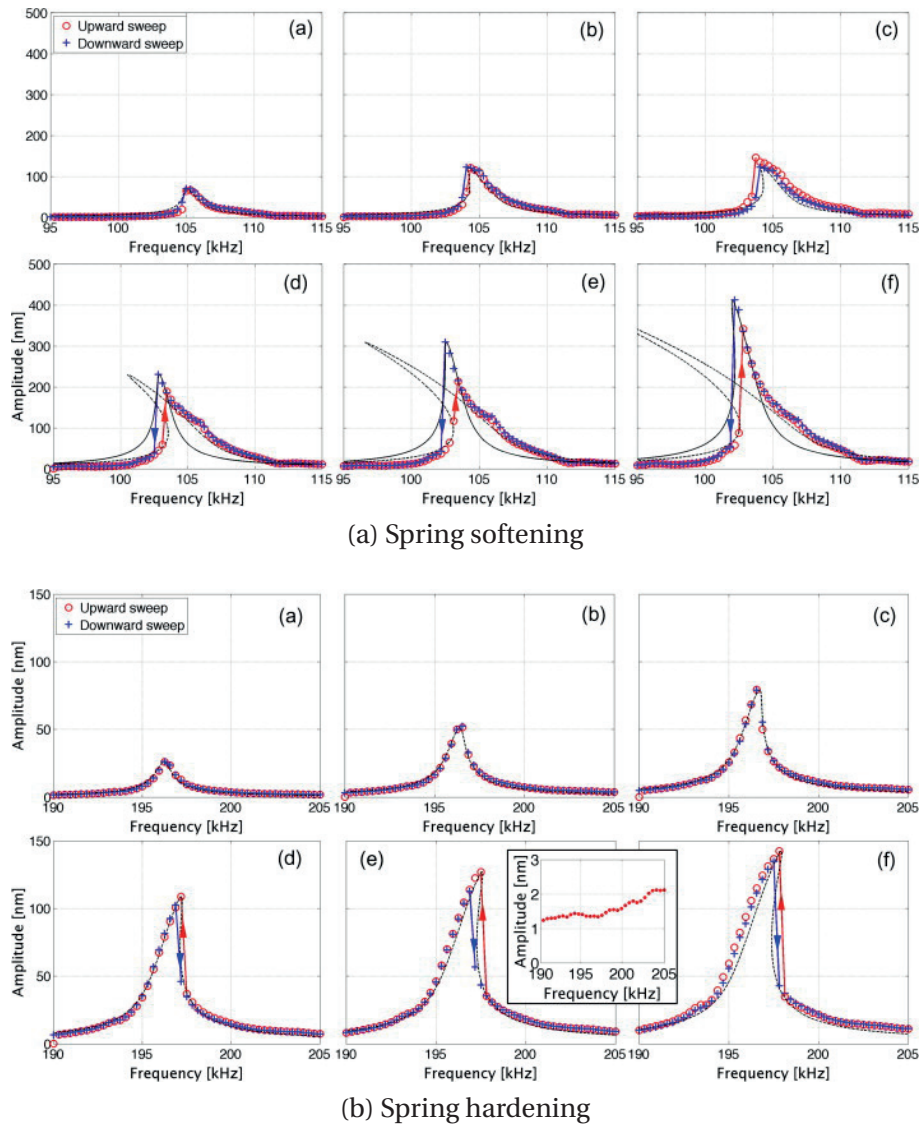
(b) Spring hardening

Figure 3.12 – Experimentally acquired spring (a) softening and (b) hardening for a cantilever-nanotube by increasing the driving amplitude [70].

When a resonator is affected by spring nonlinearities, the effective stiffness k_{eff} is defined as [72]:

$$k_{eff} \approx k_{m1} - k_{el1} + (k_{m3} - k_{el3})x^2 \qquad (3.30)$$

where k_{m1} and k_{m3} are the linear and third order mechanical spring constants and k_{el1} and k_{el3} are the linear and third order electrical spring constants.

Different stiffness adjustment methods have been recently proposed in literature [73]: (1) electrostatic tuning; (b) anchors design and dimensioning; (2) changing second moment of inertia; (3) stressing the structure and (4) changing Young's modulus by increasing the temperature.

Taking into account (2) the stiffness of a system can be increased by engaging an increasing number of anchors in the nodal (or pseudonodal) points of a vibrating [73]. This is an extremely interesting effect in the case of the bulk resonators presented in this work that it is more extensively treated in Section 3.4 and Chapter 4.

3.2.7 Quality Factor

Mechanical quality factor (Q-factor or Q) of a micromechanical resonator is a dimensionless parameter that models the losses in the vibrating structure. It is defined as the ratio between the energy stores and the energy dissipated per cycle:

$$Q = 2\pi \left(\frac{Energy_{stored}}{Energy_{dissipated-per-cycle}} \right) \qquad (3.31)$$

As Q-factor is a measurement of the discrimination of the signals at a given frequency to other signals, it may be considered as a measurement of the selectivity of the device: the higher the Q-factor, the narrower the selectivity. The Q-factor is also defined as the ratio between the resonance frequency and the width of the resonance peak as:

$$Q = \frac{f_0}{BW} \qquad (3.32)$$

where f_0 is the center-frequency of the peak and BW is the half-power (or 3 dB bandwidth)

around f_0. It is straightforward to interpret this definition as a measurement of the sharpness of the resonance: the higher the Q-factor, the sharper the response in resonance of the micromechanical resonator.

Q-factor is inversely proportional to the damping constant (Equation 3.6). By taking into consideration the loses sources discussed in Section 3.2.6, a Q-factor calculation can be addressed as:

$$\frac{1}{Q} = \frac{1}{Q_{anchors}} + \frac{1}{Q_{air}} + \frac{1}{Q_{surface}} + \frac{1}{Q_{TED}} + \frac{1}{Q_{AKE}} + \frac{1}{Q_{electrical}} + \frac{1}{Q_{internal}} \qquad (3.33)$$

For MEMS resonators operating in air, Q is limited by the air damping, Q_{air}^{-1}, while in a vacuum ambient, the main losses are due to the supporting anchors, $Q_{anchors}^{-1}$, with surface effects, $Q_{surface}^{-1}$, TED, Q_{TED}^{-1}, AKE, Q_{AKE}^{-1} and electrical, $Q_{electrical}^{-1}$, and internal, $Q_{internal}^{-1}$ damping playing a minor role.

Apart from the common definitions of the Q-factor that have been already introduced in Equation 3.31 and 3.32, the Q-factor of a resonator can be also extracted from the slope of the phase response at resonance [54] [74] [75]. The region of highest slope is at resonance where the phase response is approximately linear, therefore the Q-factor approximated by the phase-slope Q_{ph} is given by:

$$Q \approx Q_{ph} = \frac{\omega_0}{2} \frac{d\phi}{d\omega} \qquad (3.34)$$

where ω_0 is the natural resonance frequency of the device and $\frac{d\phi}{d\omega}$ is the slope of the phase at resonance. This expression is particularly useful to obtain an approximation of the Q-factor whenever no magnitude resonance peak higher than 3 dB is measured. A detailed experimental analysis of this method in comparison with the one based on BW (Equation 3.32) is included in Appendix A.

3.3 Analytical Models

In this section the analytical models for the flexural (clamped-clamped beam, double-ended tuning fork and parallel beam) and bulk (wine-glass disk and square plate) resonators considered in this work are discussed.

3.3.1 Clamped-Clamped Beam (CCB) Resonator

The electrostatic beam resonator consists of a single clamped-clamped beam (CCB) and a couple of actuation-detection electrodes in two-port configuration (see Section 3.2.3). Figure 3.13 presents the perspective view of a CCB resonator together with its main geometrical parameters: beam length (l_b) and width (w_b), transduction gap (g) and device thickness (t).
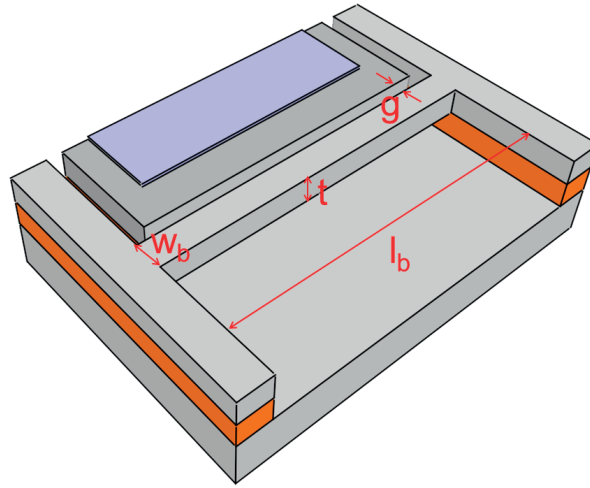
Figure 3.13 – Perspective view of a clamped-clamped beam micromechanical resonator. One of the electrodes has been removed to ease the resonator body visualization.

In order to calculate the resonance frequency of the CCB resonator, the Euler-Bernoulli beam equation with electrostatic forces is simplified as [76]:

$$\rho w_b t \frac{\partial^2 w}{\partial t^2} + E I_{CCB} \frac{\partial^4 w}{\partial x^4} = -v_{ac} \frac{\epsilon_0 t c_f f_e(x) V_{bias}}{g^2} \tag{3.35}$$

where E is the Young's modulus, ρ is the material density, I_{CCB} is the bending moment of inertia of the beam, c_f is a fringing field correction factor [77] and V_{bias} and v_{ac} are the DC and AC actuation voltages, respectively. $f_e(x)$ is a factor in function of the electrodes length

defined in Equation 3.36:

$$f_e(x) = \begin{cases} 0 \text{ for } x < \frac{l_b - l_{electrode}}{2} \\ 1 \text{ for } \frac{l_b - l_{electrode}}{2} \leq x \leq \frac{l_b + l_{electrode}}{2} \\ 0 \text{ for } x > \frac{l_b + l_{electrode}}{2} \end{cases} \tag{3.36}$$

where $l_{electrode}$ is the electrode length.

By solving Equation 3.35, the fundamental resonance frequency is defined as:

$$f_0 = \frac{\pi}{2} \beta_{CCB}^2 \sqrt{\frac{E}{12\rho}} \frac{w_b}{l_b^2} \tag{3.37}$$

with the experimental coefficient $\beta_{CCB} = 1.506$ [77].

Normally the mechanical spring constant of a CCB linear can be approximated by means of its linear component as:

$$k_{m1} = \frac{48 E I_{CCB}}{l_b^3} \tag{3.38}$$

where the moment of inertia can be calculated by solving the Equation 3.35 as [5]:

$$I_{CCB} = \frac{w_b t^3 + w_b^3 t}{12} \tag{3.39}$$

Considering Equation 3.15 and 3.6 and the approximation $k_{eff} \approx k_{m1}$, the motional resistance for a CCB resonator can be calculated as:

$$R_m = \frac{k_{m1}}{w_0} \frac{1}{\eta_e^2 Q} \tag{3.40}$$

3.3.2 Double-Ended Tuning Fork (DETF)

The basic layout of a double ended tuning fork (DETF) resonator consists of two parallel straight tines anchored to each other and at the substrate at each end. External electrodes parallel to the beams electrostatically drive each tine in a lateral motion to carry out an flexural

in-plane mode of resonance. The dimensions of the DETF resonator described in Figure 3.14 are: beam length (l_b) and width (w_b), tines separation length (l_h) and width (w_h), anchors length (l_a) and width (w_a), transduction gap (g) and device thickness (t).
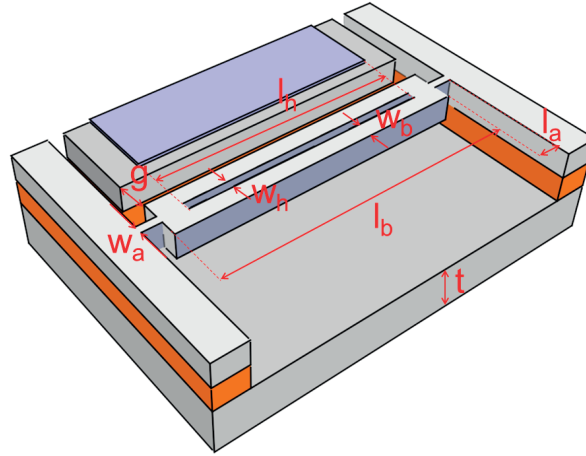
Figure 3.14 – Perspective view of a DETF resonator sketched with one actuation electrode.

As long as the DEFT is symmetric and the mode of vibration is parallel to the anchoring substrate, the frequency analysis can be reduced to an examination of the tines. Furthermore, if each tine fulfills the condition $l_b/w_b > 10$, then their vibrational characteristics can be determined using Bernoulli-Euler beam theory [78]. Applying a clamped-clamped boundary condition and assuming that there is no external shear force, the fundamental resonance frequency f_0 for a DETF resonator can be expressed as:

$$f_0 = \frac{1}{2\pi}\sqrt{\frac{16.55Ew_b^2 + 4.85El_b^2\epsilon_0}{0.4\rho l_b^4}} \tag{3.41}$$

The moment of inertia and effective mass of the DETF are considered as [78]:

$$I_{DETF} = \frac{w_b^3 t}{12} \qquad m_{eff} = 0.4\rho w_b t l_b \tag{3.42}$$

Same procedure than in Section 3.3.1 can be done in order to extract an expression for the motional resistance of the DETF resonator.

3.3.3 Parallel Beam Resonator (PBR)

A parallel beam resonator (see Figure 3.15) consists in a two-port rectangular membrane fragmented by parallel longitudinal rectangular holes that enable the resonator to operate as a multi-beam structure vibrating in length extensional mode. The dimensions of the PBR described in Figure 3.15 are: beam length (l_b) and width (w_b), length of the added mass due to inter-beams connections (l_m) and width (w_m), anchors length (l_a) and width (w_a), transduction gap (g), resonator length (l_{res}) and device thickness (t).
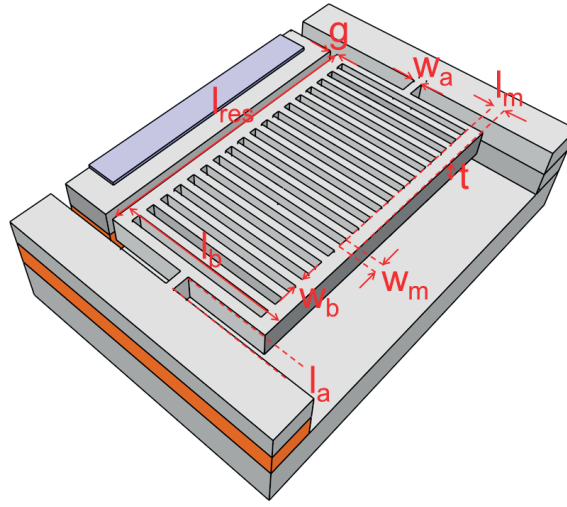
Figure 3.15 – Perspective view of a PBR schematic with one actuation electrode.

The natural resonance frequency f_0 of this microstructure is dictated by the geometry of the resonators length (l_{res}), while the Q-factor, coupling capacitance and motional resistance are related to the number of connected beams [35].

The effective mass at f_0 is expressed as:

$$m_{eff} = N\frac{l_b w_b t \rho}{2} + 2(N-1)l_m w_m t \rho \tag{3.43}$$

where l_m and w_m are respectively the length and width of the connecting element. The effective spring constant can be approximated as:

$$k_{eff} \approx k_{m1} = N\frac{\pi^2 E w_b t}{2l_b} \tag{3.44}$$

By means of Equations 3.43 and 3.44, both f_0 and R_m can be derived. Nevertheless, the mass loading corresponding to beam parallel connections resulting in a more straightforward approximation by means of the expression:

$$f_0 \approx \frac{\beta_{PBR}}{2l_b} \sqrt{\frac{E}{\rho}} \tag{3.45}$$

where l_b is the beam lengths (see Figure 3.15) and $\beta_{PBR} = 0.942$ is an experimental factor that reflects the k_{eff}/m_{eff} ratio deviation from the single-beam model due to the added mass [79].

3.3.4 Wine-Glass Disk (WGD) Resonator

In order to excite wine-glass bulk mode of resonance in a suspended disk, the electrodes configuration as the one of Figure 3.16 is normally considered [80]. The depicted geometrical dimensions for WGD resonator are: radius (R) realising holes width (w_h), inter-holes spacing (s), anchors length (l_a) and width (w_a).
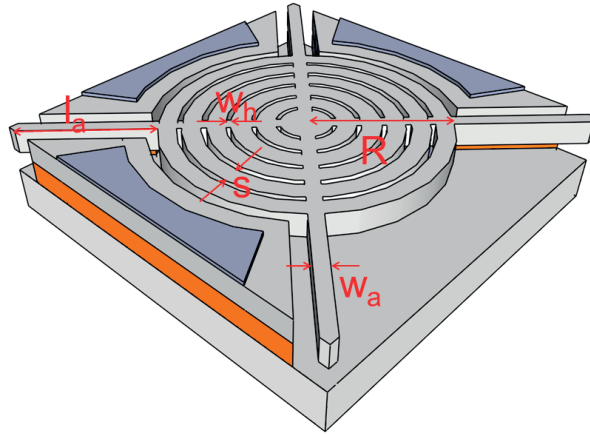
Figure 3.16 – Perspective view of a bulk WGD resonator with releasing holes performed to ease the realising step of the suspended structure during fabrication.

The resonance frequency f_0 for a wine-glass mode disk can be obtained by solving the mode frequency equation given by [81]:

$$[\Psi_2(\frac{\zeta^2}{\xi}) - 2 - q][2\Psi_2(\zeta) - 2 - q] = (nq - n)^2 \tag{3.46}$$

where:

$$q = \frac{\zeta^2}{2n^2 - 2} \qquad \zeta = R\sqrt{\frac{2\rho\omega_0^2(1+\sigma)}{E}} \qquad \xi = \sqrt{\frac{2}{1-\sigma}} \qquad (3.47)$$

where n is the mode of resonance, and ρ, σ and E are the density, Poisson's ratio and Young's modulus of the disk structural material, respectively. In order to obtain the value for the motional resistance of a WGD vibrating, Equations 3.14 and 3.15 are taken into consideration. The equivalent mass m_{eff} at a location (r, θ) of a disk vibrating in wine-glass mode can be obtained by dividing the total kinetic energy by one-half the square of the velocity at that location. Doing so for the case of a location (R_{disk}, θ) on the perimeter of the disk, the equivalent mass can be approximated as it is shown in Equation 3.48 [80] [82] [83].

$$m_{eff} = \frac{\rho \pi t \int_0^{R_{disk}} [\frac{G}{2r}J_1(G) - \frac{G}{2r}J_3(G) + \frac{2B}{AR_{disk}}J_2(G\xi)]^2 r \, dr}{[\frac{G}{2r}J_1(\frac{\zeta}{\xi}) - \frac{G}{2r}J_3(\frac{\zeta}{\xi}) + \frac{2B}{AR_{disk}}J_2(\zeta)]^2} \qquad (3.48)$$

where:

$$G = \frac{\zeta r}{\xi R} \qquad \frac{B}{A} = -4.5236 \qquad (3.49)$$

where $J_n(x)$ is the Bessel function of first kind of order n = 1, 2 ,3 and r concerns the radial polar coordinate of the disk.

3.3.5 Square Plate Resonator (SPR)

In order to actuate a squared plate, the resonator is anchored at the four nodal points to suppress energy loss through the anchors (see Section 3.2.6) as it is sketched in Figure 3.17. The square plate dimensions are: side (l_p) realising holes width (w_h), inter-holes spacing (s), anchor length (l_a) and width (w_a).

The resonance frequency f_0 for square plate vibrating in its Lamé mode is described as:

$$f_0 = \frac{1}{\sqrt{2}l_p}\sqrt{\frac{G}{\rho}} \qquad \text{(Lamé Mode)} \qquad (3.50)$$

where ρ is the density and G is the shear modulus of the material, that is related with Young's

modulus, E and Poisson's ratio, v by means of the expression:

$$G = \frac{E}{2(1+v)} \tag{3.51}$$

The spring constant and effective mass of a square plate vibrating in its Lamé mode of resonance can be calculated according to the expressions: [84]:

$$k_{eff} \approx k_m = \pi^2 c_{44} t \qquad m_{eff} = \frac{1}{2} \rho t l_p^2 \tag{3.52}$$

where c_{44} denotes the elastic stiffness parameter of crsytalline silicon with <100> orientation [85].
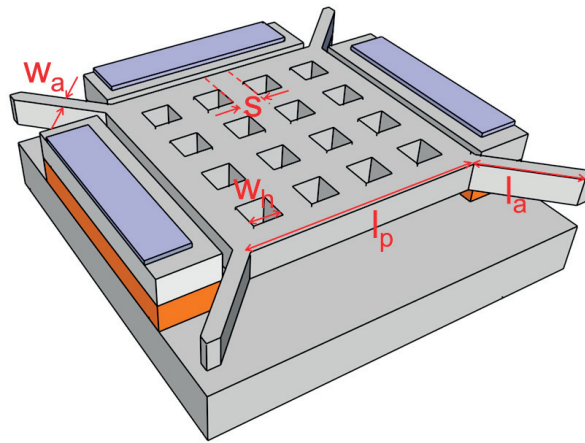
Figure 3.17 – Perspective view of a square plate resonator with three actuation electrodes.

Nevertheless, other modes of resonance that can be exploited in square plate resonators are the square plate extensional bulk mode [86] and the square plate flexural [87] that can be respectively calculated as:

$$f_0 = \sqrt{\frac{E}{4\rho l_p^2}} \qquad \text{(Extensional Mode)} \tag{3.53}$$

$$f_0 = \frac{20.56}{2\pi} \frac{t}{l_p^2} \sqrt{\frac{E}{12\rho(1-v^2)}} \qquad \text{(Flexural Mode)} \tag{3.54}$$

3.4 Finite Elements Method (FEM) Model

In this section the FEM models fulfilled by means of COMSOL®Multiphysics for the flexural (clamped-clamped beam and double-ended tuning fork) and bulk (wine-glass disk, parallel beam and square plate) resonators considered in this work are discussed and compared with the theoretical results (see Section 3.3).

3.4.1 Clamped-Clamped Beam (CCB) Resonator

Modal electromechanical FEM simulations were carried out for a CCB of l_b = 70 μm, w_b = 4 μm and t = 1 μm and the first four modes of resonance of the device are included in Figure 3.18. Taking into account the CCB schematic presented in Figure 3.3.1, the resonance mode that is preferentially excited in such a structure is the first flexural-lateral mode, that is named as f_0.

1st Mode	2nd Mode	1st Mode	3rd Mode
Flexural-Vertical	Flexural-Vertical	**Flexural-Lateral**	Flexural-Vertical
f_1 = 1.8MHz	f_2 = 4.95MHz	**f_1 = 7MHz**	f_3 = 9.7MHz
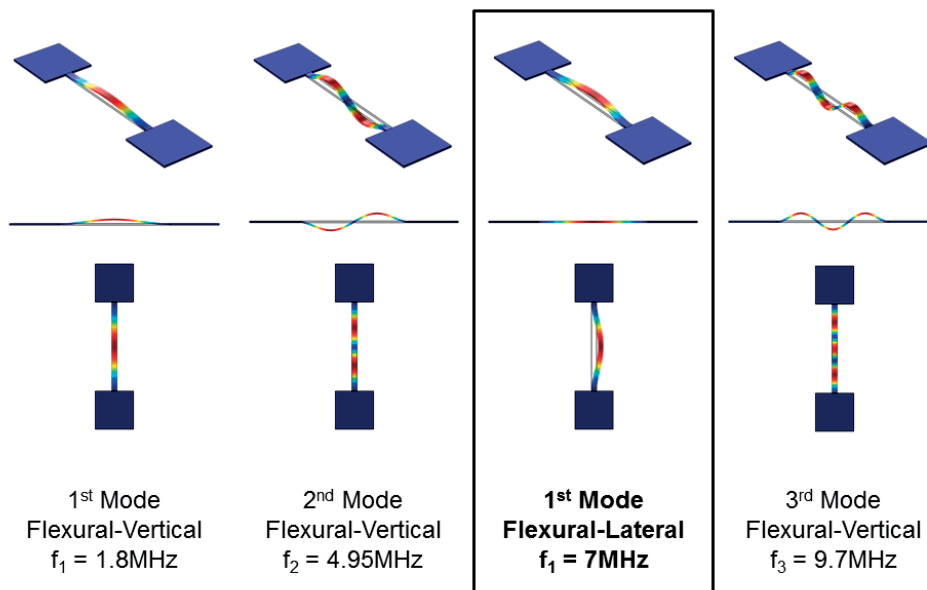
Figure 3.18 – First four modes of resonance of the simulated CCB (all in perspective, lateral and top views). Material: Silicon ϵ_r = 11.7, E = 169 GPa, ν = 0.22, ρ = 2329 $\frac{kg}{m^3}$ (these properties are considered in simulations if it is not specified differently).

In Figure 3.19 the comparison between the calculated (Equation 3.37) and simulated resonance frequencies for different dimensions of the fabricated CCB resonators (see Chapter 4) vibrating in flexural-lateral mode is depicted. As it is shown, there is a good agreement between theoretical and simulated resonance frequencies, being the maximum absolute error Δf_0 = 0.5 MHz.
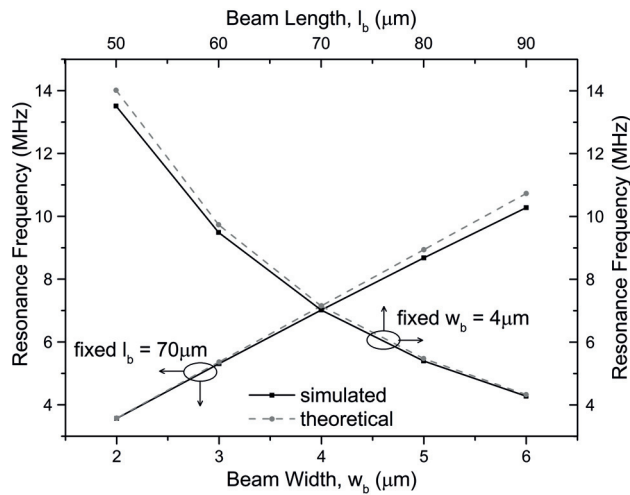
Figure 3.19 – Resonance frequency variabilities of CCB resonators depending on geometry.

Silicon is the structural material used in the devices present in this work. As it is an anisotropic material whose elastic properties depend on orientation relative to the crystal lattice [88], the values of Young's modulus E, Poisson's ratio ν and other elasticity quantities have to be appropriately chosen regarding on expecting modal shapes motion in relation with silicon crystal direction.

In order to prove how much expected resonance frequency can vary with respect to E and ν for the same geometry, FEM simulations have been performed for the CCB proposed above (see Figure 3.20). It is evident that variations of ΔE = 5 GPa can shift f_0 up to several tens of MHz, while the influence of $\Delta \nu$ = 0.05 is limited to tens of kHz.

3.4.2   Double-Ended Tuning Fork (DETF) Resonator

Modal electromechanical FEM simulations were carried out for a DETF resonator of l_b = 40 μm, w_b = 3 μm and t = 1 μm. The resonance modes that can be laterally excited are shown
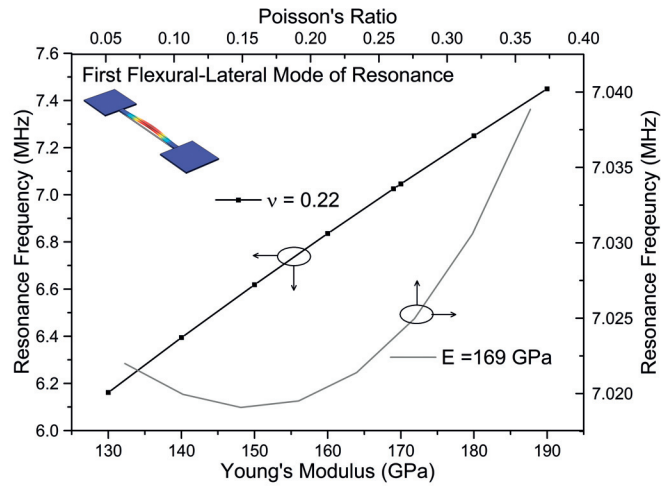
Figure 3.20 – Resonance frequency dependence with respect to Young's modulus and Poison ratio for a CCB of l_b = 70 μm, w_b = 4 μm and t = 1 μm.

in Figure 3.21 and they consist of in-phase (when the tines displace in the same horizontal direction) and out-phase (when the tines move in opposite in-plane directions).
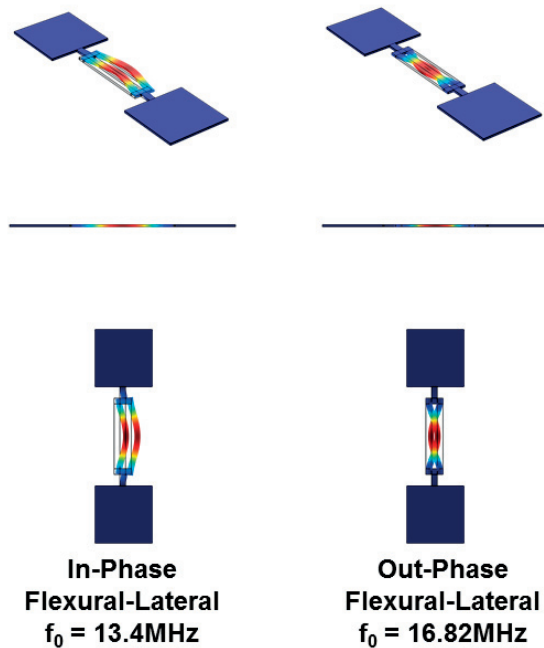
Figure 3.21 – First two flexural-lateral modes of the simulated DEFT (perspective, lateral and top views).

(a) f_0 versus w_b (fixed $l_b = 40 \ \mu m$).   (b) f_0 versus l_b (fixed $w_b = 3 \ \mu m$).
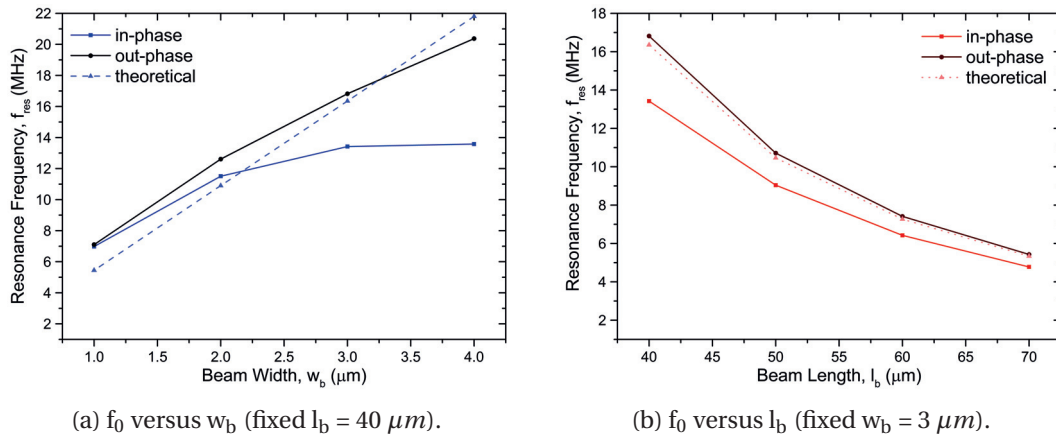
Figure 3.22 – Resonance frequency variabilities of DETF resonators depending on (a) beam width and (b) beam length.

In Figure 3.22 the comparison between the calculated (Equation 3.41) and simulated results for the DETF resonators of interest is included. In his case, a good accordance between analytical and simulated solutions have been found for out-phase mode of resonance (maximum absolute error $\Delta f_0 = 1.43$ MHz). As both in-phase and out-phase modes can be laterally excited in DETF resonators with the electrodes configurations presented in Section 3.3, these results will be useful during characterisation, in order to check which the preferential mode that is being excited in the coupled tines.

3.4.3 Parallel Beam Resonator (PBR)

The main modal shape for a PBR of N = 20, $l_b = 125 \ \mu$m, $w_b = 3 \ \mu$m, $l_m = 3 \ \mu$m and $w_m = 2 \ \mu$m is an extensional-lateral mode as depicted in Figure 3.23.

Extensional-Lateral
$f_0 = 30.39\text{MHz}$
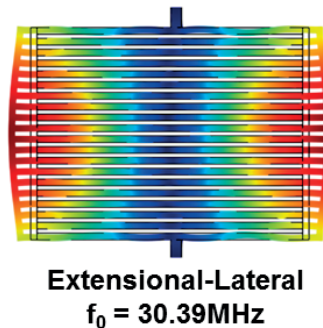
Figure 3.23 – Length-extensional mode of resonance of the simulated PBR.

Here the comparison between analytical and FEM models does not match as in the precedent sections. In Figure 3.24 a difference of several MHz in the extracted resonance frequencies is observed. This may be an effect of the approximations used to calculate the k_{eff} and m_{eff} or due to a non-accurate FEM simulation for this coupled-beams case.
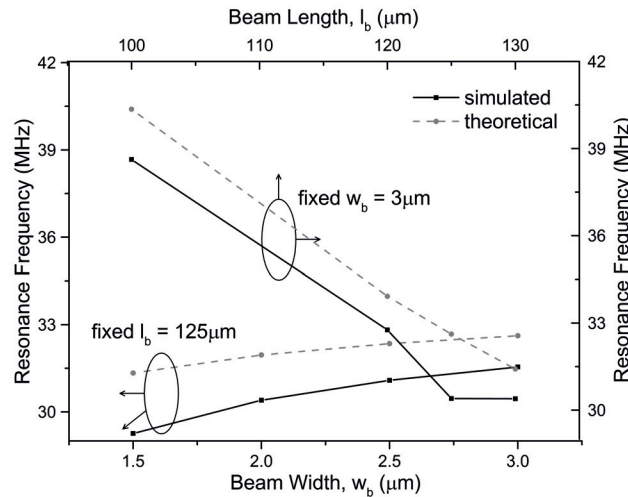
Figure 3.24 – Resonance frequency variabilities of PBRs.

3.4.4 Wine-Glass Disk (WGD) Resonator

One of the main existing issues in the theoretical and FEM approximations to the resonance frequency in the case of WGDs is the existing variability for full-disk and disks with realising holes. At a first glance, by including the realising holes in the design, the stiffness of the structure is reduced (the disk is less rigid), and so the resonance frequency is lower. In Figure 3.25 modal shapes and their extracted f_0 are shown for a disk of R = 30 μm, s = 3 μm, w_h = 1 μm and t = 1 μm.

The extracted maximum absolute error between the theoretical resonance frequency values (see Equation 3.46) and full-disk simulations is Δf_0 = 0.25 MHz. However, the difference betweeen the thoretical value for a full disk and the FEM simulated value for a disk with releasing holes is Δf_0 = 28.86 MHz. By taking into account Equation 3.48, it is evident that the effective mass is calculated by neglecting the holes, and thus, in this case FEM simulations should be taken into consideration in order to find the resonance frequency during the
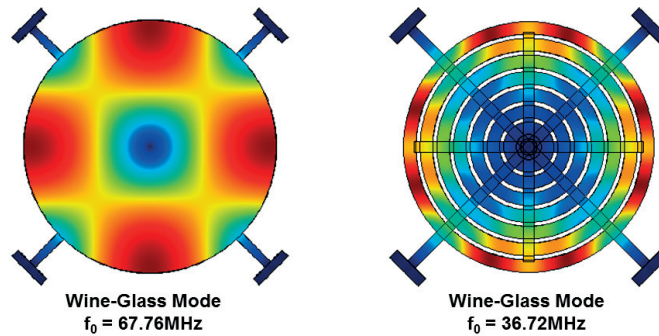
Figure 3.25 – Wine-glass modal shape of the simulated disk resonators: (left) full disk and (right) disk with releasing holes.

characterization of the devices.

Mechanical properties are strongly affected by the presence of etch holes because silicon becomes effectively orthotropic. Some approximations, as the effective medium approximation, were proposed to give good predictions of electromechanical behaviour [89] [90], otherwise FEM simulations are strongly recommended for etch-holes resonators prior design.
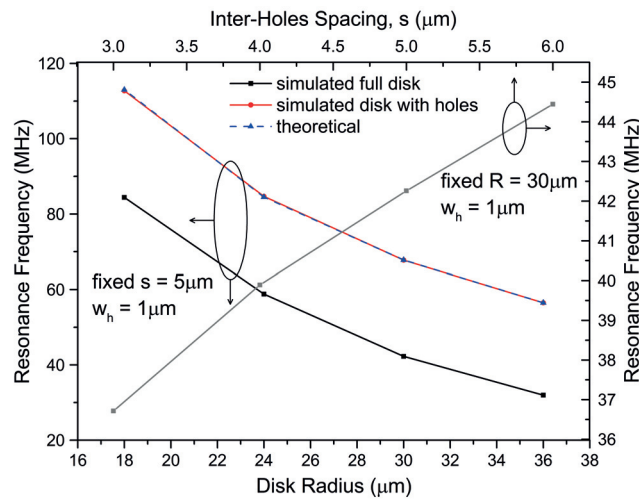
Figure 3.26 – Resonance frequency variabilities of WGD resonators.

In order to study the resonance frequency shifts regarding to variations in the geometry of the anchors of the WGD (see Section 3.2.6), FEM simulations have been carried out and the results have been plotted in Figure 3.27. While one of the dimensions has been varied, the remaining dimensions have been kept as indicated. In the case of thickness, variations between 0.25

and 2 μm suppose a slight growing deviation of the order of few hundreds of kHz. It can be concluded that certain flexibility in the design of this dimension can be accepted. Contrary, simulating the anchors width and length into the same geometrical range entails a deviation of several MHz of the original resonance frequency for both of the cases, rising and falling respectively, therefore, anchors dimensions are parameters to be strictly considered in the disk resonator design.
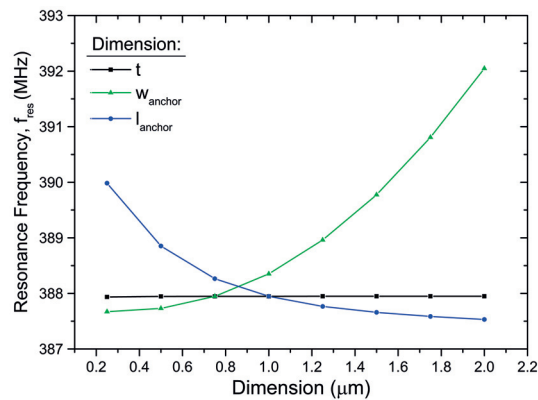
Figure 3.27 – Modal FEM simulations of the frequency shifts due to variations in the geometry of the disk: length and width of the anchors and thickness (fixed R = 5 μm). These simulations referred to the same WGD resonators presented in Section 3.2.5.

3.4.5 Square Plate Resonator (SPR)

Similar effect due to the releasing holes is observed for the two square plate resonators vibrating in their Lamé mode of resonance included in Figure 3.28 (l_p = 30 μm, s = 4 μm, w_h = 1 μm and t = 1 μm), nevertheless the frequency shift is smaller due to a minor impoverishment of the mechanical stiffness of the device.

Accordingly, in this case the theoretical calculations match better with FEM extracted resonance frequencies than in the case of bulk WGD resonators, simply because of the fact that in this case the considered releasing holes are smaller in comparison with the plate. A maximum absolute error Δf_0 = 4.66 MHz has been found between theoretical and full-plate simulations extracted values, and a slightly greater value of Δf_0 = 6.6 MHz by comparing analytical with holes-plates simulations results. As it is detailed in Chapter 4, the characterized SPR did not vibrate in their Lamé mode of resonance but in a spurious mode of resonance (most likely square extensional). Therefore the comparison presented above remains as a cross check
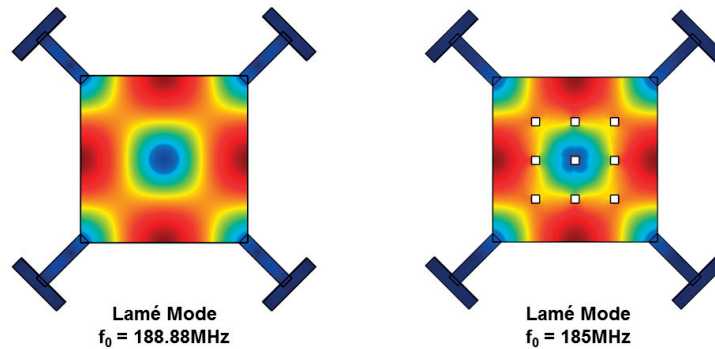
Figure 3.28 – Lamé modal shape of the simulated square plate resonators: (left) full plate and (right) plate with releasing holes.

between theoretical and FEM results.
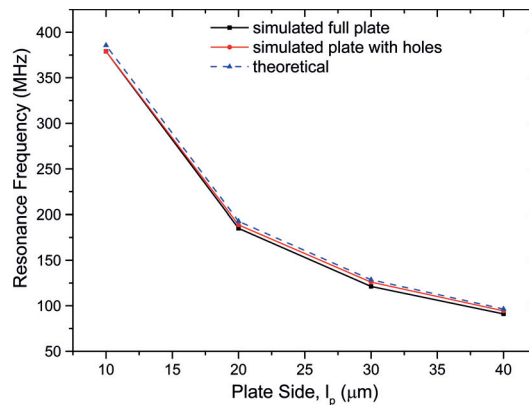
Figure 3.29 – Resonance frequency variabilities of a square plate resonator.

3.5 Summary

In this chapter, we have reviewed the equivalent models of capacitively actuated MEMS resonators and the main expressions for this analytical characterization have been extracted for both capacitive and piezoresistive detection methods. In the same way, the gap-filling effect has been theoretically analysed in terms of the resulting transduction efficiency, concluding that partial and full gap-filling achieve better coupling transduction factors than their counter in air.

The resulting range of motional resistance have been calculated and compared for different partial and fully filled gaps. In this preliminary study, we have arrived to the conclusion that

motional resistance can be reduced in a factor of 600 times by using a high-k material into the gaps as long as the quality factor is not too impoverished due to the added material. In order to provide methods that effectively help to boost the quality factor performance of capacitive MEMS resonators with partial or full filled-gaps, nonlinear dynamics has been extensively treated, concluding that the damping effect more straightforwardly controlled is the anchors damping.

An alternative method to calculate the quality factor based on the slope of the phase has been experimentally validated by comparing it with the one extracted from the resonance peak bandwidth and proven to achieve an agreement up to 7 %.

The most original contributions to this chapter are the theoretical and FEM analysis comparisons and validations that have been carried out for all flexural (CCB and DETF) and bulk (PBR, WGD and SPR) resonators that have been fabricated and characterized in Chapter 4. Resonance frequency approximations variabilities coming from geometrical device and anchors dimensions, changes in the elastic properties of the structural material, realising holes influence and anchors clamping have been discussed.

4 Design, Fabrication and Characterization

This chapter presents the design, fabrication and electrical characterisation of five types of capacitive microelectromechanical (MEMS) resonators: clamped-clamped beams, double-ended tuning forks, parallel-beams, disks and square plates resonators.

The resonators have been designed and actuated to vibrate at their fundamental in-plane flexural (CCB and DETF) and bulk (PBR, WGD and SPR) modes of resonance in a range of frequency between 5 MHz and 70 MHz.

Two-port measurements in vacuum and at room temperature have been carried out in order to perform capacitive actuation by means of air and partially-filled (HfO_2) transduction gaps and capacitive and piezoresistive detection. The contrasted results for the different transduction gaps and actuation-detection measurement techniques are presented. The effects coming from a multiple number of DC probes (up to four probes) and a different number of anchors (two and four) are analysed for a WGD resonator with partially-filled gaps. Quality factors in the order of several thousands (12163 for WGD and 8433 for DEFT resonators) have been achieved, accomplishing motional resistance as low as 874 Ω for WGD resonators.

The nonlinearities regarding the air-damping and RF handling presented in Chapter 3 are discussed for experimental data.

4.1 Introduction

In this chapter, the fabrication processes of clamped-clamped beam (CCB), double-ended tuning fork (DETF), parallel beam (PB), wine-glass disk (WGD) and square plate (SP) capacitive MEMS resonators studied in Chapter 3 are detailed for both air and HfO_2 partially-filled transduction gaps. The electrical characterization methods that have been used are described and the experimental measurements for the fabrication air and partially-filled gap resonators are presented and compared.

4.2 MEMS Resonators Design

A large variety of MEMS resonators designs have been designed in order to cover a large range of resonance frequencies and obtain working devices in diverse flexural and bulk modes of resonance. As it is studied in Chapter 3, analytical and FEM models describe all the resonators geometries that have been chosen for the present work (see Table 4.1): clamped-clamped beams (CCB), double-ended tuning forks (DETF), parallel-beam resonators (PBR), wine-glass disks (WGD) and a square plates resonators (SPR).

The modal shapes have been obtained by means of Finite-Elements Methods (FEM) simulations (as detailed in Chapter 3). In the case of the square plate, the measured resonance peak have been found in lower frequencies than the expected for the Lamé mode, therefore other modes spurious mode of resonance (most likely square extensional) are being excited.

The resulting comparison for theoretical, simulated and experimental resonance frequencies for each fabricated device are included in Table 4.2. A good agreement between theory, simulations and experimental measurements is achieved (error 3-18 %) for CCB, DETF, PBR and WGD resonators (simulated with releasing holes, see Section 3.4.4).

Table 4.1 – Geometries, modal shapes and dimensions of the resonators in this work. For each device several air and partilly-filled gaps are considered.
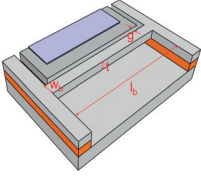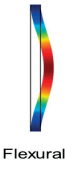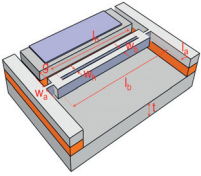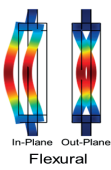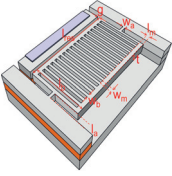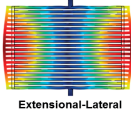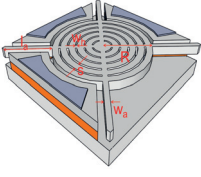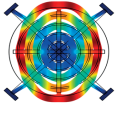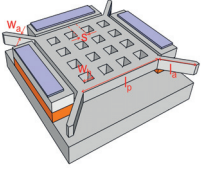
Device	Mode	Dimensions	(μm)			
	Flexural	**CCB** $l_b = 70$ $w_b = 4$				
	In-Plane Out-Plane Flexural	**DETF** $l_b = 40$ $w_b = 3$ $l_h = 34$ $w_h = 3$ $l_a = 6$ $w_a = 3$				
	Extensional-Lateral $f_0 = 30.39$MHz	**PBR1** $l_b = 125$ $w_b = 3$ $l_m = 3$ $w_m = 2$ $l_a = 10$ $w_a = 5$ $N = 20$	**PBR2** $l_b = 151$ $w_b = 5$ $l_m = 5$ $w_m = 5$ $l_a = 20$ $w_a = 6$ $N = 12$	**PBR3** $l_b = 151$ $w_b = 5$ $l_m = 5$ $w_m = 5$ $l_a = 20$ $w_a = 6$ $N = 20$	**PBR4** $l_b = 50$ $w_b = 2$ $l_m = 2$ $w_m = 2$ $l_a = 7$ $w_a = 3$ $N = 13$	**PBR5** $l_b = 100$ $w_b = 3$ $l_m = 3$ $w_m = 2$ $l_a = 10$ $w_a = 5$ $N = 20$
	Wine-Glass	**WGD** $R = 30$ $s = 5$ $w_h = 1$ $l_a = 9.8$ $w_a = 2.5$				
		SPR1 $l_p = 20$ $w_h = 1$ $s = 3.75$ $l_a = 6.6$ $w_a = 1.6$	**SPR2** $l_p = 30$ $w_h = 3$ $s = 7.5$ $l_a = 15$ $w_a = 3$			

Table 4.2 – Comparison between the analytical, simulated and measured resonance frequency.

Device	Analytical f_0 (MHz)	Simulated f_0 (MHz)	Measured f_0 air-gap (MHz)
CCB	7.151	7.020	5.720 (30V)
DETF in-phase out-phase	16.351	13.421 16.817	10.949 (20V)
PBR1	32.619	31.544	29.738 (70V)
PBR2	25.170	25.169	23.591 (80V)
PBR3	24.905	24.904	22.190 (80V)
PBR4	70.548	71.813	69.053 (50V)
PBR5	39.451	38.201	36.468 (80V)
WGD	67.801	42.258	41.1256 (80V)
SPR1	-	-	14.732 (60V)
SPR2	-	-	9.951 (60V)

4.3 MEMS Fabrication Technology

All the resonators that are presented in this work have been fabricated by following some common first steps that are presented in Section 4.3.1. This fabrication process has been modified for the last steps in order to carry out partially-filled gaps resonators based on HfO_2 (see Section 4.3.2).

4.3.1 Air-Gap Resonators

Doped p-type thin SOI wafers with device layer of 1 μm and buried oxide (BOX) layer of 1 μm were used for the fabrication as it is depicted in Figure 4.1. A full wafer n^+ diffusion with phosphorous ($POCl_3$) was carried out in furnace between 950°C and 110°C with the goal of creating a substrate with doping concentration $10^{20} cm^{-3}$. In order to uniformly distribute the dopants in the wafer, an annealing was performed (T>1000°C).

Alignment marks of 5 μm depth were created in order to ensure a successful alignment after each needed mask alignment. Therefore, a first photolithography mask was used to etch alignment marks till arrive to the bulk silicon underneath (5 μm depth and 20 μm side) as it is shown in Figure 4.1.b.

E-beam lithography was carried out by patterning the E-beam resist ZEP as it is sketched in

a. Doping/Deglazing/Extra Diffusion

1 µm Si Thin Film

1 µm BOX

Bulk Si

b. Alignment Marks

5µm

20µm

c. E-beam Patterning and Si Dry Etch

ZEP Resist

d. Thermal Oxidation

e. Pt Lift-Off

f. Release Vapor HF

Figure 4.1 – Schematic of the fabrication process used to create air-gap MEMS resonators.

Figure 4.1.c. A Bosch-like Deep Reactive-Ion Etching (DRIE) process was performed with the aim to transfer the pattern into the silicon device layer to create the gaps existing between the resonator body and the electrodes in a range of 100 to 500 nm width and 1 μm depth (high aspect ratio structures, HARS). As the Bosh-like DRIE utilizes an etching cycle flowing only SF_6 and then switches to a sidewall passivating cycle using only C_4F_8 and another cycle of O_2 to clean the passivants [91], this alternating of etching and passivating cycles forms scallops on the sidewalls of the etched features whose roughness depends on the pulses used. Thanks to the short pulses recipe it was possible to reduce the roughness scalloping of the vertical surface as it is shown for a silicon dummy wafer in Figure 4.2. Therefore, a thermal oxide layer of 15 nm was grown and subsequently etched to reduce the remaining vertical surface roughness. At the same step, etch holes were conducted in the body of the resonators to ease the later oxide etching during the final step to release the structures.

In correspondance of a transition between small and large features, bridges in the gap (skirts) can happen because of the over-passivation coming from the larger features. This effect is named skirting effect [92], and it was avoided by correcting the mask in order to create a
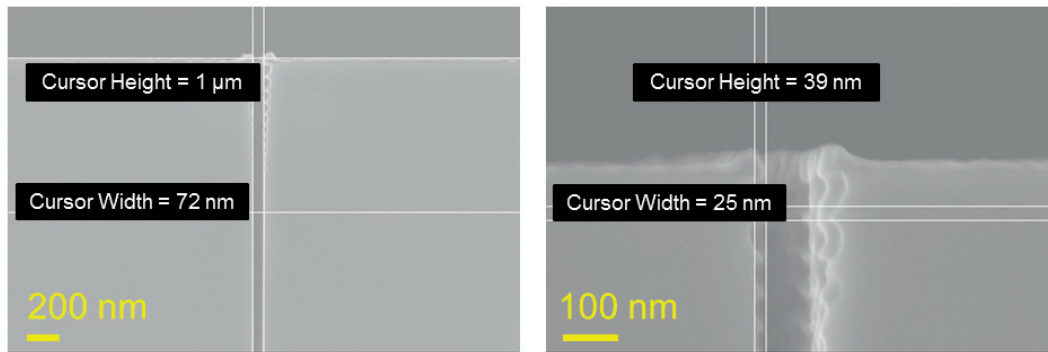
Figure 4.2 – Bosch-like DRIE etching optimisation.

smooth transition between the trenches and the open areas as it is shown in Figure 4.3.
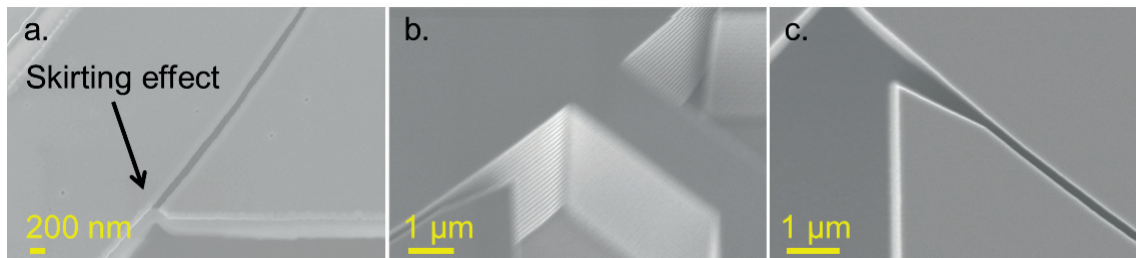
Figure 4.3 – (a) Skirting effect and mask corrections (b) lateral and (c) frontal views.

Coming up next, a lift-off step of 150 nm of platinum is performed in order to build the metallic electrodes of the resonators as it is sketched in In Figure 4.1.e. Following, the final critical step to release the resonators bodies was accomplished by means of a vapor HF process where the wafer holder was kept to 37°C. This method is an isotropic etch removal that performs the etching of sacrificial layer without yielding stiction. It provides user-controlled, residue-free etching across a wide range of etch rates that varies for each oxide.
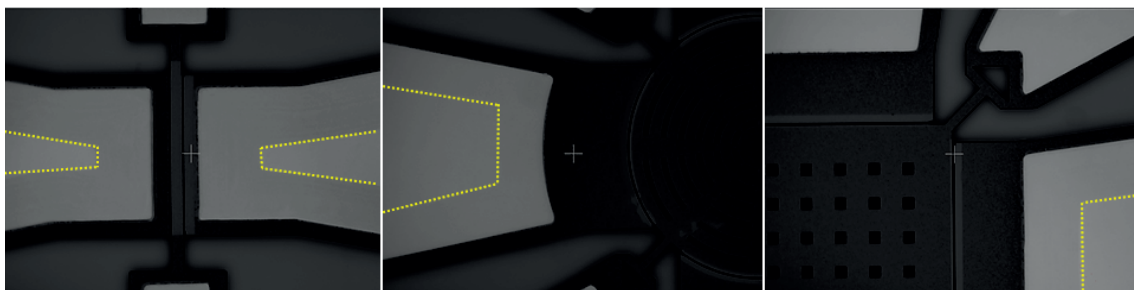
Figure 4.4 – Underetch of the underneath oxide for (a) a clamped-clamped beam (b) a disk and (c) a plate. Dashed yellow lines point the interface with the remaining oxide.

In order to carry out the release of the devices from the silicon oxide sacrificial layer, releasing holes operated in the resonators bodies were designed in order to avoid an underetch larger than 7 μm in the electrodes sides while releasing the devices from the SiO_2 sacrificial layer. As over-releasing the structure would induce stress in the resonators, the oxide etching rate was precisely controlled by visually checking the contrast of the oxide under the structure with the microscope as it is shown in Figure 4.4.

A finalised air-gap disk resonator of 40 μm radius and 100 nm gap after release is shown in Figure 4.5. A Focussed Ion Beam (FIB) cut was realized along the gap in order to check its final dimension and smoothness. If the deposition of the Platinum mask and the redeposition of material (silicon and platinum) during the physical sputtering process (materials visible inside of the gap and below the structure with the same light gray color) are neglected, the fabricated gap is around 120 nm.
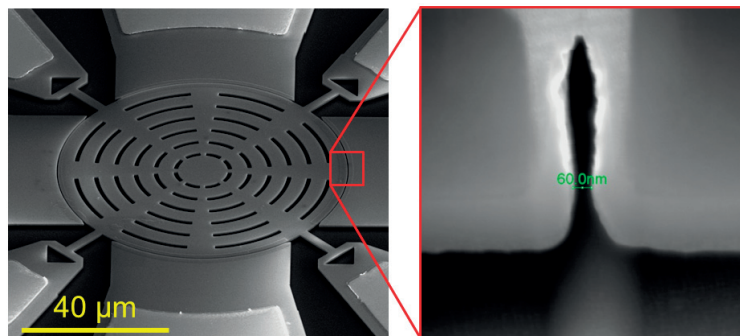
Figure 4.5 – (Left) Finalised released MEMS disk resonator (radius 40 μm and gap 100 nm) and (right) FIB cut of the air-gap. On light gray the redeposited material after the process can be seen.

Non-contact optical surface profilometer inspections were performed in released devices, firstly to observe the flatten of the suspended resonant body and secondly to inspect the vertical alignment of the electrode with the body of the resonator. Both factors are extremely important in order to maximize the coupling factor (detailed in Equation 3.14), which proportionally depends on the overlapping area between the electrodes and the body of the resonator. The used optical profiler had vertical resolution of 3 nm in vertical scanning interferometry mode and of 3 Å in phase shifting interferometry for single measurements.

From the capture shown in Figure 4.6, Figure 4.7 and Figure 4.8, several conclusions have been
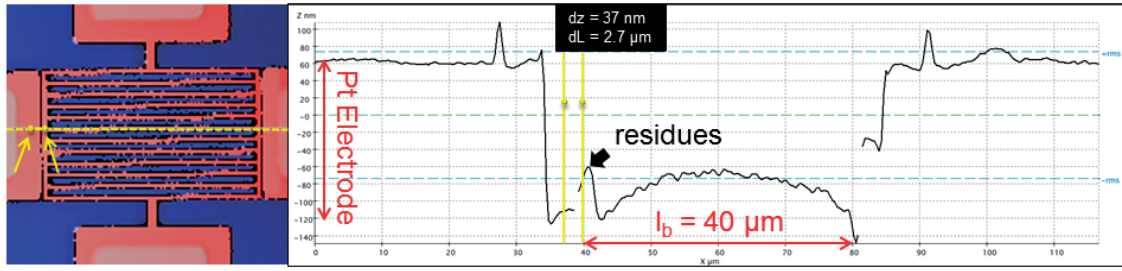
Figure 4.6 – Profiling of a PBR composed by beams of length l_b = 40 μm and gap 100 nm.
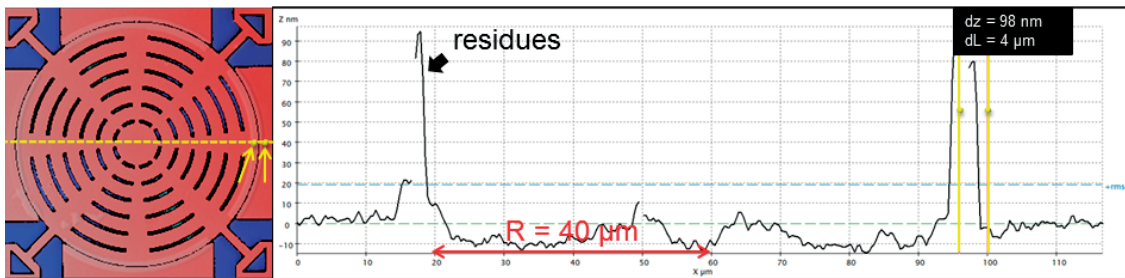
Figure 4.7 – Profiling of a disk resonator of radius R = 40 μm and gap 100 nm.
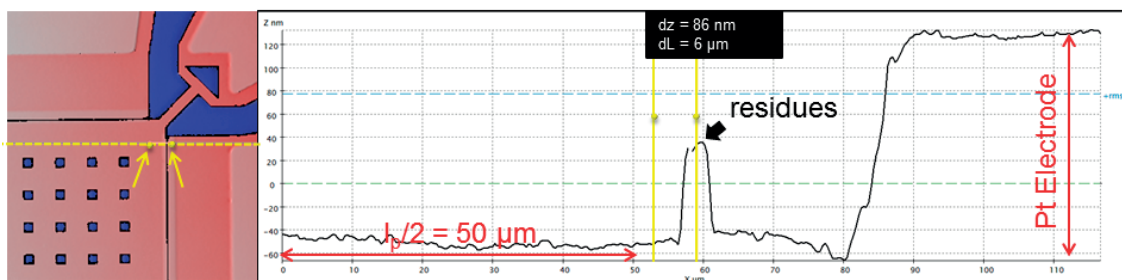
Figure 4.8 – Profiling of a square plate resonator of side l_p= 100 μm and gap 100 nm.

extracted: (1) the resonators bodies have an averaged misalignement with regard to the silicon electrodes of around ±10 nm; (2) the platinum layer deposited on top of the silicon electrodes to conform the metallic pads was measured of the order of 170-180 nm, so about 20% thicker than expected, which was an effect coming from the fact that a Pt sputtering was carried for the lift-off step of this chip, (10-20% of nonconformity) and (3) the compared height between two points immediately before and after the gap (in yellow) has an averaged difference of 77 nm, mostly due to the presence of some metallic residues present close to the gaps.

As these measurements were carried out in a test device that had been already pre-processed to have PVDF-TrFE solid-gaps (see Appendix B), these residues are fruit of the removal of the metallic hard masks that were going to be used during the etching step of the coated PVDF-TrFE [93].

Notwithstanding the presence of the residues close to the gap, the resonators bodies are in the same horizontal plane than the silicon electrodes with a misalignment around ±10 nm. Taking into consideration that the thickness of the resonator is 1 μm, if this misalignment was constant along the electrode edge, the overlapped actuation electrode-resonator area would decrease in a 1-2%, and proportionally the coupling factor (see Equation 3.14).

4.3.2   Hafnium Oxide Partially-Filled Gaps Resonators

According with the discussion included in Section 3.2.5, one alternative approach to achieve smaller transduction gaps consists of partially fill them with a high-k dielectric material. In order to conformally depose the dielectric in the gap, Atomic Layer Deposition (ALD) is recognised as the only method suited for this uniform gap-coating process. Hafnium oxide (HfO$_2$) was chosen as dielectric due to its high dielectric constant ($\epsilon_r \sim 19$) and its availability in the ALD facilities. The ALD of HfO$_2$ was done in a chamber kept at 200°C by adding deposition cycles of TEMAH (first precursor) at 80°C and HfO$_2$ at room temperature (RT).

Taking into consideration the fabrication steps presented in Figure 4.1, an ulterior step of ALD is incorporated to the process flow as it is sketched in Figure 4.9 to uniformly cover all the surfaces with a HfO$_2$ layer.

g. HfO₂ ALD

Figure 4.9 – Schematic of the added fabrication step used to partially filled the resonator gaps with HfO_2.

4.4 Measurement Setups

The electrical characterization of the MEMS resonators (on-chip and on-wafer) in the frequency domain is performed in a Süss Microtech cryogenic prober chamber model PMC 150. In this chamber the devices are kept at high vacuum (levels better than 10^{-5} mbar) and it allows to perform measurements in a range of temperatures from 4 to 400 K. The temperature control unit uses either liquid nitrogen or helium for the cooling. The pressure level depends on two pressure gauges installed into the system.

The electrical characterization setup in two-port configuration for capacitive (or electrostatic) MEMS resonators actuation is sketched in Figure 4.10 for a DETF as example. The scattering transmission parameters, S-parameters, of a device are measured by means of a vector network analyser (VNA) Anritsu MS4647B that is able to provide an RF power in a range from 10 dBm to -30 dBm. The DC bias are applied using a parameter analyser Agilent 4156 that is remotely controlled jointly with the VNA. It has an expansion module that can provide constant DC voltages in a range of ±200 V. Coaxial, triaxial or RF cables are connected to the measurements tools for static or RF measurements. Bias-tee (bias-T) connectors that withstand a DC voltage up to 200 V are used as interface between the RF and the DC actuation voltages in order to isolate the VNA and avoid electrostatic discharge coming from the the DC signals of parameter analyser. RF probes (in a Ground-Signal-Ground, GSG, standard configuration) with a 150 nm pitch and DC probes are are manually placed on the pads of the devices with a visual control provided through a microscope.

81
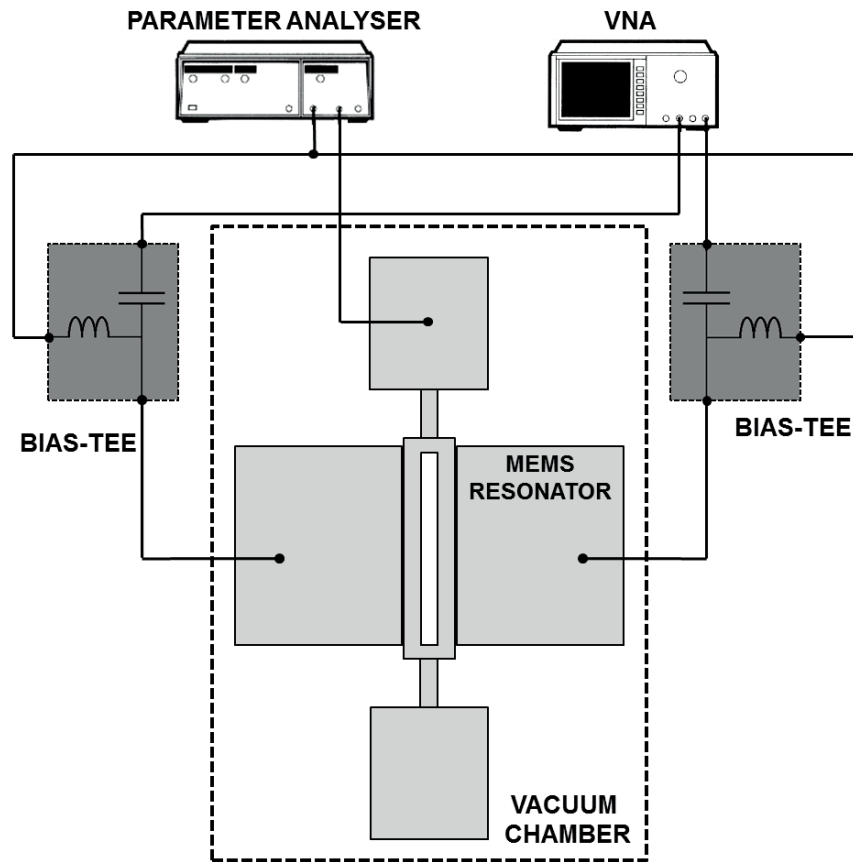
Figure 4.10 – Capacitive/Electrostatic characterization setup for a DETF in a two-port configuration.

4.4.1 Capacitive Detection

Figure 4.11 shows general 2-port probes schematics of two capacitive MEMS resonators: (left) a DETF with 2-probes to apply the AC + DC excitation and (right) a disk resonator with 2-probes to apply the AC excitation and 4-probes to apply the DC excitation. The diagram includes the resonators in the center and the capacitive drive and sense electrodes. For the 2-port excitation the AC and DC signals are directly mixed by means of the tee-bias and applied to the two-port drive ($v_{ac} + V_{DC1}$) and sense ($v_{ac} + V_{DC2}$) electrodes.

In the case of the 2-probes + 4-probes excitation, two extra DC signals, V_{DC3} and V_{DC4}, are supplied in order to study the stiffness softening of the structure. The body of the resonator and the SOI substrate are grounded to avoid undesired vertical pull-in of the resonator, which would make the resonator collapse (see Section 3.2.6).
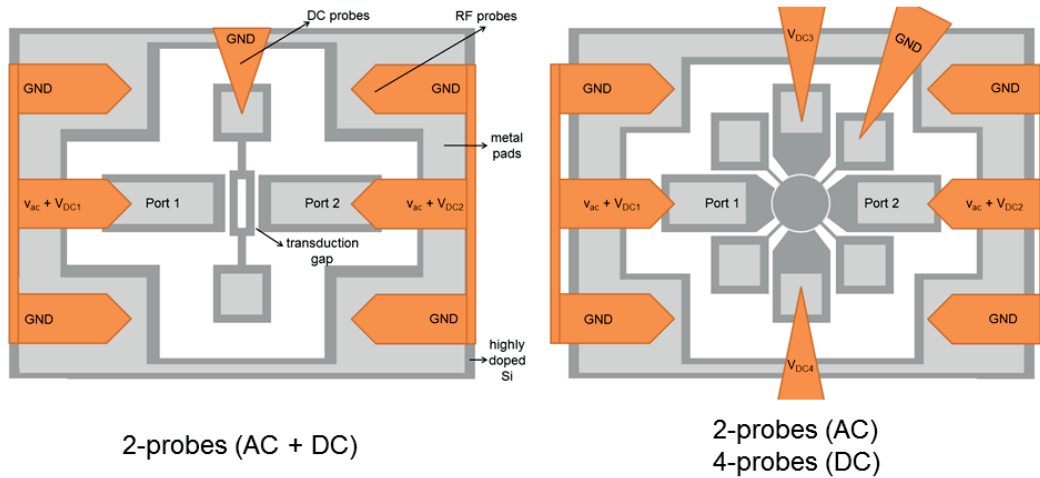
Figure 4.11 – Two-port capacitive measurement setup used for the characterization of capacitive resonators with (left) 2-probes to apply the AC + DC excitation and (right) a disk resonator with 2-probes to apply the AC excitation and 4-probes to apply the DC excitation.

4.4.2 Piezoresistive Detection

Most often MEMS resonators use capacitive transduction to excite and detect the mechanical resonance because it is easily implemented on-chip. However, typically these resonators may exhibit high impedance at resonance. In order to minimize the effect of high motional resistance, piezoresistive detection is used to amplify the ouput current coming from the mechanical motion of MEMS resonators [24] [10] [11].

Here, the detected output current is proportional to the current through the resonator (due to the piezoresistive effect of single crystal silicon) in combination with the capacitive current over the transduction gap (see Section 3.2.4) [40]. As it is depicted in Figure 4.10, the resonator is capacitively actuated by applying AC + DC signals in the excitation gates ($v_{ac} + V_{DC1}$). A DC voltage difference (between V_{DC2} and ground) is applied into two transversal resonator anchors to stretch the resonator causing a change in the mechanical strain leading to a change of resistance that has a proportional effect in the output current (piezoresistive effect). Alternatively this detection mode might be combined with two extra DC probes as shown in Figure 4.12 that are independently controlled by V_{DC3} and V_{DC4} and that can be optimize in order to maximize the piezoresistive detection (see Section 3.2.4).
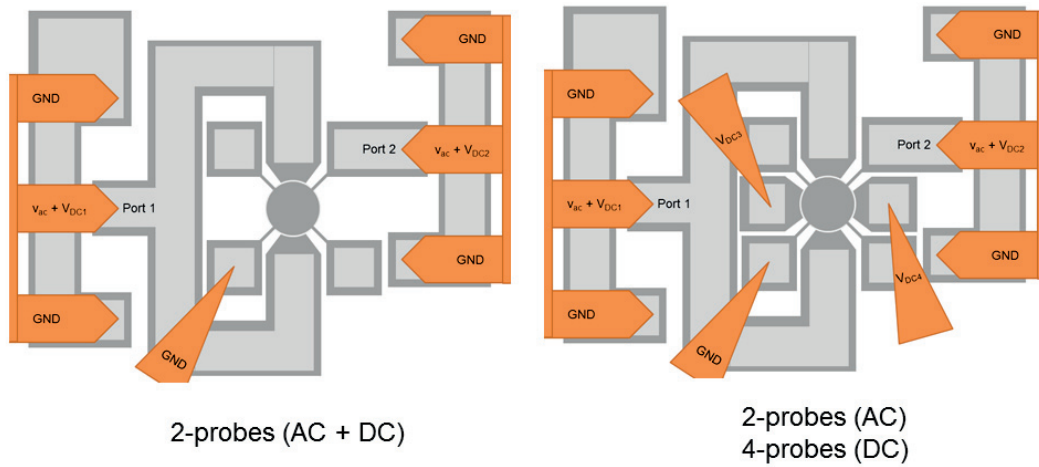
Figure 4.12 – Two-port piezoresistive measurement setup used for the characterization of capacitive resonators with (left) 2-probes to apply the AC + DC excitation and (right) a disk resonator with 2-probes to apply the AC excitation and 4-probes to apply the DC excitation.

4.4.3 Optical Detection

Commercial Laser Doppler Vibroter LDV systems consist of two major components: the optical sensor/controller processor and the scan control/data acquisition system. The optical sensor contains the actual laser, the optical elements, and electrical components needed to spatially position the laser beam. The controller processor, containing the electronic components needed to process the velocity information provided by the optical sensor, constitutes the interface between the interferometer and the scan control/data acquisition computer. The continuous nature of the Doppler signal focused on the resonator body surface that vibrates out-of-plane at the resonance frequency (Poisson's effect) allows to the in-plane resonance frequency tracking demodulation [94].

In this configuration, resonators are capacitively excited as in the capacitive detection method presented above, but the changes in the resonance frequency are tracked by a laser diode focused on the resonator whose reflected signal is tracked by a sensitive photodetector (SPD) [95] as it is depicted in Figure 4.13. In this case, the AC signal is provided by means of a UHF Lock-In (LI) Amplifier Zurich Instruments. The DC voltages are given by a DC Power Supply Hewllet Packard E3631A.
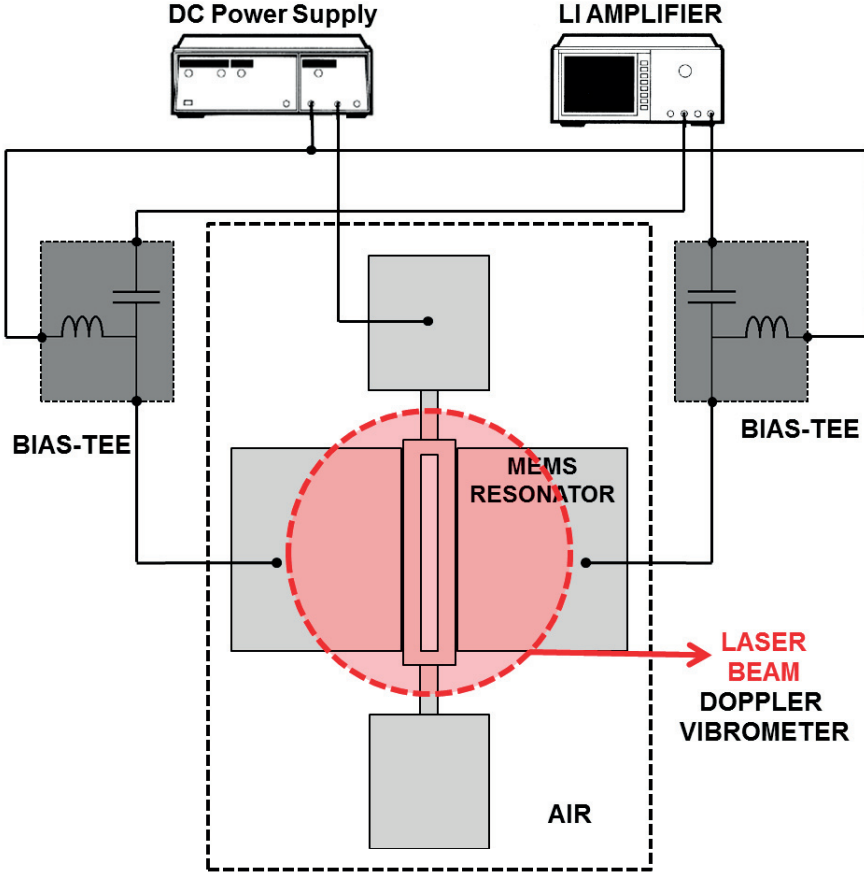
Figure 4.13 – Optical characterization setup for a two-port configuration.
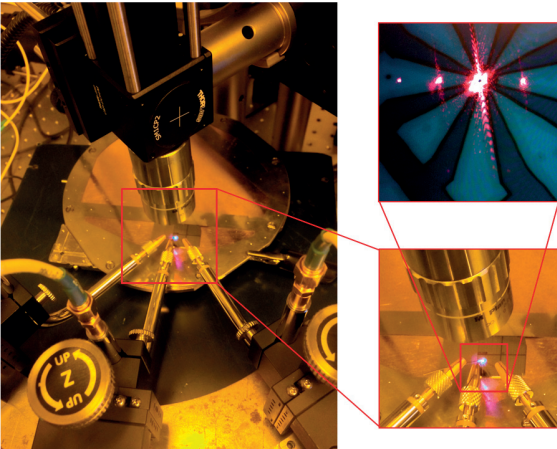
Figure 4.14 – Two-port measurement optical set-up.

The resonator response is measured in air by placing it under the beam of a laser Doppler vibrometer Polytec OFV-55 ruled by a Polytec OFV-5000 vibrometer controller. When the resonator is capacitively actuated, the vibrations at the resonance frequency are extracted from the Doppler shift in frequency of the reflected laser beam (resolution 50 nm/V) in the SPD. Figure 4.14 shows the ad hoc setup in air (left and right-bottom) with the resonator being actuated and the laser beam focussed on the resonator surface (right-top).

Laser Doppler vibrometry (LDV) systems are suitable to resolve the details of a MEMS structure that is vibrating in an in-plane mode of resonance (in horizontal) by detecting its consequent out-of-plane vibrations (in vertical).

4.5   Air-Gap Capacitive MEMS Resonators

In this section, an comparison among the detection methods proposed in Section 4.4 is presented followed by a thoroughgoing study of the flexural and bulk MEMS resonators described previously.

All the air-gap resonators presented in the present section have only a native oxide layer of around 10-20 Å formed due to its exposure to ambient conditions. Capacitive and piezoresistive measurements have been carried out in vacuum and room temperature (RT) and the measurement bandwidth has been fixed to 10 Hz with no averaging in the utilized VNA. Devices and chuck have been kept grounded to avoid structures vertical collapse (see Section 3.2.6).

In this section and Section 4.6, quality factors have been calculated by means of the BW consideration in the cases where signal magnitudes were higher than 3 dB, otherwise the phase-slope method detailed in Appendix A has been applied. Similarly, in order to improve the accuracy of the analysis and avoid as much as possible uncertainness coming from the noise, experimentally acquired signals have been processed (Loess signal smoothing and Lorentz fitting, when needed). The used signal treatment for a parallel beam resonator a PBR2 (see Table 4.1) with air-gap g = 100nm capacitively sensed at DC bias $V_{DC1} = V_{DC2} = 100$V and RF power -20 dBm is shown in Figure 4.15.
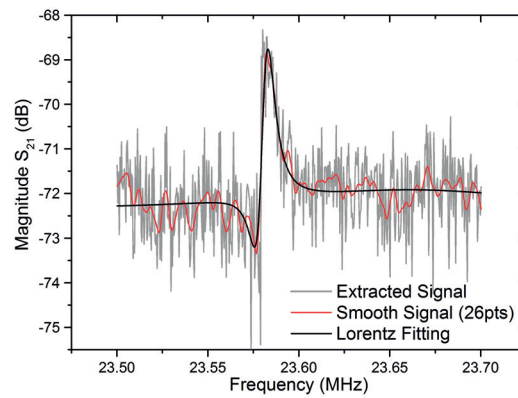
(a) Magnitude of the measured transmission parameter.
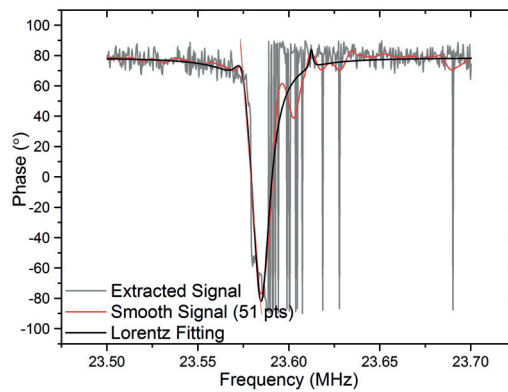
(b) Phase of the measured transmission parameter (gray).

Figure 4.15 – Signal treatment example for PBR2 (g = 100nm).

4.5.1 Comparison of the Detection Techniques

Optical and Capacitive Detections

Figure 4.16 shows the SEM picture of a silicon DETF resonator fabricated as described in Section 4.3.1. The forks were operated in lateral flexural mode profiting from the in-phase (beams resonating jointly in the same planar direction) and out-phase (beams moving in opposite planar directions) modes of resonance. The structure has the dimensions specified in Table 4.1 and an air-gap g = 500 nm as it is illustrated in Figure 4.16 (right).

Certain dependance between the signal floor-level and the applied DC bias can be observed in
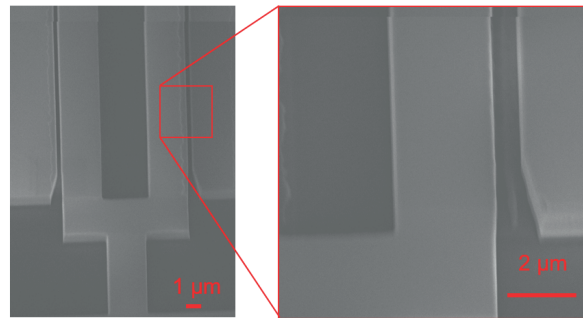
Figure 4.16 – SEM images of the released DETF1 (see Table 4.1).

Figure 4.17. De-embedding techniques have been proposed in literature in order to minimise the effect of feedthrough (see Section 3.2.1), which could be the cause of this effect and should be considered for future designs.
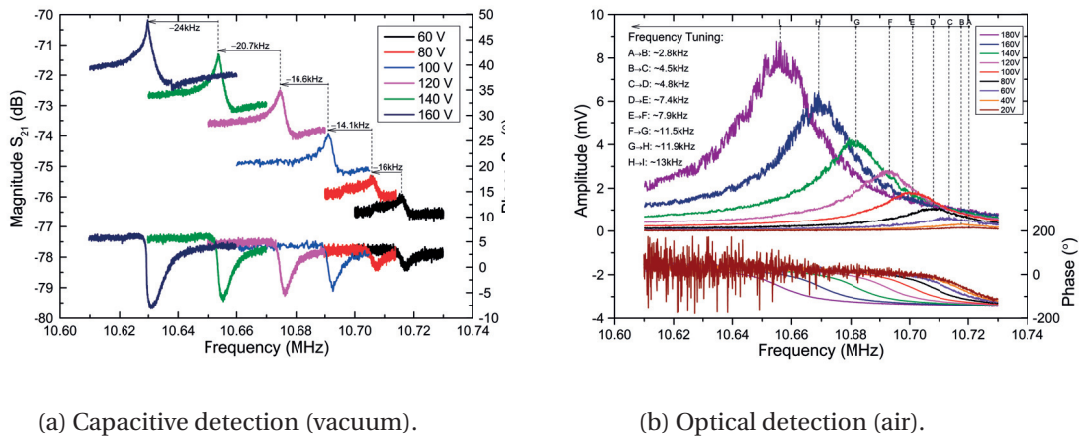
(a) Capacitive detection (vacuum). (b) Optical detection (air).

Figure 4.17 – Transmission characteristics of the fabricated DETF (l_b = 40 μm, w_b = 3 μm, g = 500nm).

The same device was measured in the optical and capacitive detection setups presented in Section 4.4. The experimental transmission characteristics of the DETF varying with the bias voltage are included in Figure 4.17. The applied RF power was of 0 dBm in both setups. As it was expected, the resonator stiffness softens as the bias potential is increased.

The capacitive coupling factor of a MEMS resonator increases with bias potential by means of the relation shown in Equation 3.14. As the capacitive coupling factor is proportional to the output current, a higher coupling factor implies a higher capacitive current, therefore the detected signal is enhanced and better Q-factor could be obtained as a result of the

improvement in the readout.

The characteristic measured and calculated parameters of the DEFT are listed in Table 4.3. As the working DETF was fabricated with air-gaps of 500 nm, which are relatively wide, large motional resistance were expected [52].

Table 4.3 – Characteristic parameters of the DEFT extracted from capacitive and optical detection. Motional parameters (R_m, C_m and L_m) are calculated from Equation 3.15.

Parameter	Capacitive Detection	Optical Detection
V_{DC1}, V_{DC2}, (V)	100	100
f_0, (MHz)	10.6911	10.7009
Q	468	400
R_m, (Ω)	1.1M	-
C_m, (F)	28.74a	-
L_m, (H)	7.7	-
$\eta_e^2(\frac{C^2}{m^2})$	14.5f	-

The downshifting in resonance frequency with regards to an increasing DC excitation of the DETF evidences the reduction in the fork effective stiffness due to the spring softening of the beams (see Section 3.2.6). In Figure 4.18 (gray line), differences in the resonance frequency downshifting were observed between the acquired capacitive and optical output signals. Similarly, the downshifting in the resonance frequency was observed decrease more quickly for the capacitively (black line) than for the optically detected signals (red line). These variations are effect of the different sensitivity and uncertainness coming from the provided DC signals in each setup.

Piezoresistive and Capacitive Detections

A disk resonator (see Table 4.1) vibrating in its wine-glass mode, in which the motions of opposite sides are in phase while being 180° out of phase with respect to the other two sides was measured as described in Section 4.4 at a RF power of -20 dBm. The experimental transmission S-parameters of the WGD are shown in Figure 4.19.

As it is depicted, the piezoresistive readout substantially rejects the effect of capacitive feedthrough parasitics present during the measurements. Nevertheless, the noise floor under the same driving conditions looks slightly better in case of the capacitive detection, possibly
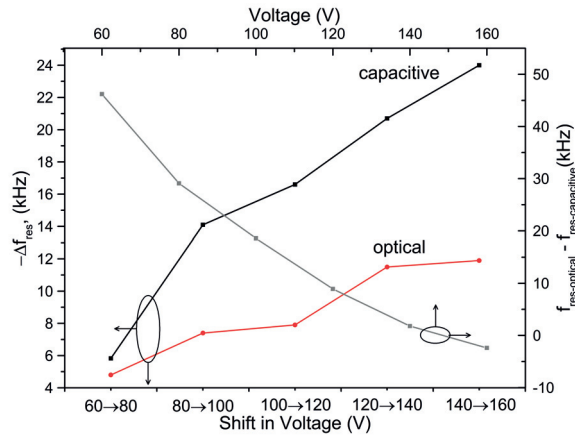
Figure 4.18 – Resonance frequency difference between capacitive and optical detection (gray line) and resonance frequency shifts with voltage for both detection methods (black and red lines).

due to a shorter path in the electrode layout. This result validates the acquired resonance frequency with two detection methods based in different physical principles.
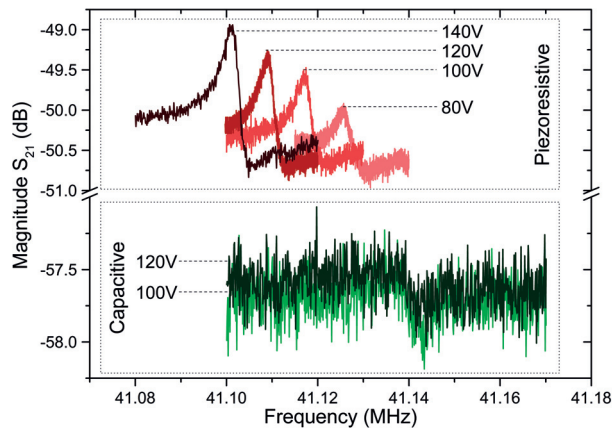
Figure 4.19 – Transmission parameter S_{21} response for the capacitive and piezoresistive detection methods for a 100 nm air-gap WGD resonator.

The detection of the motional signal is enhanced enabling Signal-to-Noise (SNR) ratios up to 5.6 times better at the same nominal voltages. Quality factors have been extracted by means of the phase-slope approximation and are 228 (capacitive detection, $V_{DC1} = V_{DC2} = 100V$) and 1107 (piezoresistive detection, $V_{DC1} = 100V$, $V_{DC2} = 1V$). The piezoresistive transduction also provides superior resonator performance in terms of motional resistance [11] [24] [96].

The motional resistance calculated (Equation 3.15) for 100 V are 74.8 kΩ for the capacitive

Table 4.4 – Characteristic parameters of the described WGD extracted from capacitive and piezoresistive detection. Motional parameters (R_m, C_m and L_m) are calculated from Equation 3.15.

Parameter	Capacitive Detection	Piezoresistive Detection
V_{DC1}, (V)	100	100
V_{DC2}, (V)	100	1
f_0, (MHz)	41.1091	41.1375
Q	228	1107
R_m, (Ω)	74.8k	15.4k
C_m, (F)	226.8a	227.1a
L_m, (H)	65.99m	65.99m
$\eta_e^2 (\frac{C^2}{m^2})$	17.4p	17.4p

and 15.4 kΩ for the piezoresistive readout. This result highlights the advantages of using the piezoresistive detection method to improve the output signal (see Table 4.4) and being able to decrease the bias voltage, that has been needed in the range of tens of volts..

4.5.2   Clamped-Clamped Beam (CCB) Resonator

The experimental characteristics of two fabricated CCB (see Table 4.1 with gaps 300 nm and 500 mn operated in lateral flexural mode, were extracted by means of the capacitive detection method (see Section 4.4.1) by applying an RF power of -20 dBm as it is included in Figure 4.21. A SEM picture of the 300 nm CCB is included in Figure 4.20.
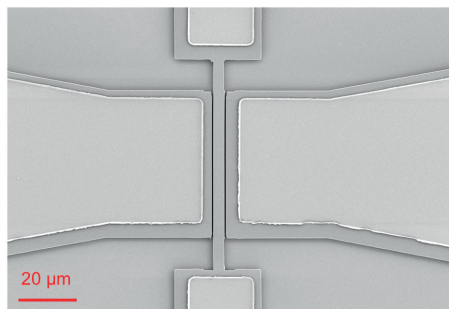
Figure 4.20 – SEM picture of the characterised CCB (see Table 4.1) with g = 300 nm. Motional parameters (R_m, C_m and L_m) are calculated from Equation 3.15.

The CCB with g = 500 nm performs noticeably worse than its counterpart of g = 300 nm, as it was expected: resonant peaks with a magnitude of approximately 3 dB have been obtained for the latter at V_{DC1} = V_{DC2} = 60V (Q = 201) while the 500 nm air-gap resonator achieved

(a) CCB with air-gap g = 300nm.

(b) CCB with air-gap g = 500nm.
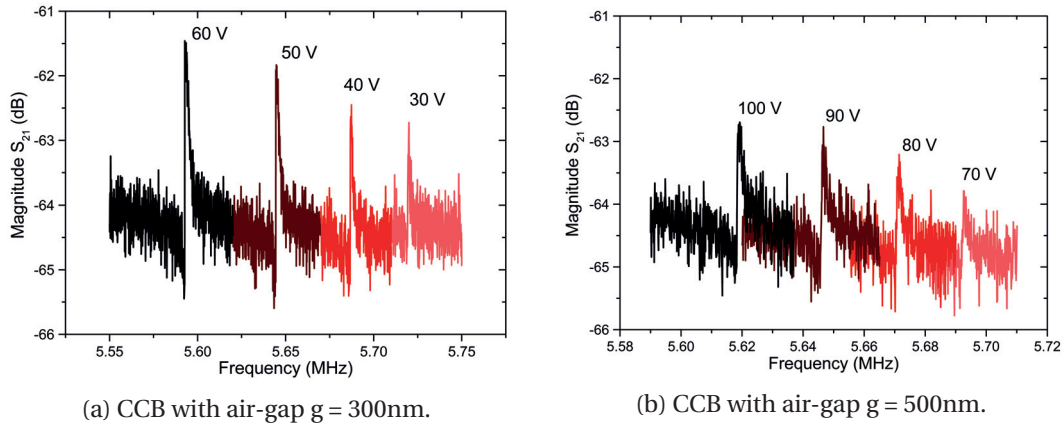
Figure 4.21 – Transmission S_{21} parameter for the CCB (see Table 4.1).

up to 1.4 dB at V_{DC1} = V_{DC2} = 70V (Q = 164). At a first glance, quality factor seemed to be measurable based on the 3 dB banwidth (BW) of the resonator (Equation 3.32), nevertheless, in Figure 4.22 it is revealed that the only applicable way to obtained an approximation for Q is the phase-slope method, validated in Appendix A.

By having a look into Table 4.5, the gap-scaling effect can be observed in the obtained coupling factor, which improves by a factor of almost six times in the same considered polarization conditions, having the consequent effect in the motional resistance, which decreases from 1.49 MΩ to 212.9 kΩ. The CCB extracted performance is very poor, but it has to be taken into consideration that these working devices were fabricated with too large air-gap, so far the results presented in this section are an experimental prove of the inference of gap-sizing and how it can be improved with the aim of the gap-filling (see Section 4.6).

Table 4.5 – Characteristic parameters comparison for CCB resonators with air-gaps g = 300 nm and g = 500 nm extracted from capacitive detection. Motional parameters (R_m, C_m and L_m) are calculated from Equation 3.15.

Parameter	g = 300 nm	g = 500 nm
V_{DC1}, V_{DC2}, (V)	60	70
f_0, (MHz)	5.5934	5.6925
Q	201	164
R_m, (Ω)	212.9k	1.49M
C_m, (F)	650a	114.7a
L_m, (H)	1.19	6.82
$\eta_e^2(\frac{C^2}{m^2})$	87.1f	15.4f
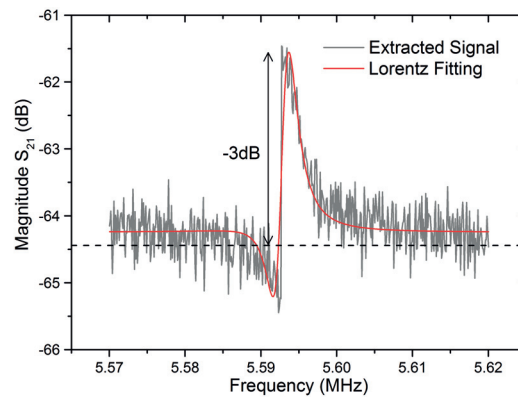
(a) Magnitude of the measured transmission parameter.
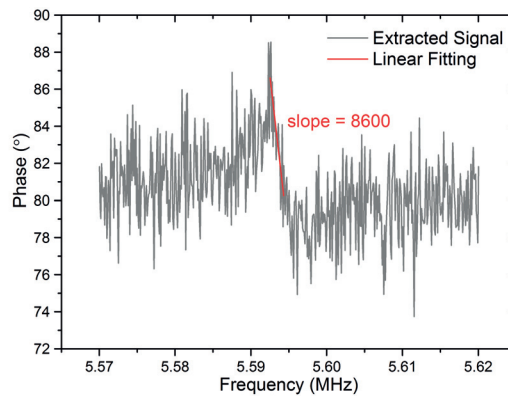
(b) Phase of the measured transmission parameter.

Figure 4.22 – Signal treatment of the extracted S_{21} parameters for the fabricated CCB ($l_b = 70$ μm, $w_b = 4$ μm and g = 300 nm, $V_{DC1} = V_{DC2} = 60$V).

4.5.3 Double-Ended Tuning Fork (DETF) Resonator

In order to accurately acquired the motional characteristics, the signal processing shown in Figure 4.23 (linear and Lorentz fittings) have been carried out for the measured DETFs.

The experimental characteristics of two fabricated DETF (Figure 4.24) with gaps of 100, 300 and 500 mn operated in lateral flexural mode, were extracted by means of the capacitive detection method (see Section 4.4.1) by applying an RF power of -20 dBm. A SEM picture of the 500 nm CCB is included in Figure 4.20

Quality factor of 1020, 227 and 126 were extracted for 100, 300 and 500 nm gaps, respectively,
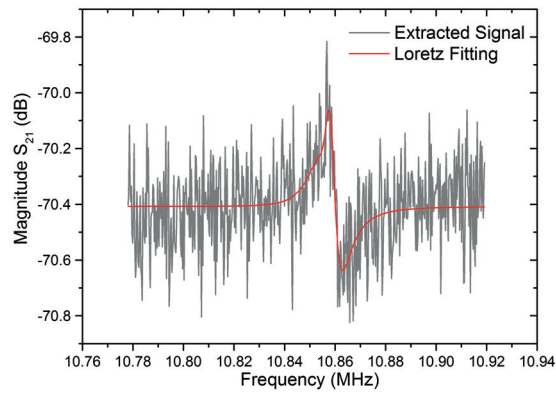
(a) Magnitude of the measured transmission parameter.
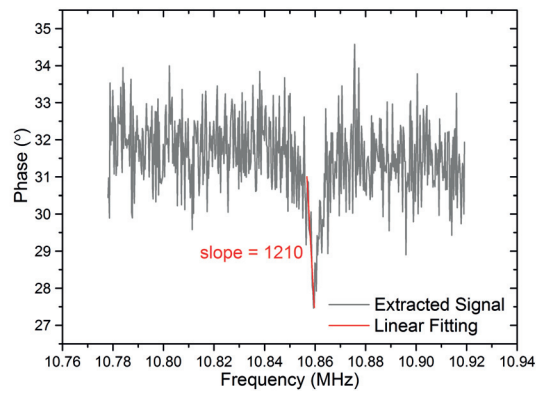
(b) Phase of the measured transmission parameter.

Figure 4.23 – Signal treatment of the extracted S_{21} parameters for the fabricated DETF (l_b = 40 μm, w_b = 3 μm and g = 300 nm, $V_{DC1} = V_{DC2} = 60$V).
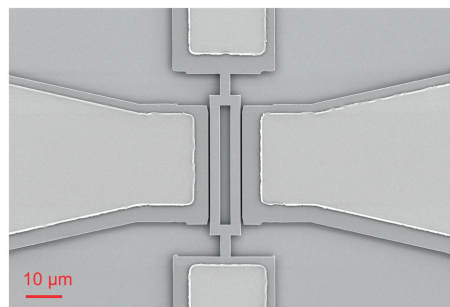
Figure 4.24 – SEM picture of the characterised DETF (see Table 4.1) with g = 500 nm.

being the DC bias $V_{DC1} = V_{DC2} = 50$ V for the first and $V_{DC1} = V_{DC2} = 100$ V for the two latter. As it was expected, the gap reduction is playing the dominant role to increase the electromechanical

coupling and so increase the measured device response and decrease its motional resistance. Table 4.6 shows the characteristic parameters variation with gap and DC bias voltage for the fabricated DETFs. The spectra comparison is included in Figure 4.25.
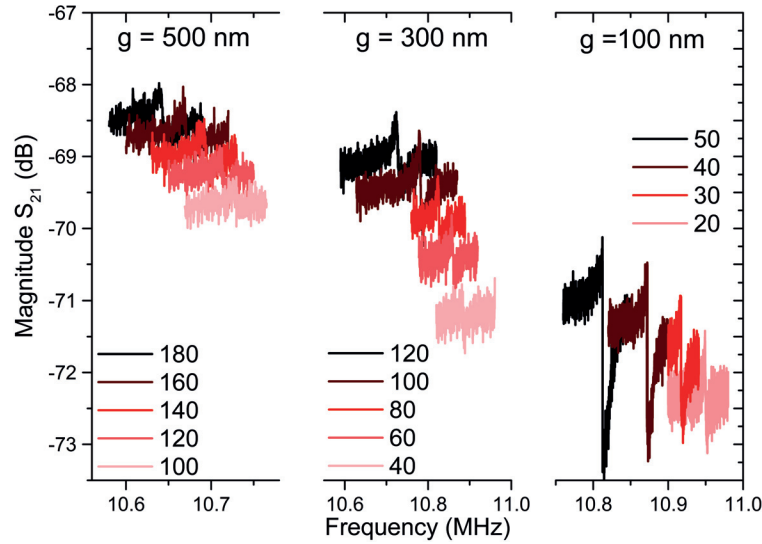
Figure 4.25 – Transmission S_{21} parameter for the DETF resonators (see Table 4.1).

Table 4.6 – Characteristic parameters variation with gap and DC bias voltage for the fabricated DETF. Motional parameters (R_m, C_m and L_m) are calculated from Equation 3.15.

Parameter	g = 100 nm	g = 300 nm	g = 500 nm
V_{DC1}, V_{DC2}, (V)	50	100	100
f_0, (MHz)	10.8124	10.7786	10.6398
Q	1020	227	126
$R_m{}^1$, (Ω)	3.3k	298k	4.1M
C_m, (F)	4.39f	218a	28.6a
L_m, (H)	49.3m	999m	7.7
$\eta_e^2 (\frac{C^2}{m^2})$	2.27p	112f	14.5f

4.5.4 Parallel Beam Resonators (PBR)

PBR involve parallel connected beams that vibrate as a fragmented membrane in an in-plane bulk length extensional mode. The PBRs in the present section were measured by means of a capacitive readout (RF power -20 dBm).

The transmission curves show the effect of parasitic vibration modes and feedthrough, which depends on: (a) the large overlap capacitance that those structures have in the transducer;

(b) the capacitive coupling through the substrate and (c) the interconnects parasitics [97]. Nevertheless, these parasitic effects do not obscure the observable signals, which are detected in the expected range of frequency of design (see Table 4.1) and they are modulated with variable DC voltages (see Figure 4.28). The side dimensions of the PBR presented below can be seen in Figure 4.26.
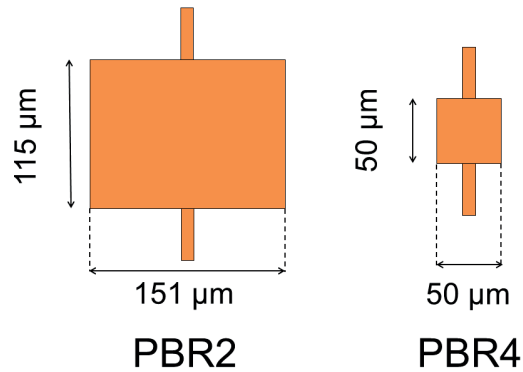
Figure 4.26 – Sides dimensions for the characterised PBR2 and PBR4.

Gap Sizing

The transducer size effect was studied by means of two PBR2 (see Table 4.1) with air-gap g = 100 nm (see Figure 4.27) and g = 300 nm and the results are shown in Figure 4.28. Regarding to the extracted quality factors, as it was expected, PBR2 with the smallest gap achieves a Q-factor of 3160, being 1.6 times better than the one of its counterpart of 300 nm (1963). In this case, the PBR2 with g = 300 nm exhibits a motional resistance of 1 MΩ and thanks to the gap reduction the motional resistance gets reduced up to 4.43 kΩ for the 100 nm air-gap PBR2.
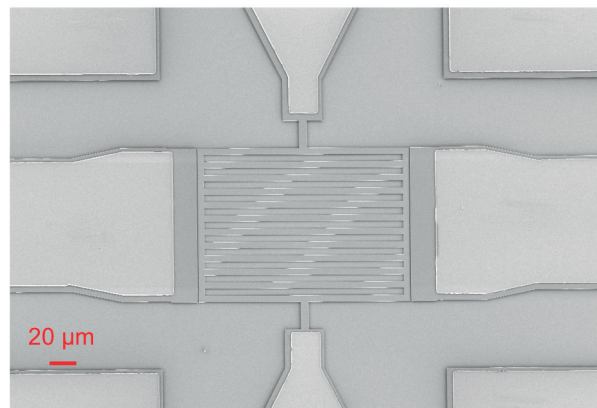
Figure 4.27 – SEM picture of the characterised PBR2 (see Table 4.1) with g = 100 nm.
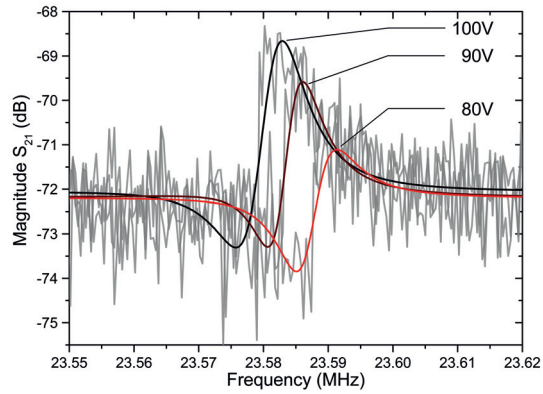
(a) Gap g = 100nm.
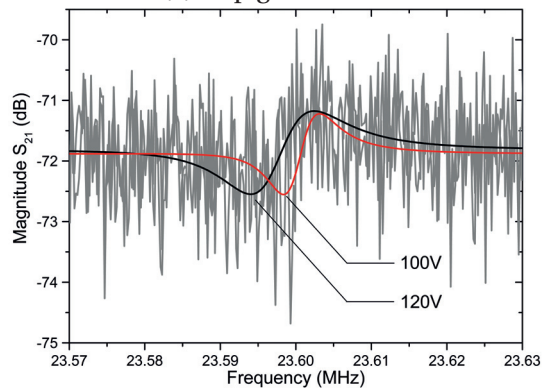
(b) Gap g = 300nm.

Figure 4.28 – Transmission characteristics of two PBR2 (see Table 4.1) with gap (a) g = 100 nm and (b) g = 300 nm. Gray lines: direct extracted signal. Solid lines: Lorentz fitting.

Table 4.7 – Characteristic parameters of the fabricated PBR2 resonators. Motional parameters (R_m, C_m and L_m) are calculated from Equation 3.15.

Parameter	g = 100 nm	g = 300 nm
V_{DC1}, V_{DC2}, (V)	100	100
f_0, (MHz)	23.5925	23.6026
Q	3160	1963
$R_m{}^2$, (Ω)	4.43k	1M
C_m, (F)	311a	2.1a
L_m, (H)	61.1m	9m
$\eta_e^2(\frac{C^2}{m^2})$	176p	2.18p

Structure Dimensioning

In order to evaluate how beam dimensions and effective mass influence the quality factor and motional parameters (see Section 3.3.3), two different PBRs with the same transduction air-gaps were compared: (a) PBR2, actuation area A = 115 μm^2 and (b) PBR4, actuation area A = 50 μm^2 shown in Table 4.1.
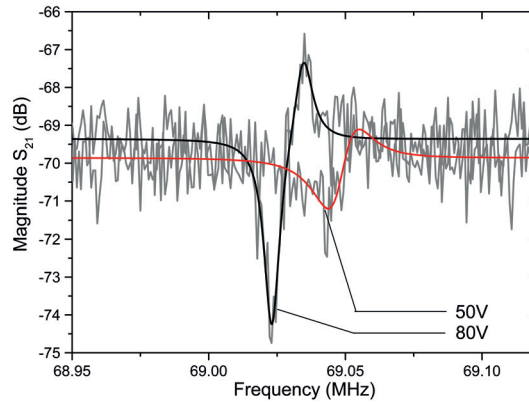
Figure 4.29 – Transmission characteristics of the fabricated PBR4 (g = 100 nm). Gray lines: direct extracted signal. The Lorentz fittings are superposed to the measurements.

Table 4.8 – Characteristic parameters of the fabricated PBR (g = 100 nm). Motional parameters (R_m, C_m and L_m) are calculated from Equation 3.15.

Parameter	PBR4	PBR2
V_{DC1}, V_{DC2}, (V)	80	80
f_0, (MHz)	69.0569	23.5925
Q	4247	3164
R_m, (Ω)	14.15k	7.5k
C_F, (Ω)	38.3a	182a
L_H, (Ω)	138m	104m
$\eta_e^2(\frac{C^2}{m^2})$	12.5p	113p
A (μm^2)	50	115
k_{eff} ($\frac{N}{m}$)	327k	617k
m_{eff} (g)	1.74p	1.18p

The resulting parameters are listed in Table 4.8. PBR4 has a better performance in terms of quality factor than PBR2, even if the latter has higher effective mass and stiffness and coupling factor. In Figure 4.29 it can be seen that the PBR4 acquired signal it is more noisy, and that the fitting of the resonance peaks is poorer, therefore that can have influenced the Q-factor acquisition based on the slope-phase method. Nonetheless, the importance of the actuation area can be observed in the lower extracted motional resistance and higher coupling factor

(up to 9 times better) for PBR2.

4.5.5 Wine-Glass (WG) Disk Resonator

WGD resonators (see Figure 4.30) have been characterized by measuring the direct transmission S-parameters with the piezoresistive setup with an RF excitation of -20 dBm. The effect of the gap sizing for two disk of radius R = 30 μm with nanometric air-gaps of 100 and 300 nm, respectively is included in Figure 4.31. The quality factor falls from 1482 to 368 and the motional resistance increases from 4.49 kΩ to 1.46 MΩ when the gap is increased from 100 to 300 nm. The gap reduction means a increase up to 4 times of the quality factor and up to 81 times of the coupling factor, leading to an decrease of the motional impedance in the range of several kΩ (see Table 4.9).
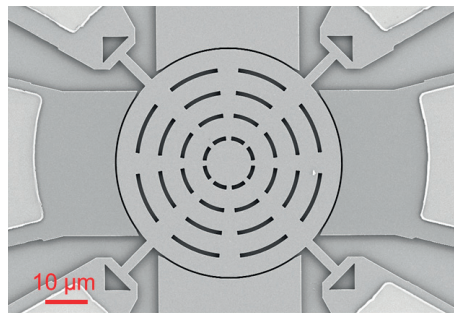
Figure 4.30 – SEM picture of the characterised WGR (see Table 4.1) with g = 100 nm.
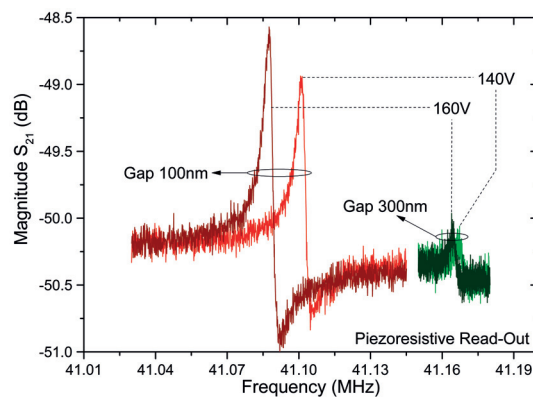
Figure 4.31 – Comparison between the piezoresistive detection of transmission parameter S_{21} response for two WGD resonators with air-gaps of 100 and 300 nm.

Table 4.9 – Characteristic parameters of the described WGD (R = 30 μm) extracted from piezoresistive detection. Motional parameters (R$_m$, C$_m$ and L$_m$) are calculated from Equation 3.15.

Parameter	g$_{air}$ = 100 nm	g$_{air}$ = 300 nm
V$_{DC1}$, (V)	160	160
V$_{DC2}$, (V)	1	1
f$_0$, (MHz)	41.0855	41.1651
Q	1482	368
R$_m$, (Ω)	4.49k	1.46M
C$_m$, (F)	582a	7.19a
L$_m$, (H)	25.7m	2.1
$\eta_e^2(\frac{C^2}{m^2})$	44.6p	550f

4.5.6   Square Plate Resonator

An square plate resonator SPR1 (see Figure 4.32) with air-gaps g = 100 nm was characterized by means of a capacitive detection with RF power -20 dBm. As the resonance peak at V$_{DC1}$ = V$_{DC2}$ = 120V is higher than 3 dB, the Q-factor of the device has been calculated with the aim of both BW and phase-slope approximation (see Appendix A), resulting in Q$_{BW}$ = 844 and Q$_{ph}$ = 784. With the purpose of being able to do a consistent comparison with the 100 nm air-gap WGD presented in the previous section (V$_{DC1}$ = 120V, V$_{DC2}$ = 1V) the characteristic motional parameters have been calculated by considering Q = 784 and they are included in Table 4.10, jointly with the ones calculated for the WGD resonator.
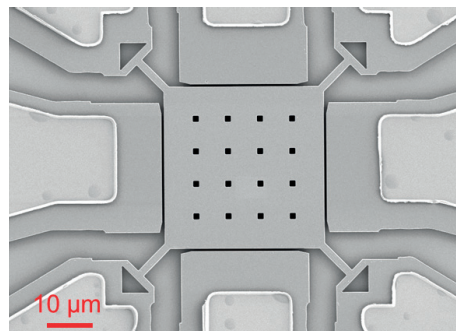
Figure 4.32 – SEM picture of the characterised SPR (see Table 4.1) with g = 100 nm.

If the square plate is compared with the WGD resonator presented above, both vibrating in a similar bulk mode of resonance, it is observed a better quality factor and lower motional resistance in case of the WGD. The factors that produce such a difference are: (a) piezoresistive detection has been proven to perform better than capacitive one (see Section 4.5.1); (b) the
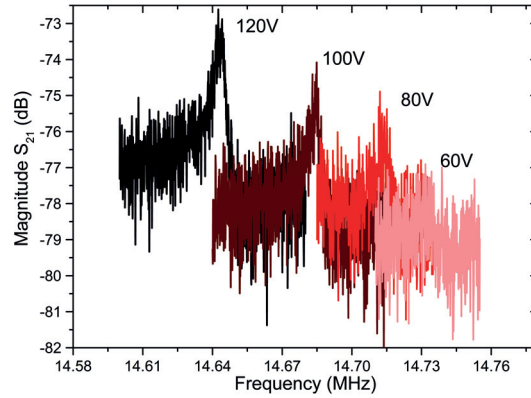
Figure 4.33 – Experimental transmission parameters for a l_p = 20 μm side and g = 100 nm gap square resonator.

Table 4.10 – Characteristic parameters of a square plate resonator (l_p 20 μm, g = 100 mn) at 120V. Motional parameters (R_m, C_m and L_m) are calculated from Equation 3.15.

Parameter	Square Plate	WGD
V_{DC1}, (V)	120	120
V_{DC2}, (V)	120	1
f_0, (MHz)	14.6402	41.1105
Q	784	1256
R_m, (Ω)	11.245k	9.4k
C_m, (F)	1.145f	327.2a
L_m, (H)	103m	45.8m
$\eta_e^2(\frac{C^2}{m^2})$	4.52p	44.6p

actuation area of the WGD is larger (A_{disk} = 47.1 μm^2) than for the square plate resonator (A_{plate} = 20 μm^2) and (c) both effective mass and stiffness are larger for the WGD (k_{eff} = 76600 $\frac{N}{m}$ and m_{eff} = 1.14 pg) than for the square plate (k_{eff} = 3943 $\frac{N}{m}$ and m_{eff} = 0.465 pg). Calculations have been done by means of the equations presented in Section 3.3.1.

4.6 Partially-Filled-Gap Capacitive MEMS Resonators

4.6.1 Impact in Signal Level

Equivalent Capacitance in the gap

As it is discussed in Section 3.2.5, MEMS resonators gap-filling via a high-k dielectric is an effective way to improve the overall equivalent capacitance value existing between electrodes

and resonator [30] [31] and therefore the capacitive coupling, which is inversely proportional to the gap width and governs the output current (see Sections 3.2.3 and 3.2.4). As motional resistance is sensitive to final gap spacing, the motional impedance is indeed lowered.

One of the methods that has been proposed in order to reduce the transduction gap is to fill the gap with a high-k dielectrics by means of Atomic Layer Deposition (ALD) methods [30]. As it is explained in Section 4.3.2, a conformal layer of several nanometers is deposited all around the structure, partially closing the air space and thus attaining sub-micron high-aspect-ratio gaps. Moreover, structures are better consolidated for inertial mass sensing and they are more robust against electrodes-resonator collapse by electrical stiction [31].

From now on, the gap-space filled by HfO_2 will be referred as g_{HfO2} and considers the addition of the two sidewall layers. Therefore if an ALD HfO_2 layer of 5 nm is deposited in a resonator with initial air-gap of 100 nm, after the deposition we will have g_{air} = 90 nm and g_{HfO2} = 10 nm).

Energy Losses

Hafnium oxide (HfO_2) was proposed to be the filling material of the gaps due to its high dielectric constant and relatively high thermal stability with respect to a silicon surface, which make HfO_2 a extremely interesting material for enhanced performance of MEMS resonators fabrication. The main drawback that was reported for HfO_2 partially-filled gaps was the observed lowering of the quality factor after the ALD coating [30]. This worsening was ascribed to losses introduced by the HfO_2 film due to two factors: (1) additional parasitics interconnects coming from the poor contact probe-electrode and (2) further energy dissipation at the interface polysilicon-HfO_2.

Taking into consideration (1), the ALD process conformally coats every exposed surface with HfO_2, but only the HfO_2 film in the transduction gap contributes to coupling enhancement. Probe-to-electrode contacts worsen after each deposition and the acquired signal floor level changes from measurement to measurement. This fact suggest the need of locally removed the undesired HfO_2 film in future resonators batches.

If we focus on (2), HfO$_2$ on top of and beneath the disk resonator does not help reduce the gap spacing; even worse, it dissipates energy. There are two approaches for minimizing the energy dissipation at the Si-HfO$_2$ interface. One approach is to minimize the energy dissipation per unit area by smoothing the surface roughness. In our case this is carried out thanks to have silicon as structural material (and not polysilicon [30] and the thermal oxidation performed to minimize the gap sidewalls scalloping (see Section 4.3.1). The second approach is to reflow silicon by means of annealing in order to to smooth the surface, which was also carried out during ALD, as the substrate was kept at 200° (see Section 4.3.2).

Dielectric Charging

Net charge in the HfO$_2$ or at the oxide-silicon interface, can impose a change in electrical stiffness that will pull the frequency of the resonator up or down, according to the sign of the net charge and the polarity of DC bias. The existence of such charge has been proven to be eliminate by means of annealing [30] [31], therefore it may be reduced by means of the ALD process itself. Nevertheless, this effect was beyond the scope of this thesis and remains as a future characterization step.

Stress and Coefficient of Thermal Expansion (CTE)

Films made by ALD have been shown to face challenges when directly grown onto surfaces, including differing nucleation and growth rates across the surface, stress, thermal expansion and elastic mismatches and particle contamination that may impact the performance of the material [98].

At the interface between HfO$_2$ and silicon the stress is larger, the bonds strengths are weaker and there is a mismatch between the coefficient of thermal expansion (CTE) of HfO$_2$ [99] and the one of silicon [100]. Therefore, further studies about the linearity and stability of the MEMS resonators presented below remain as future characterization steps.

In the next sections, the improvements achieved by filling the air-gaps of diverge flexural and bulk resonators with HfO$_2$ are shown.

Double-Ended Tuning Fork (DETF) Resonator

The experimental transmission parameters for a DETF (length, l_b = 40 μm and air-gap g = 300 nm) before and after sequential HfO$_2$ depositions have been extracted (see Section 3.2.3) and they are presented in Figure 4.34. Notice that the frequency axis range has been kept 0.15 MHz for (a) and 0.03 MHz in (b-d) for a better visualization.

Three conformal thin layers of ALD HfO$_2$ that have been deposited on the DETF: the first and second had a of 5 nm and the third one of 10 nm. The device performance is proven to improve after the first deposition (see Figure 4.34.b). The signal amplitude becomes sharper (see frequency scale) and increases from 3.88 to 4.6 dB, considering the amplitude from the peak to the noise floor. Similarly the slope becomes steeper, increasing in a factor of 9 times, effect that implies a direct improvement in the Q-factor according with the study done in Appendix A: Q(g = 300 nm) = 963, Q(g = 290 nm) = 8433, Q(g = 280nm) = 1812 and Q(g = 240 nm) = 1768. As it can be seen, after the first deposition the Q-factor improves up to a factor of 8.8 times. Concerning the motional impedance it has been proven to be reduced up to 10 times after the first deposition (see Table 4.11).

It has been observed that after several deposition, the signal performance has decayed (see Figure 4.34.c), nevertheless, the extracted response after the last deposition of 10 nm (Figure 4.34.d) is always better than the initial one, whereby this signal degradation was attributed due to the worsening of the contact of the probe on the covered electrodes.

Table 4.11 – Experimental characteristic parameters of the fabricated DETF with the original 300 nm air-gap and after each HfO$_2$ deposition (DC bias V$_{DC1}$ = V$_{DC2}$ = 90V and RF power -20 dBm. Motional parameters (R$_m$, C$_m$ and L$_m$) are calculated from Equation 3.15.

Parameter	g$_{air}$ = 300 nm	g$_{air}$ = 290 nm g$_{HfO2}$ = 10 nm	g$_{air}$ = 280 nm g$_{HfO2}$ = 20 nm	g$_{air}$ = 260 nm g$_{HfO2}$ = 40 nm
f$_0$	11.0387	10.8516	10.6816	10.4105
Q	963	8433	1812	1768
R$_m$, (Ω)	88.8k	8.7k	35.5k	27.3k
C$_m$, (F)	169a	199a	228a	304a
L$_m$, (H)	1.23	1.1	943m	707m
$\eta_e^2(\frac{C^2}{m^2})$	90.6f	103f	119f	188f

The effect of the contact impoverishment after each deposition can clearly seen in Figure 4.34,
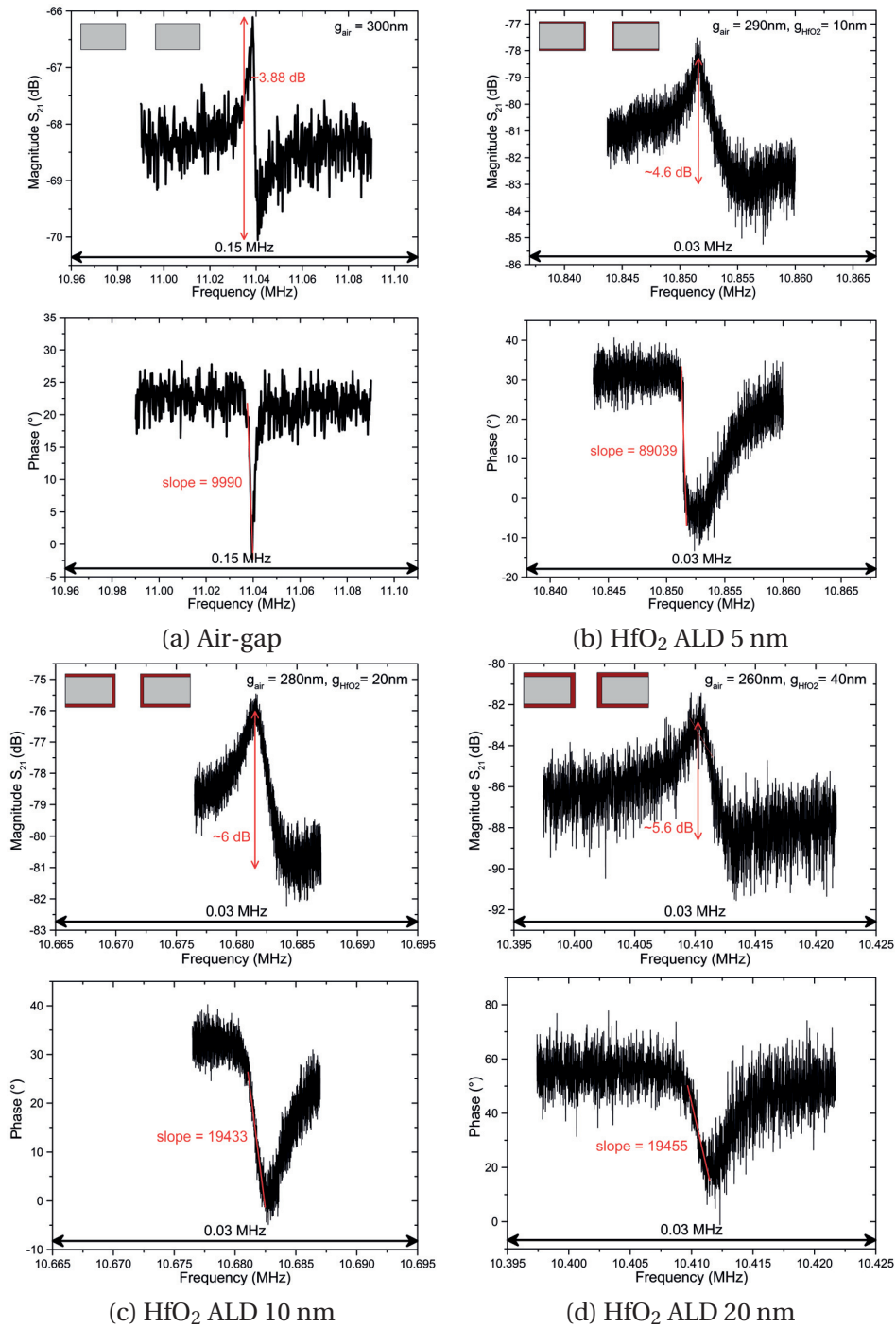
Figure 4.34 – Experimental transmission parameters for a DETF with an initial air-gap of 300 nm and three consecutive HfO$_2$ depositions of thickness 5 nm, 5 nm and 10 nm: (a) 300 nm air-gap; (b) 20 nm air-gap and 10 nm HfO$_2$; (c) 280 nm air-gap and 20 nm HfO$_2$ and (d) 260 nm air-gap and 40 nm HfO$_2$. The applied DC bias V$_{DC1}$ = V$_{DC2}$ = 90V and the RF power -20 dBm. Notice that the frequency scales are different for (a) and (b-d).

where it is shown how the signal floor level changes after each added HfO$_2$ layer, being observed a lowering of the transmission level of the signal of -12 dB after the first deposition (5 nm), +2 dB after the second deposition (5 nm), and -6 dB after the last deposition (10 nm). In order to ascertain how HfO$_2$ gap-filling behaves with DC bias modulation, the DETF has been capacitively excited and measured for several voltages as it is depicted in Figure 4.35. The frequency downshift is slightly larger for the 20 nm covered DEFT, around 19 kHz averaged downshift for $+\Delta V_{DC1} = +\Delta V_{DC2} = 10$ V, than for the uncovered resonator, 17.18 kHz.
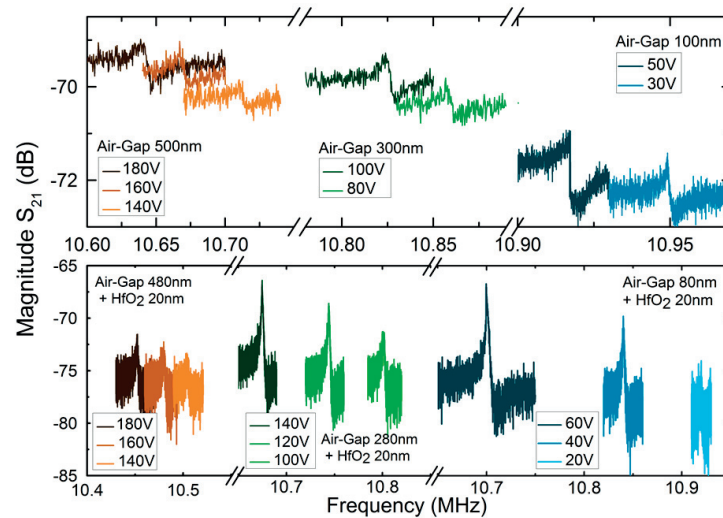
Figure 4.35 – Characteristics parameters after each HfO$_2$ deposition for DETF resonators with three different initial air-gaps: 100 nm (right), 300 mn (middle) and 500 nm (left).

The effect of HfO$_2$ gap-filling for DETFs with different initial air-gaps (100 nm, 300 mn and 500 nm) is illustrated in Figure 4.35. The resulting responses for the same structures before (top) and after the ALD (bottom) excited at bias depict that the partially-filled gaps resonators overperform their previous response with air-gaps, showing a detection enhancement of more than 6 dB. After the ALD, resonance frequency shift down showing that the HfO$_2$ loaded mass plays a more important role in the resonance modulation than the eventual DETF mechanical stiffening coming from the high-k HfO$_2$ mass load (see Section 3.2.6). Partially-filled HfO$_2$ gaps performs better than air gaps suggesting a potential enhanced detection for atmospheric operation (see Section 4.6.3). In addition, the frequency shift versus applied voltage (sensing resolution) remains as good as for air-gap flexural mode DETF (see Figure 4.36).
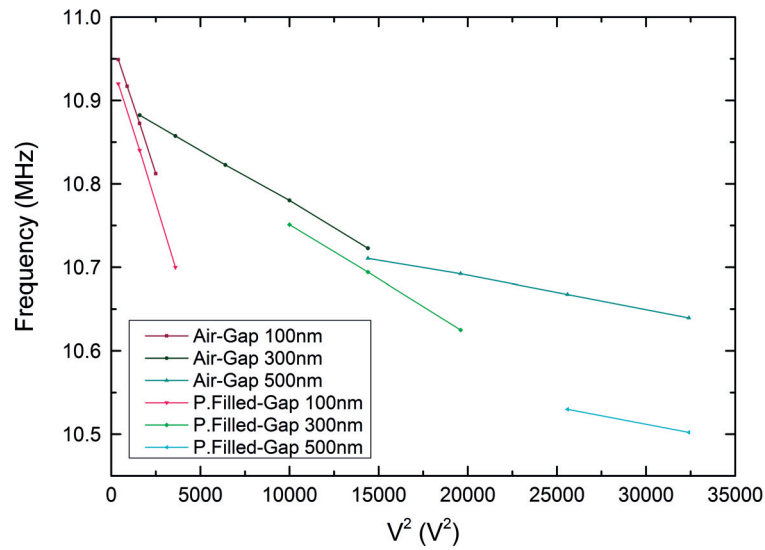
Figure 4.36 – Frequency versus the square applied voltage for different air and filled gaps dimensions.

Wine-Glass Mode Disk Resonator

The same experiment that has been explained above was carried out for 100 nm air-gap WGD resonators with radius R = 30 μm (see Table 4.1). For this kind of device either capacitive and piezoresistive measurements were able to be extracted and compared as it is shown in Figure 4.37. Here, detection methods show similar slopes for the resonance frequency downshift after each HfO$_2$ deposition, nonetheless, the needed actuation DC voltages are much lower for the piezoresistive one, proving once again the enhancement that piezoresistive effect current provides in RF MEMS characterization.

The frequency spectra of the WGD presented above, was measured by means of the piezoresistive detection method with variable V_{DC1} and V_{DC2} = 1 V before and after the first 5 nm of HfO$_2$ and it is illustrated in Figure 4.38. As it is shown, the output signal after the ALD coating is less noisy and the peak increased up to 1.75 times from the signal floor to the resonance peak.

In order to evaluate the evolution of the signal after each deposition as it has been done for the DETF above, V_{DC1} = 50 V and RF power -20 dBm were kept as actuation signals and amplitude-phase changes were tracked. As it is depicted in Figure 4.39, there is a signal enhancement after the first deposition that perishes with the subsequent ones. Here, the measured amplitude is
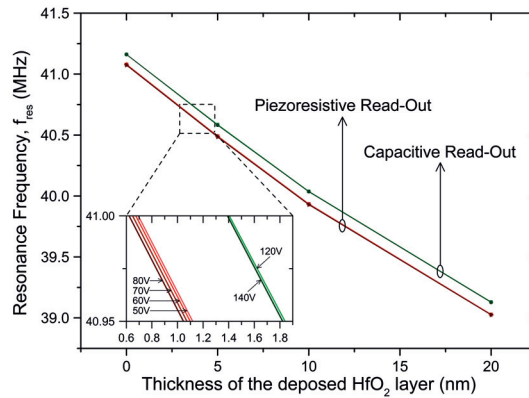
Figure 4.37 – Resonance frequency, f_0, shifts for a WGD after successive depositions of nano-metric HfO_2 ALD layers.

(a) 100nm air-gap.

(b) 90nm air-gap and 10nm HfO_2.
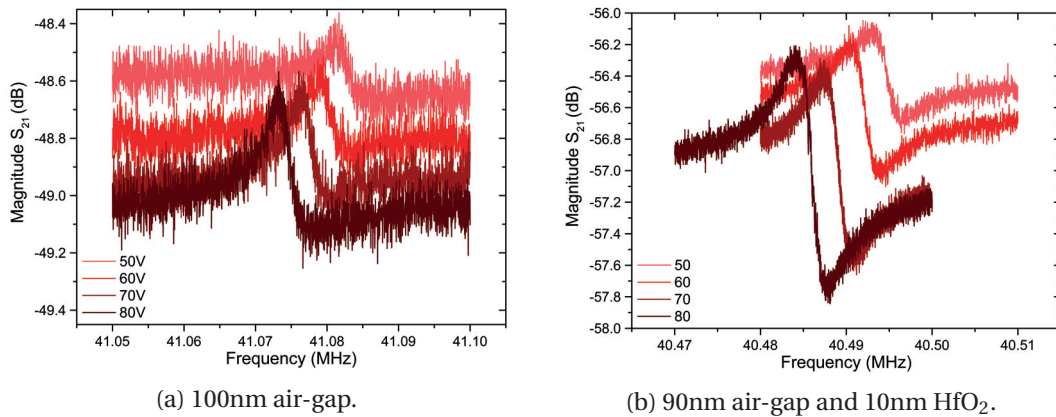
Figure 4.38 – Frequency spectra for a WGD for different bias voltages before (a) and after (b) the first HfO_2 deposition of 5nm.

always kept beyond the initial signal measured along the 100 nm air-gap, nevertheless, the slope sharpness, which improves from 426 to 1186 during the first ALD (Figure 4.39.b) worsens after the third deposition (Figure 4.39.d).

The characteristic parameters extracted for this device are included in Table 4.12 and they reveal worse Q-factor and motional resistance improvements than for the DEFT (see Table 4.11), however it has to be considered that the initial extracted Q-dactor and R_m were lower for the WGD. As it has been discussed in Section 4.6.1, energy losses have been attributed to the HfO_2-silicon interface, hence more energy dissipation is expected in bulk resonators than in flexural resonators due to the larger surfaces.

(a) AIR GAP

(b) HfO_2 ALD 5 nm

(c) HfO_2 ALD 10 nm

(d) HfO_2 ALD 20 nm
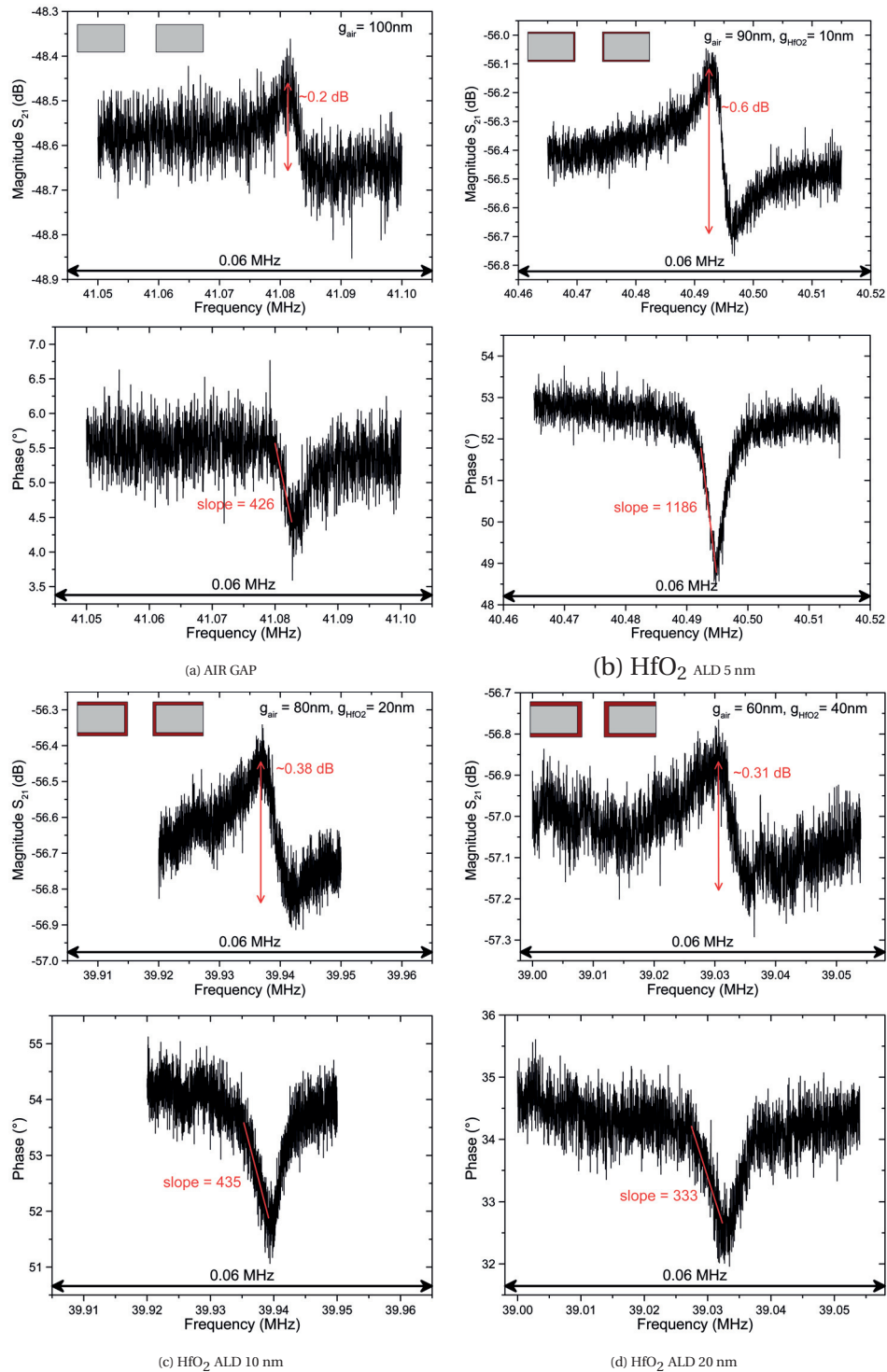
Figure 4.39 – Experimental transmission parameter for a WGD with an initial air-gap of 100 nm after consecutive HfO_2 deposition: (a) 100 nm air-gap; (b) 90 nm air-gap and 10 nm HfO_2; (c) 80 nm air-gap and 20 nm HfO_2 and (d) (b) 60 nm air-gap and 40 nm HfO_2. The applied DC bias was 50 V and the RF power -20 dBm.

Table 4.12 – Experimental characteristic parameters of the fabricated WGD with the original 100 nm air-gap and after each HfO_2 deposition (DC bias $V_{DC1} = V_{DC2} = 80$ V and RF power -20 dBm). Motional parameters (R_m, C_m and L_m) are calculated from Equation 3.15.

Parameter	g_{air} = 100 nm	g_{air} = 90 nm g_{HfO2} = 10 nm	g_{air} = 80 nm g_{HfO2} = 20 nm	g_{air} = 60 nm g_{HfO2} = 40 nm
f_0, (MHz)	41.0733	40.4843	39.9413	39.0257
R_m, (Ω)	146.3k	43.3k	53.8k	23.8k
C_m, (F)	56.8a	88.2a	143a	454a
L_m, (H)	263m	175m	110m	36.6m
$\eta_e^2 (\frac{C^2}{m^2})$	4.35p	6.56p	10.4p	31.3p
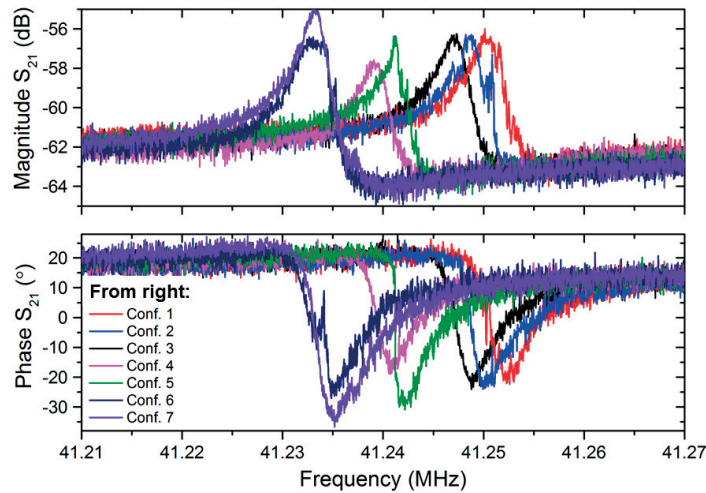
Figure 4.40 – Multigate operation for a WGD resonator (R = 30 μm, g_{HfO2} = 20nm, g_{air} = 80 nm) by keeping V_{DC1} = 1 V and RF power -25 dBm) and varying the bias voltages V_{DC2}, V_{DC3} and V_{DC4}.

In order to study the effect that a variable number of AC and DC probes has in the piezoresistive response (as explained in Section 3.2.4), a WGD resonator (R = 30 μm, g_{air} = 80 nm, g_{HfO2} = 20 nm) has been measured for different excitation configurations: (1) AC voltage, $+v_{ac}$ and DC voltages, $+V_{DC1}$ and $+V_{DC2}$; (2-3) AC voltage, $+v_{ac}$ and DC voltages, $+V_{DC1}$, $+V_{DC2}$, $+V_{DC3}$ and $+V_{DC4}$; (4) AC voltage, v_{ac} and DC voltages, $+V_{DC1}$, $+V_{DC2}$, $+V_{DC3}$; (5) AC voltage, v_{ac} and DC voltages, $+V_{DC1}$, $+V_{DC2}$, $-V_{DC4}$; (6) AC voltage, v_{ac} and DC voltages, $+V_{DC1}$, $+V_{DC2}$, $+V_{DC3}$ and $-V_{DC4}$ and (7) AC voltage, v_{ac} and DC voltages, $+V_{DC1}$, $+V_{DC2}$, $-V_{DC3}$ and $-V_{DC4}$. As it is depicted in Figure 4.40, this WGD resonator provided a better transmission signal due to the amplification coming from the piezoresistive effect (configuration 7).

Table 4.13 – Experimental bias configuration and resulting parameters for the multi-gate actuated WGD resonator (RF power -20 dBm, V_{DC1} = 80 V, V_{DC2} = 1 V). Motional parameters (R_m, C_m and L_m) are calculated from Equation 3.15.

Parameter	Conf.1	Conf.2	Conf.3	Conf.4	Conf.5	Conf.6	Conf.7
V_{DC3}, (V)	0	40	80	80	0	80	-80
V_{DC4}, (V)	0	40	80	0	-80	-80	-80
f_0, (MHz)	41.2507	41.2487	41.2470	41.2412	41.2391	41.2331	41.2331
Q, (by BW)	7500	9015	7953	10815	7951	7950	11760
Q, (by phase-slope)	8006	9059	8192	9989	8025	8493	12163
R_m, (Ω)	1.49k	1.25k	1.41k	1.04k	1.41k	1.41k	874

Q-factors of the order of several thousands have been calculated by means of the BW and the phase-slope methods and they have proven to be pretty similar (see Table 4.13). The motional resistance have been calculated with Equation 3.15 by taking into consideration $V_{bias} = V_{DC1}$, nonetheless, due to the increasing number of actuated transduction gaps for the three and four gates configuration, it is expected a larger relaxation in the effective stiffness due to the increase of the electrical spring contant (see Equation 3.30), hence the motional resistance could be even lower.

Square Plate Resonator

The experimental characteristics for a SPR2 (see Table 4.1) with initial air-gaps g_{air} = 100 nm at a RF power -20 dBm are shown in Figure 4.41. The obtained motional parameters are summarised in Table 4.14.

Table 4.14 – Experimental characteristic parameters for the fabricated square plate (l_p = 30 μm, g_{air} = 80 nm, g_{HfO2} = 20 nm). Motional parameters (R_m, C_m and L_m) are calculated from Equation 3.15.

Parameter	Square Plate
V_{DC1}, V_{DC2}, (V)	160
f_0, (MHz)	9.9707
Q	780
R_m, (Ω)	3k
C_m, (F)	6.6f
L_m, (H)	38m
$\eta_e^2 (\frac{C^2}{m^2})$	27.2p
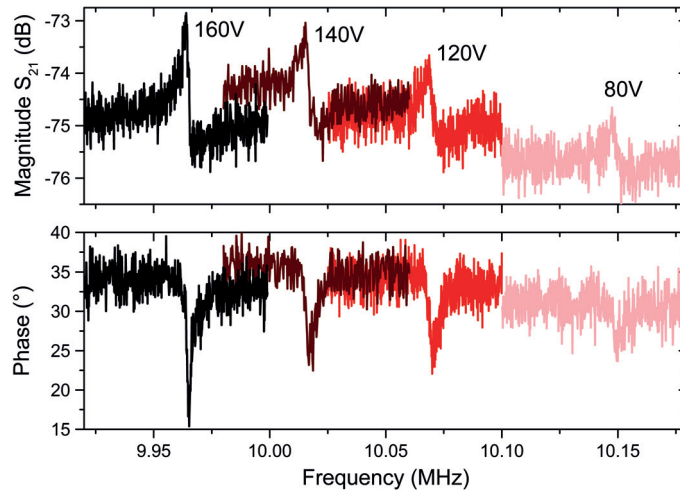
Figure 4.41 – Frequency spectra as as function of DC bias for the fabricated square plate resonator.

4.6.2 RF Power Handling

Unlike quartz crystals, where the maximum power handling is limited by the sustaining electronics, the power handling in MEMS resonators is limited by device nonlinearities [101] [102].
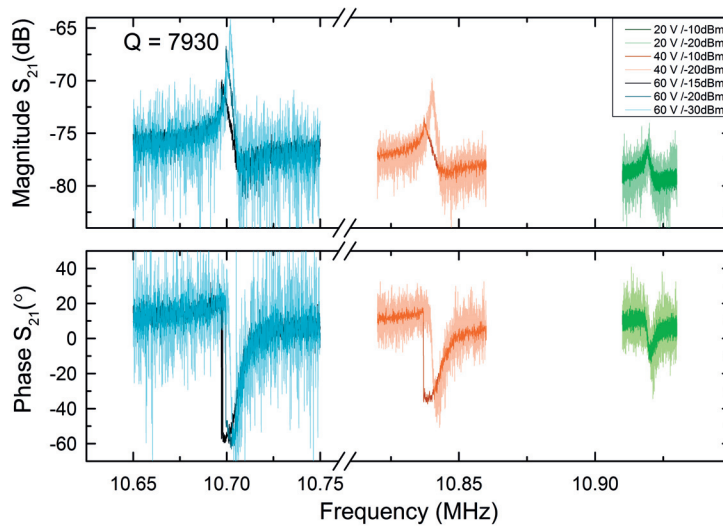
Figure 4.42 – Transmission parameter S_{21} response in magnitude and in phase for a DETF 80nm partial-filled 20nm HfO_2 gap at different DC/RF applied signals.

The oscillation amplitude is directly determined by the applied AC voltage (see Section 3.2.6). If the AC voltage is too low, the noise level buries the small signal generated by the motional

current. By contrary, if the AC voltage is too high, it may be a cause of electrical and mechanical nonlinearities [103] that cause a bifurcation of the resonator response [102].

In Figure 4.42 an incipient nonlinear behaviour can be observed for the case of a partially-filled gap DETF resonator (g_{air} = 80 nm, g_{HfO2} = 20 nm). Having a closer look for a bias of 60 V in Figure 4.43.b, peak bifurcation starts to be observable for values over -20 dBm, suggesting a spring softening due to the left-tilting of the peak [101]. For AC values of -15 dBm (Figure 4.43.c), the transmission peak decreases and shifts towards lower frequencies showing a stronger nonlinear peak bifurcation of the frequency-amplitude relation. This result suggests that the maximum AC power to be applied in this kind of devices should be kept should not be larger than -20 dBm.

| (a) 60 V/-30 dBm. | (b) 60 V/-20 dBm. | (c) 60 V/-15 dBm. |
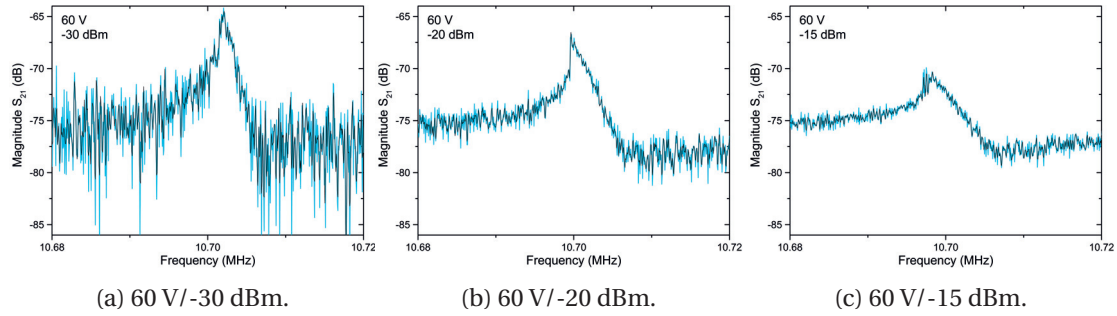
Figure 4.43 – Experimentally acquired electrical nonlinear behavior (spring softening) of a DETF (g_{HfO2} = 20nm, g_{air} = 80nm).

Nevertheless, as the oscillation amplitude of the resonators is directly determined by the applied AC voltage, it is critical not to apply too low AC signals. In Figure 4.44 the transmission parameters of a WGD at V_{DC1} = V_{DC1} = 180 V are shown for different AC powers, proving the impoverishment of the signal at -20 dBm. In this case, the peak does not show at -10 dBm (black line) and -20 dBm (gray line), the output signal is more difficult to recognize. By comparing this result with the one presented above for a DETF (bifurcation at 60V/-20dBm), we can see that the power handling has to be studied for each particular device.

On the other hand, extreme AC and DC biasing can cause mechanical nonlinearities in the devices. This effect has been observed for a WGR ((DC bias at 180 V and AC signal up to 0 dBm)) in Figure 4.45). A right-tilt of the peak is observed to increased with AC signal levels from -30 dBm (brown line) to 0 dBm (red line), giving rise to a strong decrease of Q and a right
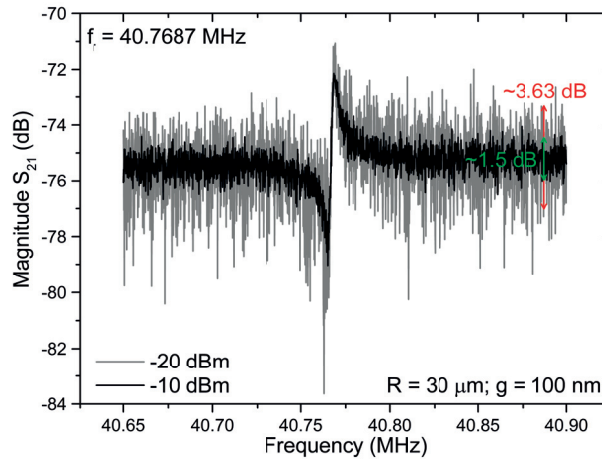
Figure 4.44 – Impoverishment of the transmission parameter S_{21} response for a WGD by means of the noise (R = 30 μm, (g_{HfO2} = 20 nm, g_{air} = 80 nm)) at low RF applied signals.

shifting of the resonant frequency of the order of tens of kHz.
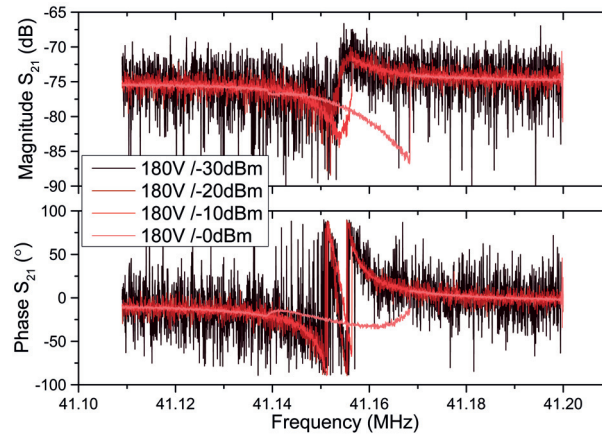
Figure 4.45 – Experimentally acquired mechanical nonlinear behavior of a WGD (R = 30 μm, (g_{HfO2} = 20 nm, g_{air} = 80 nm).

4.6.3 Air Damping

As it is detailed in Section 3.2.6, air damping is among the most important factors that bring down MEMS resonators performance. The most common solution is the device packaging in vacuum conditions. Nevertheless, if the resonator is intended for sensing applications, this is often not possible, therefore, high quality factors are needed in order to overcome the air damping degradation by keeping a detectable output signal. Figure 4.46 shown a comparison between atmospheric pressure and vacuum conditions for two DETF resonators with air and

partially filled gaps.
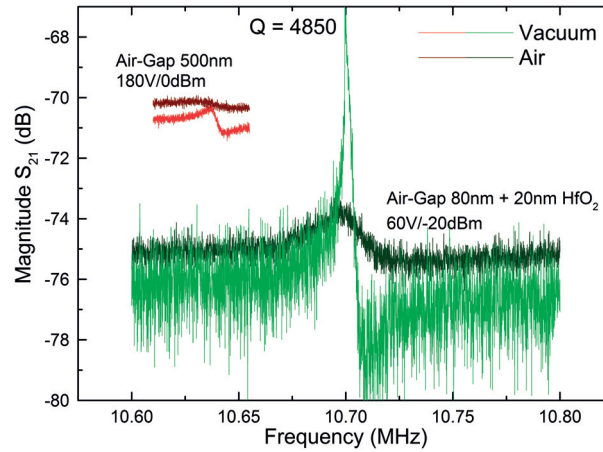
Figure 4.46 – Frequency characteristics of an air-gap versus partially-filled HfO_2 gap DETF both measured at atmospheric pressure and vacuum (10_{-5} mbar).

4.6.4 Anchors Damping

As it is widely studied in Section 3.2.6, anchors damping is one of the main sources of the energy losses of a suspended structure, which has repercussions on the quality factor deterioration. In order to determine their effect in the case of a WGD resonator, two anchors designs were fabricated and electrically characterised by capacitive and piezoresistive detection methods as sketched in Figure 4.47 [104].

Oppositely to what was expected, WGD resonators performance worsens for the design with less anchoring points. A decay up to 10.2 dB was observed with the purely capacitive measurement (Figure 4.48.a) and up to 2.75 dB in the piezoresisitive measurement (Figure 4.48.b), what has meant an impoverishment up to three times in the Q-factor (817 for two anchors and 2284 for fours anchors) by solely removing two anchors points.

The reason for such an effect was attributed to the addition of vibrations freedom degrees that might ease the excitation of spurious resonance modes (probably torsional [105]) in the structure. The energy that the device employs in these spurious modes does not contribute to the fundamental wine-glass mode that is meant to be excited with this electrodes configuration.
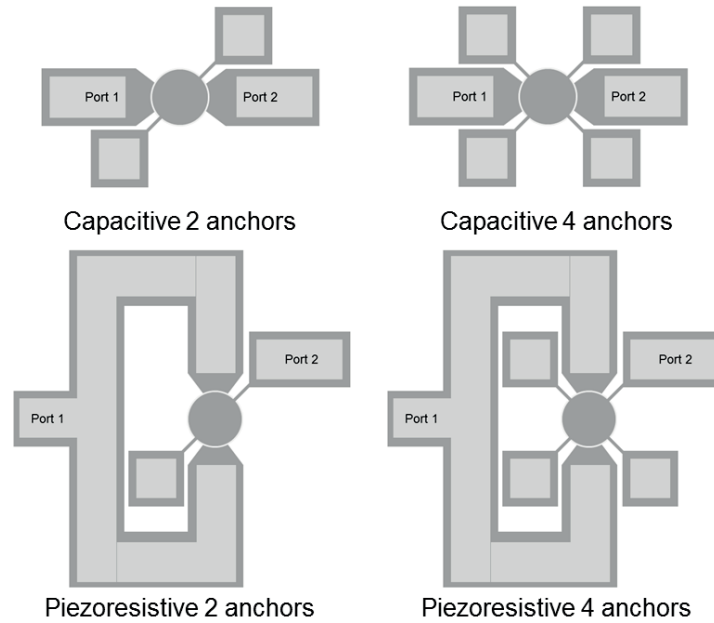
Figure 4.47 – Pad layouts used to study the effect of the anchors damping in a WGD resonator.

(a) Capacitive readout.

(b) Piezoresistive readout.
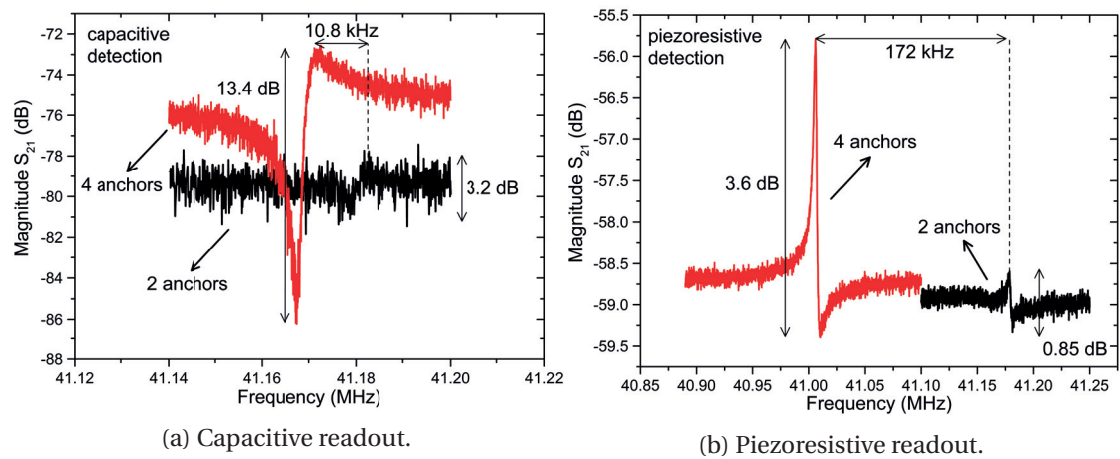
Figure 4.48 – Transmission characteristics for two disk resonators (R = 30 μm, (g_{HfO2} = 20 nm, g_{air} = 80 nm) with 2-4 anchoring points measured by means of (a) capacitive detection and (b) piezoresistive detection.

4.6.5 Probe-to-Electrode Contacts

The noise floor level variation in consequence of bad contact between the metallic characterisation probes and the device pads (which are covered by a thin layer of HfO_2) is depicted in Figure 4.49. The noise floor worsens after each HfO_2 deposition, nevertheless, if the probe-electrode contact if not carefully controlled, the probe scratches of the electrode metal differently with every measurement, and very different noise floor can be achieved.
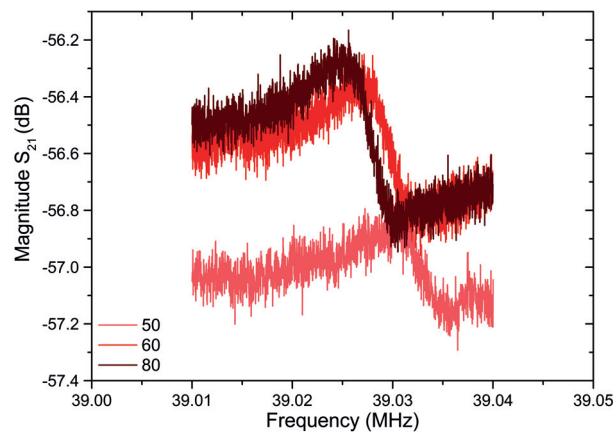
Figure 4.49 – Experimental frequency characteristic for a WGD resonator (R = 30 μm, (g_{HfO2} = 20nm, g_{air} = 80nm) showing the noise floor variations due to a bad contact between the characterisation probes and the device electrodes due to the HfO_2 coating.

4.7 Motional Resistance Calculations

Motional resistance can be estimated by means of two approximations: (1) Equation 3.15 and (2) Equation 3.17. In the first approximation, nominal geometrical values and experimentally acquired f_0 and Q-factors are considered. In the second approximation, $Z_0 = 50\,\Omega$ is considered and the conditions $j\omega C_0 \ll 1/R_m$ and $C_p = 0$ have to be fulfilled.

As in the measurements presented in this work we did not use a de-embedding method [106] [107] [108] in order to minimise the effect of of feedthrough, the condition $j\omega C_0 \ll 1/R_m$ is not always fulfilled. Therefore, motional resistances have been calculated by means of the approximation (1). A complete example is presented in Appendix C.

4.8 Q-factor Extraction

As it is detailed in Sections 4.5 and 4.6, the Q-factors exhibit in some of the devices of this work as lower than expected for silicon MEMS resonators. The proposed solutions for future resonators batches has been the optimization of the fabrication process in order to avoid as much as possible eventual residuals that may be damping the performance.

In addition, as the gap-filling is meant to reduce the motional resistance, a resonator with smaller R_m is loaded more heavily by parasitics interconnect resistance, R_s, than one with large R_m and the extracted Q-factor as shown in Equation 4.1 [30]. Therefore, R_s extraction should be considered.

$$Q_{measured} = Q \frac{R_m}{R_m + R_s} \tag{4.1}$$

To finish, the response in frequency may be distorted by parasitic feedthrough, which leads to poor-quality estimations of Q [109]. As it is proposed in Section 4.7, de-embedding methods should be considered in future characterization [106] [107] [108].

4.9 Summary

In this chapter, the design, fabrication and characterization of a large variety of flexural and bulk mode thin SOI MEMS resonators with are presented: clamped-clamped beams (CCB), double-ended tuning forks (DETF), parallel beam resonators (PBR), wine-glass disks (WGD) and square plate (SP) resonators, covering a range of resonance frequencies from 5 MHz to 70 MHz.

The resonance frequencies acquired experimentally have been compared with the analytical equations presented in Chapter 3 and with the ones extracted from Finite Element Methods (FEM) simulations and they have been demonstrated to fit with variations between 3-18%.

Optical, capacitive and piezoresistive detection methods for MEMS resonators characterization have been validated and compared, revealing that the piezoresistive detection method is the one that offers better performance. The extracted improvement in the quality factor

and the motional resistance has been up to five times better for the piezoresistive detection method (Q = 1107 and R_m = 15.4 kΩ). Resonance frequency tuning with applied DC voltage measurements are provided for each fabricated air-gap resonator, and gap sizing and structure dimensioning effects are studied, accomplishing quality factor of the order 1020, 4247 and 1482 for DETF, PBR and WGD with 100 nm air-gap.

The effect of filling the gaps of the resonator with high-k material ALD of HfO_2) has proven to improve up to 8.8 times the quality factor of a DETF vibrating at 11 MHz and up to 2.2 the quality factor of a WGD vibrating at 11 MHz after a deposition of 5 nm of HfO_2 per gap side. For partially-filled gap resonators with air-gap g_{air} = 90 nm and HfO_2-gap g_{HfO2} = 10 nm, motional resistance have been reduced up to 10 times for a DEFT (from 88.8 kΩ to 8.7 kΩ) and 4 times for a bulk WGD resonator (from 146.3 kΩ to 43.3 kΩ).

Multi-gate excitation combined with piezoresistive detection has proven to enhance the response of a WGD resonator (g_{air} = 90 nm, g_{HfO2} = 10 nm) achieving quality factor 11760 and motional resistance as low as 874 Ω. In the same way, measurements of the response of WGD suspended by 2 and 4 anchors (always in modal nodes) have shown better performance for the 4-anchors case (819) than for the 2-anchors case.

In this chapter, the main contributions are:

- Consistent and accurate comparison between the resonance frequencies obtained by calculations, simulations and measurements.

- Extensive discussion of flexural and bulk MEMS resonators with air-gap in a range from 5 MHz to 70 MHz considering resonance frequency tuning, gap-sizing, structure dimensioning and the effects due to air damping, anchors damping and spring softening over the quality factor and motional parameters.

- Proposed fabrication for flexural and bulk MEMS resonators with partially-filled gaps by means of HfO_2. Improved transmission characteristics in terms of signal robustness, quality factor and motional resistance have been proven after one 5 nm HfO_2 deposition, and the effect of successive deposition in order to partially close the gap have been discussed.

5 Mass Sensing

This chapter presents the state of the art of different MEMS/NEMS resonator applied to mass sensing applications in comparison with the achievements fulfilled in this work. The preliminary study based on FEM simulations that validates MEMS WGD bulk resonators as mass sensors with high point mass sensitivity (up to $796\,kHz \cdot pg^{-1}$) and distributed mass sensitivity (up to $161\,\mu m^2 \cdot ng^{-1}$) is detailed.

Furthermore, an extensive experimental characterization of partially-filled gap MEMS resonators for distributed mass sensing is presented for different modes of resonance as well as different gap-filling thickness of the high-k added material in the gap. MEMS resonators sensitivities of different flexural and bulk resonators vibrating in their in-plane modes of resonance are introduced and compared, being demonstrated that the fabricated DETFs vibrating in flexural mode can achieved mass sensitivities up to $29.52\,kHz \cdot pg^{-1}$ and bulk mode WGDs resonators are more adapted for distributed mass sensing, accomplishing sensitivities up to $5273.5\,kHz \cdot \mu m^2 \cdot pg^{-1}$.

5.1 Introduction to MEMS Resonant Mass Sensors

The actual tendency of decreasing the size of the mechanical resonators into submicron domain is very promising for the development of mass sensing applications due to their exceptionaly minuscule dimensions, which makes them ultrasensitive. They also offer foundry compatible microfabrication processes and Integrated Circuit (IC) compatibility. They have been used in applications such as nanostructured or biological thin films characterization [110], gas detection or microscaled physical processes monitoring [111] [112] able to reach extremely low mass resolutions in air and at room temperature [113].

MEMS resonant mass sensors operate on the basis of the resonance frequency downshift of a structure before and after the attachment of a target entity, where the shift in the resonant frequency can be used to calculate the added mass [111]. These miniaturized resonators can be batch-fabricated as individual devices or arrays at a very low cost. Thanks to their small size, they can provide orders of magnitude higher mass sensitivity and resolution compared to bulky quartz, SAW of FBARS resonators [114].

Most of recent microelectromechanical (MEMS) resonators used for sensory application use capacitive (see Table 5.1) [115] [116] [113] or piezoelectric [117] electromechanical transduction. As it can seen in Table 5.1, micromechanical mass sensors profit from large actuation areas (up to orders of $10^5 - 10^6$ μm^2 [118] [116]) in order to maximize the detection area, however by increasing resonators dimensions, the obtained resonance frequency decreases and mass sensitivity is limited in the order of kHz per pg. The mass sensitivities that have been obtained for the MEMS resontors presented in this work are in the order of k$Hz \cdot pg^{-1}$, what is in the state-of-the-art or beyond of some others proposed works [116] [118].

Nevertheless, as the limits of detection benefits from size reduction, this has motivated the fabrication of nanoelectromechanical (NEMS) resonators made of molecular materials such as Carbon Nanotubes (CNT) [119] [120] or silicon nanocantilevers [121] [122]. NEMS resonators are applied in mass spectrometry with sensitivities in the range of up to few kDa [123]. In this cases, optical detection is used to track changes in the resonance frequency [121] [122], but often more complex actuation techniques are required. In [120] the actuation is carried out by applying an RF signal to the CNT and detection the field emission. Frequency

Modulation is used in [119] by applying a current in the CNT modulated by the side gate and detection the changes in frequency. Regardless their ultrahigh sensitivity, NEMS resonators normally demand costly fabrication processes and require vacuum operation to mitigate the air damping effect, therefore, the optimization of mass sensitivities in MEMS resonators are a promising field for devices oriented to the customer market in applications such a dust or alergens detection, among others.

5.2 Motivation

A resonant MEMS mass sensor is a transducer that produces a frequency response when added mass changes the equilibrium state of the transducer. The resulting signal is used to make appropriate determination to the change of mass on the transducer. When a MEMS device becomes a physical transducer, it can be used directly to sense a load in a label-free environment. Nevertheless, for targeted detection, a receptor layer is strategically functionalized in a way that measurable output signals can be produced in response to specific stimuli.

The resonators in this work are proposed for future environmental mass sensing (air quality), eventually taking advantage from the connection of a large number of them and the addition of their output together in order to improve the detected signal [105] [19] [129] [130].

5.3 Figures-of-Merit (FOM)

In general, resonant mass sensing is performed by carefully determining the resonance frequency, f_0, of the resonator and then, by looking for the frequency shift, δf due to the accreted mass. Assuming that this added mass, δm is a fraction of the effective vibratory mass, m_{eff}, the relation between the frequency shift and the added mass can be expressed by:

$$f_0 + \delta f = \frac{1}{2\pi} \sqrt{\frac{k_{eff}}{m_{eff} + \delta m}} \tag{5.1}$$
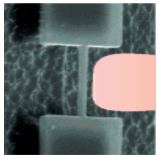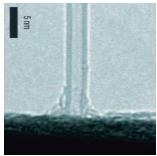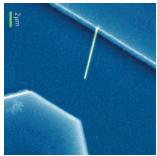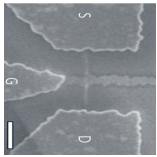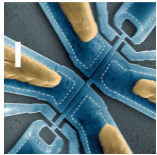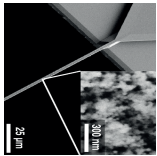
Table 5.1 – Recent Microelectromechanical Resonators for Mass Sensing Applications.

	Cagliani 2011 [113]	He 2013 [124]	McNeil 2013 [125]	Peiner 2013 [118]	Liu 2013 [126]	Zarifi 2016 [116]	This work	This work	This work	This work
Device										
Material	PolySi	PolySi	Si/PZT	Si on piezoact.	SiO_2	Si	Si	Si	Si	Si
Target	Pt/C/Ga Composite	Humidity	Au	Carbon Particles	SiO_2 Particles	Au	HfO_2 layers	HfO_2 layers	HfO_2 layers	HfO_2 layers
Type	Disk	Disk	Membrane	F-C	Toroid	Disk	CCB	DETF	PBR	WGD
Actuation	Capacitive	PMM[a]	Piezoel.	Piezoel.	Optical	Capacitive	Capacitive	Capacitive	Capacitive	Capacitive
Readout	Capacitive	Capacitive	Optical	Piezores.	Optical	Capacitive	Capacitive	Capacitive	Capacitive	Piezores.
Area (μm^2)	-	2827	11310	$1.4 \cdot 10^5$	1590	$1.4 \cdot 10^6$	280	294	10450	2650
Sensitivity	$\frac{3.75 kHz}{pg}$ (PMS) $\frac{5.4 kHz}{pg}$ (DMS)	$70 kHz$ (DMS)[b]	$\frac{0.012 kHz}{pg}$ (DMS)	$\frac{10^{-5} kHz}{pg}$ (DMS)	$\frac{0.4 kHz}{pg}$ (DMS)	$\frac{2.27 kHz}{pg}$	$\frac{2.517 kHz}{pg}$ (EMS) $\frac{15.81 kHz}{pg}$ (PMS) $\frac{704.76 kHz \cdot \mu m^2}{pg}$ (DMS)	$\frac{4.816 kHz}{pg}$ (EMS) $\frac{29.52 kHz}{pg}$ (PMS) $\frac{1415.91 kHz \cdot \mu m^2}{pg}$ (DMS)	$\frac{0.326 kHz}{pg}$ (EMS) $\frac{0.67 kHz}{pg}$ (PMS) $\frac{3406.7 kHz \cdot \mu m^2}{pg}$ (DMS)	$\frac{1.99 kHz}{pg}$ (EMS) $\frac{10.69 kHz}{pg}$ (PMS) $\frac{5273.5 kHz \cdot \mu m^2}{pg}$ (DMS)

[a]Pulse Mode Mechanism
[b]Humidity changes from 0% to 80%

Table 5.2 – Recent Nanoelectromechanical Resonators for Mass Sensing Applications.

Device	Roukes 2006 [122]	Zettl 2008 [120]	Craighead 2010 [127]	Tamayo 2010 [121]	Bachtold 2012 [119]	Roukes 2012 [123]	Boisen 2013 [128]
Material	SiC	CNT	PolySi	Si	CNT	Si	Si_3N_4
Target	Xe Atoms	Au Atoms	Liquids	Carbon Layer	$C_{10}H_8$	Au Part.	Au Part.
Type	CCB	CCB	CCB	CCB	FCB	CCB	FCB
Actuation	PLL[a]	RF Signal	Optical	Optical	FM[b]	Capacitive	Coupled Circuit
Readout	PLL	Field Emission	Optical	Optical	FM	Piezoresistive	Coupled Circuit
Sensitivity ($\frac{Hz}{g}$) ($\frac{1Hz}{zg}$)	zg		$\frac{100Hz}{fg}$	zg	$\frac{320kHz}{yg}$	$500kDa$	$\frac{1.1MHz}{6fg}$

[a]phase Lock Loop
[b]Frequency Modulated

If δm « m_{eff}, expanding in series the expression can be linearized as:

$$\delta f \approx -\frac{f_0}{2m_{eff}}\delta m \tag{5.2}$$

This expression assumes that the modal Q-factor and stiffnedd are not appreciably affected by the accreted species [131]. Therefore it can be determined that:

$$\delta m = -2\frac{m_{eff}}{f_0}\delta f \tag{5.3}$$

Hereafter, δm can be referred as the minimum detectable mass of the system and δf as the minimum measurable frequency shift.

Taking into account Equations 5.1, 5.2 and 5.3, two major FOMs for MEMS resonators refer the sensitivity calculated by means of a resonance frequency shift caused by the attachment of single particles on the resonator surface (point mass sensitivity) and the one extracted by considering a distribution of mass on its surface (distributed mass sensitivity).

Point Mass Sensitivity

When the added mass is much smaller than the effective mass of the resonator, the maximum point mass sensitivity (PMS) of a resonant mass sensor (or point mass resolution, PMR) is theoretically estimated by Equation 5.4 [113]. The PMR gives a measure how the minimum mass that the device can potentially detect, expressed in $Hz \cdot g^{-1}$.

$$S = \frac{f_0}{2m_{eff}} \tag{5.4}$$

where f_0 is the resonance frequency and m_{eff} is the effective mass of the device.

As observed in Equation 5.4 to be able to achieve the highest possible sensitivity, an extremely tiny beam needs to be considered in the design. This however makes the sensor more susceptible to external perturbations caused by the environment, thus demanding operation under ultra-high vacuum. Therefore, MEMS bulk mode plate sensors have become an alternative to overcome the limitations imposed by M/NEMS beam resonant technology.

Distributed Mass Sensitivity

The distributed mass sensitivity (DMS) has to be considered when a large part of the sensor surface is involved in capturing the target and the quantity under investigation is proportional to the amount of mass per surface unit [95]. It measures the minimum mass that can be detected per square meter of sensing surface, expressed in $Hz \cdot m^2 \cdot g^{-1}$ (or distributed mass resolution, DMR) [113]. As we can see in Equation 5.5, the DMR is calculated by taking into account the effective mass of the resonator, which considers the resonator mass when it is vibrating.

$$S = \frac{f_0 A_{eff}}{2 m_{eff}} \tag{5.5}$$

where $A_{eff} = \frac{m_{eff}}{\rho t}$ is the effective area of the device, ρ is the material density and t is the device thickness. The effective mass takes into account the dependence of the sensitivity on the mode shape, cause the contribution to the frequency shift from the added mass depends on where it is located on the resonator surface.

5.4 Finite Elements Method (FEM) Model

The present section is focused on the micromechanical Finite Elements Methods (FEM) analysis of wine-glass disk (WGD) resonators to study the benefits of air and partially-filled gaps regarding to resonance frequency, motional resistance, Q-factor and point and distributed mass sensitivity.

Figure 5.1 shows the perspective schematic for the resonator: a solid disk with radius R, thickness t, anchor length l_a, anchor width w_a and gap g. The gates surround the gaps, (in blue) and excite the disk by means of a harmonic perturbation. Aside from the variants that are specified later, the typical dimensions considered in this section are: R = 5 μm, t = 1 μm, g = 50 nm, l_a = 1 μm and w_a = 750 nm, and four anchors have been simulated.

In order to excite the WGD resonator (Figure 5.2, left), the actuation electrodes (preferentially two or four as it is discussed in Section 4.6.4) are designed as it is depicted in Figure 5.2 (right) and the resulting shape mode of resonance (wine-glass) can be seen in Figure 5.2 (left).
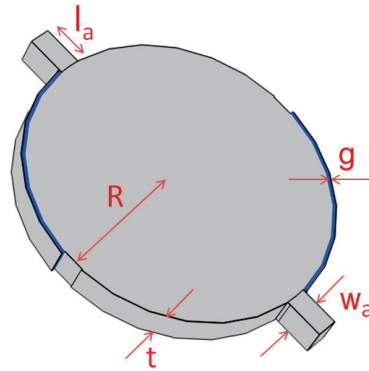
Figure 5.1 – Perspective schematic of the simulated micromechanical wine-glass mode disk resonator.
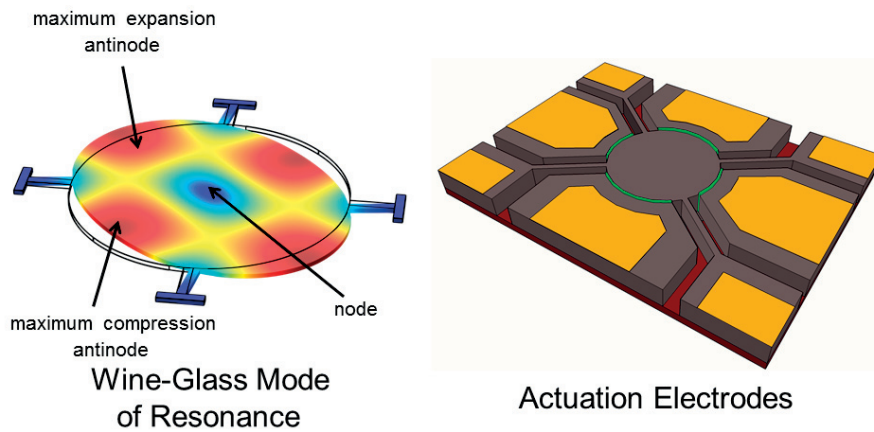
Figure 5.2 – (Left) WG-mode of the disk resonator: minimum displacement points (nodes, in blue) and minimum displacement points (antinodes, in red). (Right) Actuation electrodes surrounding the disk resonator to excite the mode.

5.4.1 Point Mass Detection

Particles sitting on different locations of the thermal actuator beams will have different effects on the resonance frequency of the structure due to different vibration amplitudes and therefore different effective stiffness and effective resonator mass at different locations [114]. In order to evaluate this effect, platinum particles of 1 μm^3 were simulated to attach on the surface of a WGD (t = 2μm, R = 10 μm and g = 200 nm) with Si_3N_4 solid-gap resonating at 189 MHz to obtain the frequency shifts and the simulated point mass sensitivity. Si_3N_4 as conforming material of the solid gap was chosen in accordance with the good performance exhibited in literature [31] [44] and the medium motional resistance proven in Figure 3.8. MEMS resonators

based on solid-gaps transduction have been proposed for mass sensing applications in order to prevent devices stiction due to the eventual attachment of particles inside of the gap.

Taking into consideration the mode shape shown in Figure 5.2 (left), several deposition cases have been considered in order to analytically compare the sensitivity of the WGD depending on the area where the particles attach (see Figure 5.3). In case 1 the particle is deposited on a resonance node with minimum displacement; in cases 2-3 the particle is attached to a resonance antinode, (maximum displacement) considering the cases of maximum compression (case 2) and expansion (case 3) of the resonance shape; in case 4 it has been proven that deposition in the node of resonance does not substantially contribute to the frequency downshift by simulating two attached particles on top of the resonators, one in a resonance antinode and the other one to the resonance node; in cases 5-9 particles have been added sequentially in order to approximate a distributed mass deposition, attaining mass sensitivities up to 796 kHz$\cdot pg^{-1}$.
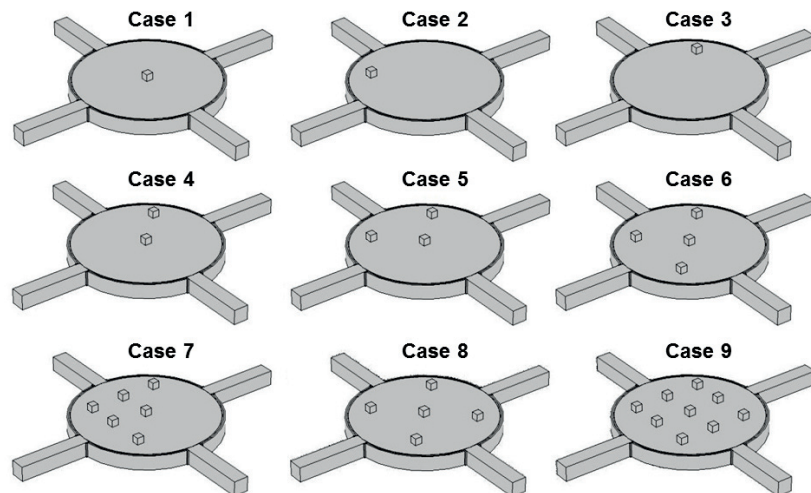
Figure 5.3 – Deposition cases for the Pt particles used to calculate the point mass sensitivity: (1) on resonance node; (2-3) on a resonance antinode; (4) on both resonance and antiresonance nodes and (5-9) distributed particles.

The extracted sensitivity has has been proven to barely change from deposition on the maximum compression to the maximum extension antinodes of resonance (see inset of Figure 5.4. Single particle deposition on a resonance node (case 4) addresses frequency shifts around 5 kHz/pg, revealing that future implementations of bulk resonators have to take into considera-

tion antiresonance nodes areas. To further increase the precision of measurements one can add a shadowing stationary surface [114].
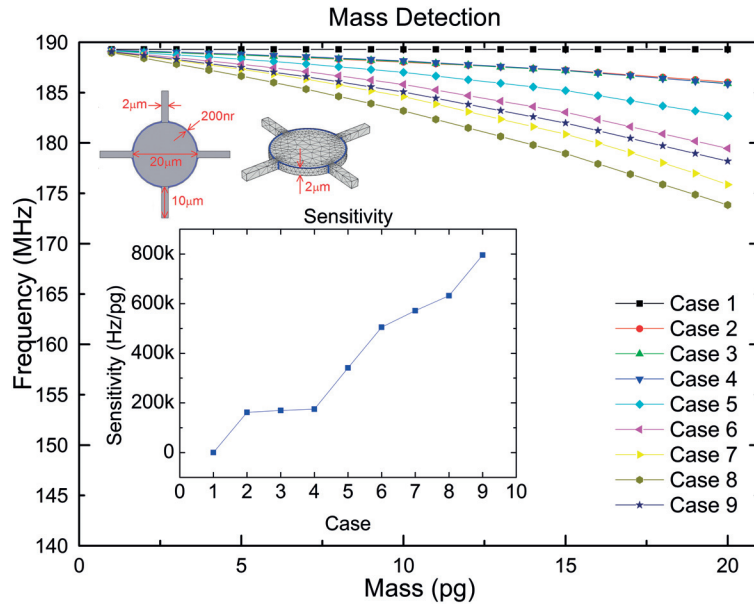
Figure 5.4 – Modal FEM simulations of the resonance frequency shifts and mass sensitivity for different deposited Pt particles distributions onto a disk. The inset shows the averaged mass loading calculated after each added particle. Cases: (1-3) 1 particle; (4) 2 particles; (5) 3 particles; (6) 4 particles; (7) 6 particles; (8) 5 particles and (9) 9 particles.

Figure 5.5 shows the additional resonant frequency downshifting effect due to variations in the particle-disk contact area that have been simulated (particle on an antinode). Mass sensitivity approximately increases by a factor of 1.6 times when the contact area between the disk and a deposited Pt particle increases by a factor of 16.

In Figure 5.6 an interesting FOM has been included. In green, the resonant frequency shifts regarding to a Pt particle deposited onto an antinode are included, with a mass that varies from 1 fg to 20 pg. Frequency shifts up to 2 times those of the 189 MHz are achieved by means of the smallest disk at 394 MHz. Nevertheless, the smallest disk stops being sensitive for particles heavier than 3 pg while the disk at 189 MHz keeps on resonance for particles up to 20 pg. This effect is a consequence of the disk-particle mass ratio: the larger the ratio, the smaller the frequency shift and the faster the disk vibrations are attenuated. Therefore, FEM simulations have been proven to be an excellent method to approximate the maximum resonator-specimen mass ratio range.
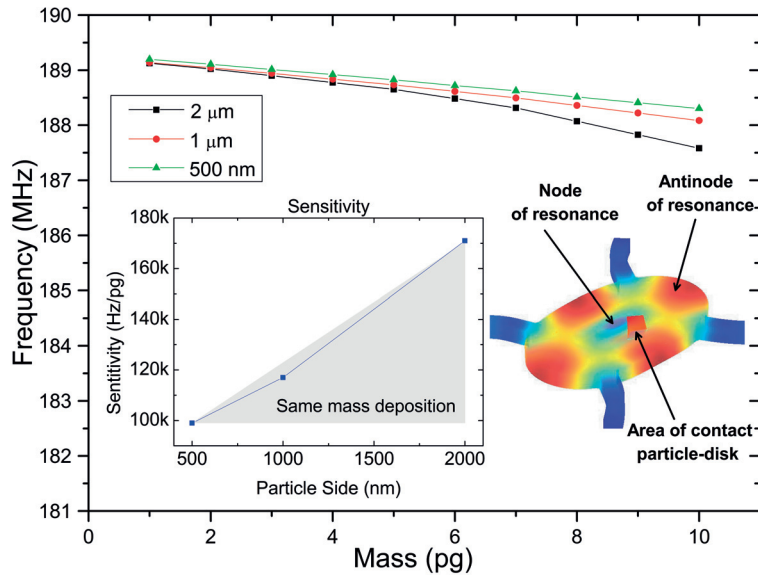
Figure 5.5 – FEM simulations for the resonance frequency shifts considering different particle-disk contact areas with the same mass. The shape of the wine-glass mode of resonance is included on the right for a sketched disk resonator.
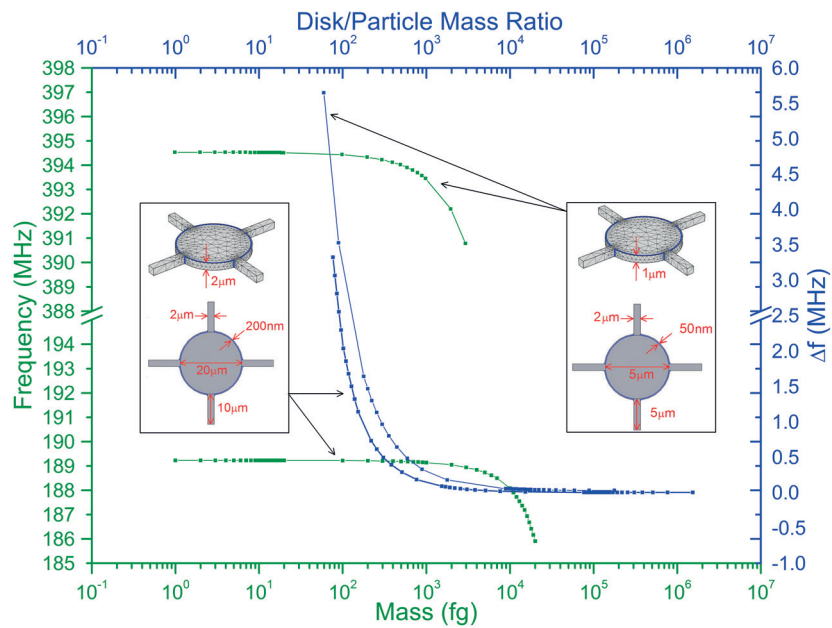
Figure 5.6 – Modal FEM simulations of the frequency shifts considering a mass deposited onto an antinode of resonance of disks resonating at 189 and 394 MHz and their respective disk-particle mass ratio relationship.

5.4.2 Distributed Mass Detection

In order to simulate biomass sensing by virtue of FEM analysis, uniform layers of 10 nm-thickness of a typical antibody such a goat IgG have been attached onto the disk resonator [132]. The resonance frequency variation after every deposited layer of IgG is depicted in Figure 5.7.
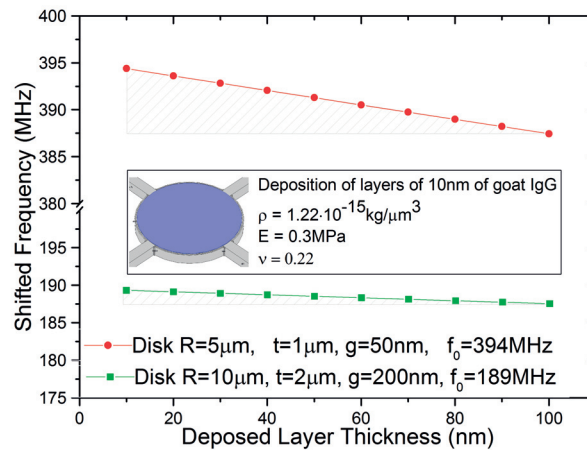
Figure 5.7 – Modal FEM simulations of the frequency shifts considering uniform layers of biomass deposited onto the disk.

The frequency downshifting achieved by the smallest disk resonating at 394 MHz is four times larger than the one of the WGD vibrating at 189 MHz. The distributed mass sensitivity is defined in Equation 5.5. The achieved distributed mass sensitivity is of 161 $\mu m^2 ng^{-1}$ for the WGD vibrating at 394 MHz and 86 $\mu m^2 ng^{-1}$ for the disk vibrating at 189 MHz, so while disks are kept in resonance as it has been discussed above, smaller and higher frequency disks are more suitable to be implemented as mass and/or biomass sensors.

5.5 Mass Sensing Experiment

As it has been detailed in Chapter 4, the performance in terms of quality factor and motional resistance of the fabricated air-gap MEMS resonators has been improved by filling the gap with a high-k material. In case of the present work the chosen material has been HfO$_2$ due to its high dielectric constant ($\epsilon_r \sim 19$) and its availability in the cleanroom facilities. In addition

to this performance enhancement, the mass load effect produced by the added HfO_2 layers provides an effective way to calculate the distributed mass sensitivity in the covered devices.

In mass sensors, the additional mass is meant to attach on one surface of the device, normally the top one. On the contrary, in the devices that have been covered by means of an ALD method, all the exposed surfaces are conformally covered by an homogeneous layer of HfO_2. In order to extract the distributed mass sensitivities for the top surface of each of the fabricated devices and therefore being able of comparing their point and distributed mass sensitivities for the flexural and bulk resonators, the total frequency downshift and mass loading after each HfO_2 deposition have been extracted. The ratio between the total resonance frequency shift and the total added mass gives an straightforward measure of the mass sensitivity on the top surface of each device. The devices that have been studied for mass sensing are detailed in Chapter 4. They are sketched in the schematic of Figure 5.8 and their dimensions listed in Table 5.3.
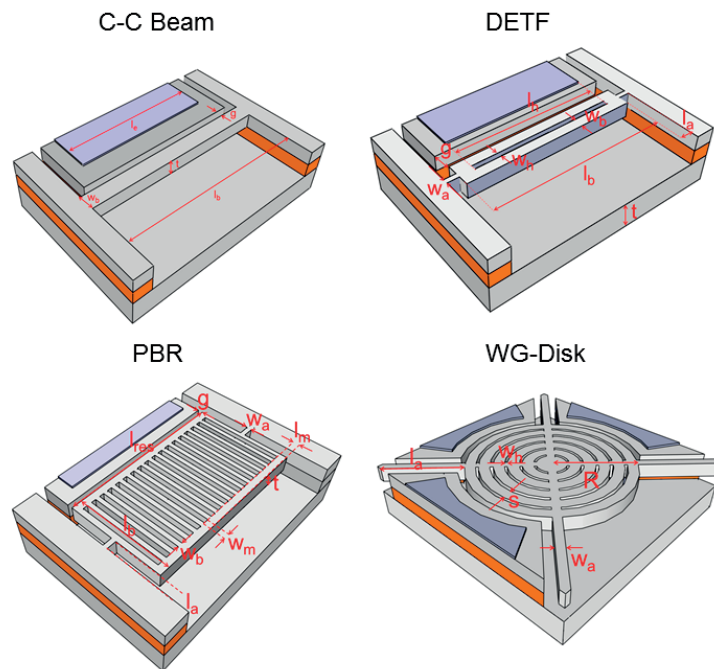
Figure 5.8 – Geometries of the flexural and bulk resonators considered in this section.

The effect of the additional mass coming from the HfO_2 makes that the resonance frequency shifts are larger in those devices that have more sidewalls. As it can be observed in Figure 5.9, PBR and WGD resonators have more conformally covered area due to (a) their larger dimen-

Table 5.3 – Dimensions of the MEMS resonators considered for mass sensing applications ($t = 1\mu$m).

Parameter	CCB g = 300 nm	CCB g = 500 nm	DETF g = 300 nm	PBR (N = 12) g = 100 nm	WGD g = 100 nm
V_{DC1}, (V)	30	80	50	70	50
V_{DC2}, (V)	30	80	50	70	1
$l_b / l_p / R (\mu m)$	70	70	40	151	30
$w_b / s (\mu m)$	4	4	3	5	5
$w_h / w_m (\mu m)$	-	-	-	2	1
$l_m (\mu m)$	-	-	-	2	1
$l_a (\mu m)$	-	-	6	7	9.8
$w_a (\mu m)$	-	-	3	3	2.5

sions and (b) the etch holes carried out to release the resonators. Hence this effect will obscure the mass sensitivity study, an analysis from the HfO$_2$ mass deposited after each ALD step for the devices is displayed in Figure 5.10, highlighting the need of extract on-top surface mass sensitivities for a better comparison.
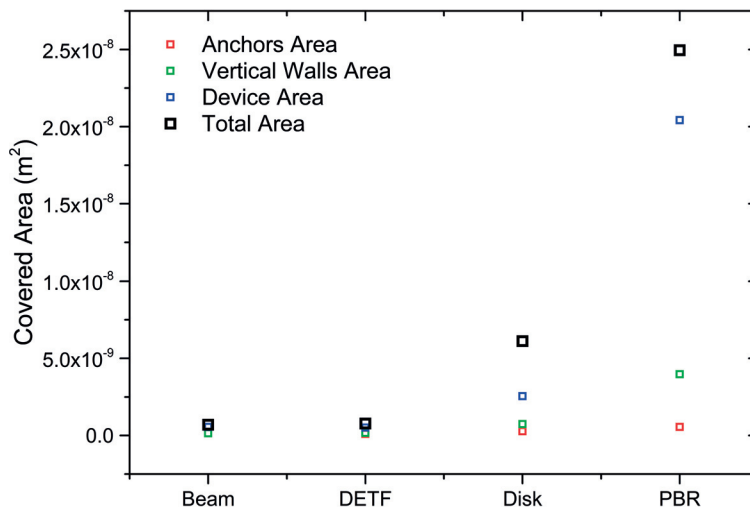
Figure 5.9 – Comparison of the total area (top, bottom, anchors and sidewalls) covered by conformal ALD HfO$_2$ in each of the studied MEMS resonators: (red) anchors surfaces; (green) vertical surfaces (considering releasing holes); (blue) horizontal surfaces of the resonators bodies and (black) total area covered by ALD HfO$_2$.

Each of the devices included in Table 5.3 is analysed and compared in the following sections. A final comparison of the experimental mass sensitivities (PMS and DMS) is included in Section 5.5.5.
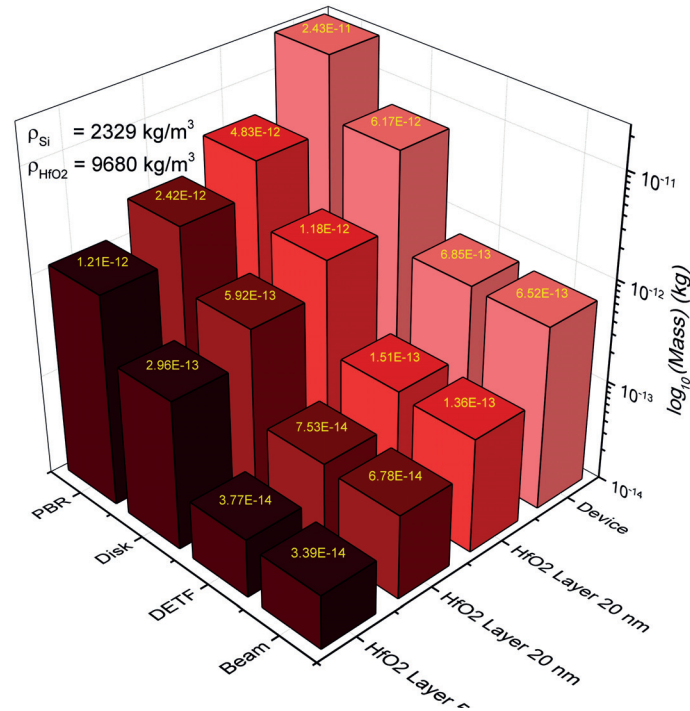
Figure 5.10 – Comparison of the devices mass and the added mass after each ALD HfO$_2$ deposition. The considered materials densities for silicon and hafnium dioxide are ρ_{Si} = 2329 kg·m^{-3} and ρ_{HfO2} = 9680 kg·m^{-3}, respectively.

5.5.1 Clamped-Clamped Beam (CCB) Resonator

The resonance frequency shifts for two CCB (see Table 5.3) at different gap-filling and hence different added mass have been measured through the capacitive detection method detailed in Section 3.2.3 and they are shown in Figure 5.11. The extraction of the resonance frequencies have been done starting by air-gaps of 300 and 500 nm, and partially filling each sidewall of the gaps with 5 nm, 10 nm and 20 nm ALD layers of HfO$_2$. It can be seen that the linear slopes are similar for both devices, nevertheless the CCB with an initial air-gap of g = 300 nm performs better in terms of supplied bias (V_{DC1} = V_{DC2} = 30V).

In order to compare the effect of the total added mass and resonance frequency shifts in comparison with the ones calculated for a conformal HfO$_2$ layer on the top surface (top surface area A_{CCB} = 280 μm^2), Figure 5.12 can be studied. The resonance frequency shifts are evidently much larger if total HfO$_2$ added mass is considered. From the averaged resonance frequency shift value after each deposition, experimental mass sensitivities of 2.52 kHz·pg^{-1}
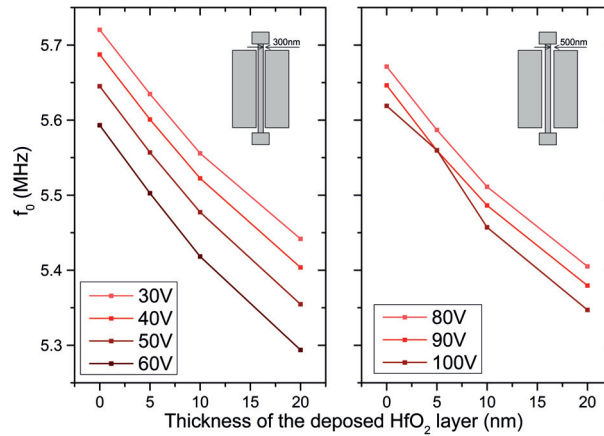
Figure 5.11 – Resonance frequency, f_0, versus the thickness before and after ALD HfO$_2$ deposition per sidewall (5, 10 and 20 nm) for two CCB resonators of (left) 300 nm and (right) 500 nm original air-gap vibrating at their fundamental flexural mode of resonance for different applied bias.

and 2.49 kHz$\cdot pg^{-1}$ are extracted for the initial 300 nm and 500 nm air-gap CCB resonators.
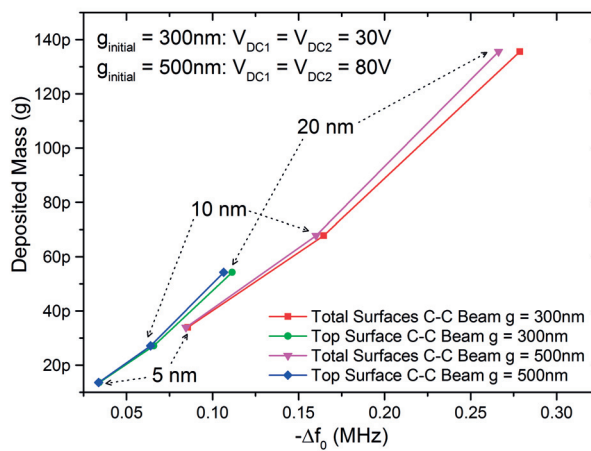
Figure 5.12 – Measurements of the extracted distributed mass deposited versus the resonance frequency shifts.

As it is studied in Chapter 4, the devices performance have been boosted by virtue of the gap-filling (quality factor increases and motional resistance decreases). In order to extract the experimental sensitivity values, frequency resonance shifts and added mass on top of the resonator are listed in Table 5.4. Quality factors have been calculated by means of the phase-slope approximation discussed in Appendix A [54] and are shown to keep the trend that

has been discussed in Chapter 4: after the first HfO_2 deposition, it increases, to get worse after the second and third deposition, but always similar than the quality factor extracted with the air-gap device, in contradiction with other partially-filled resonators, whose Q decreases by filling the gap [30].

Table 5.4 – Extracted frequency shifts after the accumulated added mass (on top) coming from each HfO_2 deposition for a CCB ($V_{DC1} = V_{DC2} = 30V$).

Parameter	$g_{air} = 300$ nm	$g_{air} = 290$ nm $g_{HfO2} = 10$ nm	$g_{air} = 280$ nm $g_{HfO2} = 20$ nm	$g_{air} = 260$ nm $g_{HfO2} = 40$ nm
f_0, (MHz)	5.7203	5.6347	5.5557	5.4416
Layer thickness, (nm)	0	5	10	20
Added mass, pg	0	13.6	27.1	54.2

5.5.2 Double-Ended Tuning Fork (DETF) Resonator

Similar capacitive measurements to the ones performed above have been done for a DETF whose dimensions are included in Table 5.3. In this case, the additional area concerning the top surfaces of the two anchors of the DETF have been included as sensing area of the resonator $A_{DETF} = 294 \ \mu m^2$). Here, averaged resonance frequency shifts up to 180 kHz have been detected after each HfO_2 layer deposition of 5 nm-thick with an applied bias voltage $V_{DC1} = V_{DC2} = 50V$, and a mass sensitivity of 4.82 kHz·pg^1 has been extracted from Figure 5.13 after neglecting the added mass that is not on the device surface.

These results highlight two effects: (a) devices with similar geometries (CCBs and DETFs are composed by strings) vibrating at similar modes of resonance (flexural-lateral) and with dimensions in an analogous range, the one that exhibits higher resonance frequency have better sensitivity (Section 5.4.1) and (b) mass loading on the anchors surfaces have to be considered in distributed mass calculations because they are a vibrating part of the resonator.

Table 5.5 – Extracted frequency shifts after the accumulated added mass (on top) coming from each HfO_2 deposition for a DETF, ($V_{DC1} = V_{DC2} = 50V$).

Parameter	$g_{air} = 300$ nm	$g_{air} = 290$ nm $g_{HfO2} = 10$ nm	$g_{air} = 280$ nm $g_{HfO2} = 20$ nm	$g_{air} = 260$ nm $g_{HfO2} = 40$ nm
f_0, (MHz)	11.1	10.9191	10.7508	10.4816
Layer thickness, (nm)	0	5	10	20
Added mass, (pg)	0	14.2	28.5	56.9
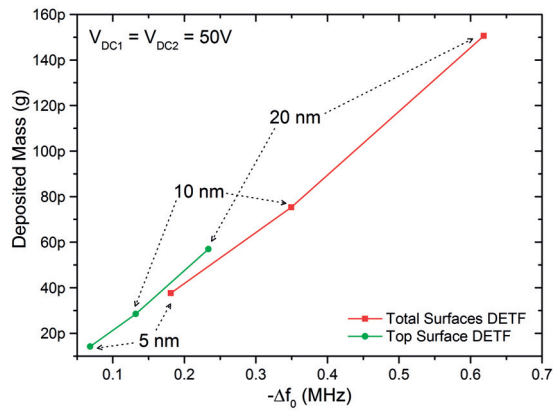
Figure 5.13 – Resonance frequency, f_0, shifts of 300 nm-gap DETF after HfO_2 ALD depositions.

5.5.3 Parallel Beam Resonator

As the top surface area of the measured PBR is $A_{PBR} = 10200 \ \mu m^2$. Mass sensitivity has been extracted by means of the same procedure than in precedent sections, and it is $0.33 \ kHz \cdot pg^{-1}$ from the resonance frequency shifts after each ALD deposition shown in Figure 5.14 and Table 5.6.
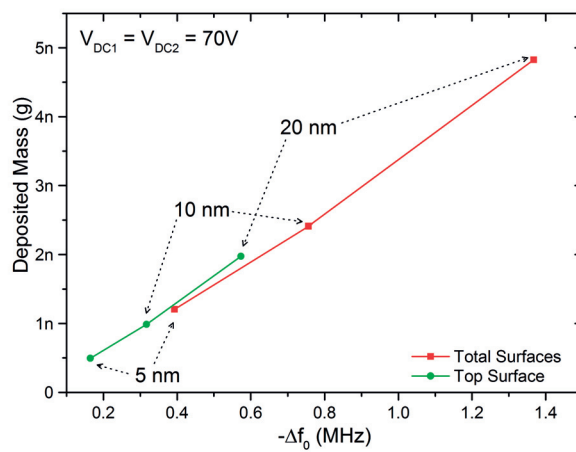
Figure 5.14 – Resonance frequency, f_0, shifts of 100 nm-gap PBR after HfO_2 ALD depositions.

Table 5.6 – Extracted accumulated on top HfO_2 added mass resonance frequency of the PBR for each deposition, ($V_{DC1} = V_{DC2} = 70$ V).

Parameter	g_{air} = 100 nm	g_{air} = 90 nm g_{HfO2} = 10 nm	g_{air} = 80 nm g_{HfO2} = 20 nm	g_{air} = 60 nm g_{HfO2} = 40 nm
f_0, (MHz)	23.5973	23.2040	22.8412	22.2298
Layer thickness, (nm)	0	5	10	20
Added mass, (pg)	0	506	1010	2020

5.5.4   Wine-Glass Disk Resonator

The transmission characteristics of the WGD resonator described in Table 5.3 have been extracted by virtue of the piezoresistive detection described in Section 3.2.4 with $V_{DC1} = 50$ V and $V_{DC1} = 1$ V.

By taking into consideration its surface area $A_{WGD} = 2550 \ \mu m^2$, the extracted mass sensitivity is 1.99 kHz·pg^{-1} (see Table 5.7). In this case, low quality factors have been extracted. In order to improve them, a higher bias voltage could be applied [103], with the advantage of having less motional resistance (see Equation 3.15), but more power consumption.
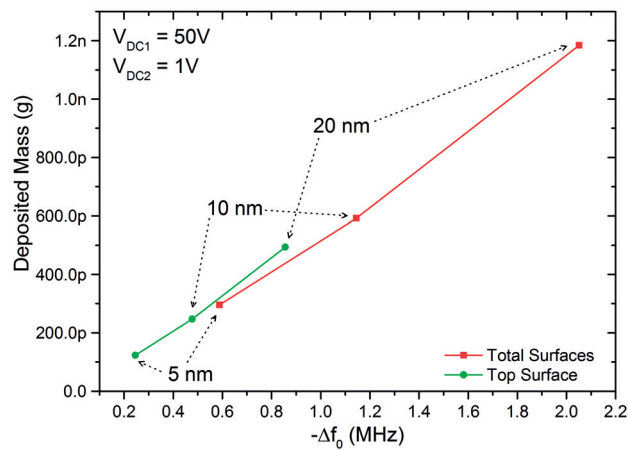
Figure 5.15 – Resonance frequency, f_0, shifts of 100 nm-gap WGD after HfO_2 ALD depositions.

5.5.5   Mass Sensing Comparison

Theoretical mass resolutions (PMR and DMR) have been calculated by means of Equations 5.4 and 5.5 with the resonance frequencies before HfO_2 depositions. The conditions considered

Table 5.7 – Extracted frequency shifts after the accumulated added mass (on top) coming from each HfO_2 deposition for a WGD, (V_{DC1} = 50 V, V_{DC1} = 1 V).

Parameter	g_{air} = 100 nm	g_{air} = 90 nm g_{HfO2} = 10 nm	g_{air} = 80 nm g_{HfO2} = 20 nm	g_{air} = 60 nm g_{HfO2} = 40 nm
f_0, (MHz)	41.0816	40.4931	39.937	39.0298
Layer thickness, (nm)	0	5	10	20
Added mass, (pg)	0	128	256	513

for the extraction of the experimental mass sensitivities have been [133]:

- Experimental mass sensitivities have been calculated from the averaged frequency shift after each 5 nm deposition of HfO_2. The masses loaded have been considered as the HfO_2 mass on top of the devices after each deposition. These two parameters can be related in the experimental mass sensitivity as:

$$EMS = \frac{\Delta f_0}{m_{load}} \tag{5.6}$$

where Δf_0 is the averaged resonance frequency shift and m_{load} is the additional mass deposited on top of the device, both after each 5 nm HfO_2 deposition.

- Experimental distributed mass sensitivity (EDMS) has been calculated by taking into consideration the effective area of the devices:

$$EDMS = \frac{\Delta f_0}{\frac{m_{load}}{A_{total}}} = A_{total} \cdot \frac{\Delta f_0}{m_{load}} \tag{5.7}$$

where A_{total} is the on-top covered area.

- Experimental point mass sensitivity (EPMS) has been extracted from EDMS by means of the relation between Equations 5.4 and 5.5 as [134]:

$$EPMS = \frac{EDMS}{A_{eff}} \tag{5.8}$$

As it is shown in Section 5.4.1, in a vibrating structure the effective mass varies with time and with respect to the spatial locations of the device depending on the modal shape of the resonator. Due to this fact, the contribution to the frequency shift from the added mass

depends on where the mass is located on the resonator surface. When the mass is deposited in an antinode, (maximum displacement points of the resonator that compound the effective area) the expected sensitivity is larger than when a particle is deposited in a node (minimum displacement points of the resonator).

By taking into consideration the effective mass, the effect of the mode shape is taken into account into the sensitivity calculations. The relation between the device mass and effective mass for the fabricated devices has been plotted in Figure 5.16. Here, we can see the ratios between deposited layer and device real and effective mass, that are larger for the flexural devices (CCB and DETF) as it was expected. The other parameters that have been used for the analysis are listed in Table 5.8.
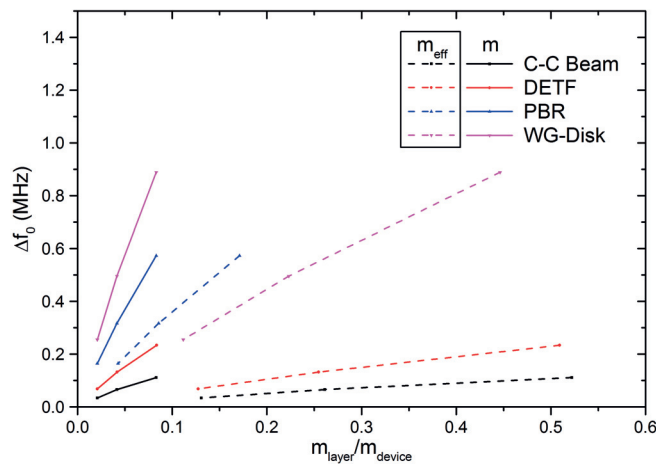
Figure 5.16 – Comparison between the mass of the HfO_2 layer that have been deposited and the inertial (solid lines) and effective (dashed lines) mass of the resonators.

The resulting experimental sensitivities (EMS, EPMS, EDMS) are included in Table 5.9. By comparing them with the theoretical PMS and DMS, we can see that the device that gets closer to the theoretical PMS and DMS predictions is the PBR, with an agreement around 68%. This result may come from a more accurate approximation of the effective mass used during the sensitivities calculations (see Equation 3.43).

The devices that have better mass sensitivities are the DETF with a PMS of 29.52 kHz$\cdot pg^{-1}$ and the WGD, which accomplishes a DMS of 5273.5 kHz$\cdot \mu m^2 \cdot pg^{-1}$. As it was expected, flexural

Table 5.8 – Characteristic parameters for the fabricated mass sensing MEMS resonators (t = 1 μm).

Parameter	CCB	DETF	PBR (N = 12)	WGD
	g = 300 nm	g = 300 nm	g = 100 nm	g = 100 nm
f_0, (MHz)	5.72 (30V)	11.1 (50V)	23.6 (70V)	41.08 (50V)
Total Covered Area (μm^2)	700	778	24930	6110
Top Covered Area (μm^2)	280	294	10450	2650
Effective Area, A_{eff} (μm^2)	44.57	47.96	5079	493
Device Mass m, (ng)	0.66	0.63	24.34	6.17
Effective Mass, m_{eff}, (ng)	0.11	0.11	11.83	1.15
Top Deposited Mass, (pg)	13.6	14.2	506	128

devices, which have smaller device-sample mass ratios (see Figure 5.16), are more sensitive to punctual mass loading, however, bulk devices, which have larger effective areas, offer better DMS.

Table 5.9 – Dimensions of the MEMS resonators considered for mass sensing applications ($t = 1\mu m$).

Parameter	CCB	DETF	PBR (N = 12)	WGD
	g = 300nm	g = 300nm	g = 100nm	g = 100nm
f_0, (MHz)	5.72 (30V)	11.1 (50V)	23.6 (70V)	41.08 (50V)
EMS kHz·pg^{-1}	2.517	4.816	0.326	1.99
Theo. PMS kHz·pg^{-1}	27.55	49.69	0.99	17.88
EPMS kHz·pg^{-1}	15.81	29.52	0.67	10.69
Theo. DMS kHz·$\mu m^2 \cdot pg^{-1}$	1227.99	2382.99	5066.55	8819.24
EDMS kHz·$\mu m^2 \cdot pg^{-1}$	704.76	1415.91	3406.7	5273.5

5.6 Summary

In this chapter, the preliminary FEM simulations for mass sensors design are presented and discussed for different mass sensing cases:

- Point mass detection of single particles of platinum (considered cubical) deposited on top of two WGD resonators vibrating in the VHF range at 189 MHz. Different particle emplacement have been simulated in order to evaluate the importance of the resonance shape with regard to the mass sensitivities. The maximum point mass sensitivities (PMS) that has been obtained is 796 kHz·pg^{-1}, for a multiple particle deposition distributed homogeneously on the resonators surface.

- Point mass detection of single particles for different particles size (but same mass). The PMS has been proven to increase for larger contact areas between the particle and the resonator. For particles with the same mass, the extracted distributed mass sensitivities (DMS) increases by a factor of 1.7 times, (from 100 kHz to 172 kHz) when the contact area particle-disk increases by a factor of 16 times (cube side from 500 nm to 2 μm).

- Distributed mass detection of uniform layers (thickness of 10 nm) of goat IgG deposited on the surface of two WGD resonators vibrating at 189 MHz and 394 MHz. The extracted DMS have been 86 $\mu m^2 \cdot ng^{-1}$ for the smallest disk (394 MHz) and 161 $\mu m^2 \cdot ng^{-1}$ for the largest (189 MHz).

Experimental point and distributed mass sensitivity have been obtained by extracting the mass load effect due to the deposited HfO_2 layer used to fill the gaps in the resonators whose characterization is detailed in Chapter 4. This experiment provides a way to precisely obtained the mass sensing performance from the fabricated devices without using direct metal write techniques such us FIB pellets deposition.

The mass sensing characterization has been carried out in two devices vibrating in flexural mode: CCB (f_0 = 5.72 MHz) and DETF (f_0 = 11.1 MHz); and two devices vibrating in bulk mode: PBR (f_0 = 23.6 MHz) and WGD (f_0 = 41.08 MHz). An exhaustive analysis of the mass loading effect coming from the HfO_2 ALD layers, the resonance frequency shifts and the influence of effective area and mass is presented.

A PMS of 29.52 kHz·pg^{-1} has been obtained with the DETF and a DMS of 5273.5 kHz·$\mu m^2 \cdot pg^{-1}$ has been obtained with the WGD. As it is included in Table 5.1 the performance of tbe DETF and the WGD are beyond the state-of-the-art of the MEMS resonators for mass sensing. The comparison of the experimental results with FEM simulations remains a meaningful study for future investigations.

6 Conclusions

6.1 Major Achievements in this Work

During the last few years significant efforts have been made on achieving better MEMS resonators performances in terms of improving the technology and design, increasing the output signal levels, reducing motional resistance and increasing quality factors in order to accomplish full integrable devices with monolithic electronics for filtering, frequency reference and sensing applications.

In this context, partially-filled high-k dielectric gap resonators have been proposed to reduce the motional resistance and improve the f_0xQ figure-of-Merit of MEMS resonators thanks to the contributions of high-k dielectrics in the enhancement of the coupling transduction in the gap.

This work was dedicated to identify, propose and validate improvements in the design, fabrication and characterization of air and partially-filled high-k dielectric gap MEMS resonators in the HF/VHF frequency range. Additionally, we have explored the potential applications of such resonators for mass sensing. This project was funded by the Swiss National Science Foundation (SNSF).

145

The main technical contributions of this work are summarised as follows:

- **Analytical and Finite-Elements-Method (FEM) models study.** Exhaustive theoretical models were amply reviewed and validated with FEM simulations and ulterior experimental measurements. Preliminary FEM simulations for mass sensors design for point and distributed mass detection were discussed taking into account wine-glass disk (WGD) resonators vibrating at 189 Mz and 394 Mz. Simulated point mass sensitivity (PMS) of 796 kHz $\cdot pg^{-1}$ and distributed mass sensitivity (DMS) of 161 kHz $\mu m^2 \cdot ng^{-1}$ were achieved. These studies provided the necessary basis concerning resonators dimensioning in order to scheme the fabrication designs.

- **Fabrication of RF MEMS resonators with nanometric transduction air and HfO$_2$ partially-filled gaps.** A novel full wafer microfabrication process was validated for the development of capacitive MEMS resonators based on air and partially-filled gaps. Gap dimensions were scaled down to 100 nm using electron beam (E-beam) lithography and gap-filling was carried out by means of ALD of hafnium oxide (HfO$_2$) in the EPFL cleanroom facilities. Diverse flexural (clamped-clamped beams, CCB and double-ended tuning forks, DETF) and bulk (parallel beams, PB, wine-glass disks, WGD, and square plate, SP) resonators with variations of geometrical dimensions included on the same chip were simultaneously released by means of vapor HF etching, giving rise to well-aligned suspended structures.

- **Optical, capacitive and piezoresistive characterization of sub-micron air gaps MEMS resonators.** Contrasted detection setups were built and cross-checked in order to determine the most performing characterization method for the fabricated resonators. Piezoresistive detection was endorsed as the one with better measured transmission scattering parameters, showing output signal magnitudes up to six times higher than for their capacitive counterpart in WGD resonators vibrating at 41.1 MHz. The fabricated flexural and bulk resonators were validated in the range of 5 MHz to 70 MHz.

- **Gap-filling effect investigation.** By means of capacitive and piezoresistive characterization of sub-micron HfO$_2$ partially-filled MEMS resonators, HfO$_2$ gap filling was proven to improve up to ten times the obtained motional resistance of DETFs vibrating at 10.4 MHz and up to three times the one of WGDs vibrating at 41.1 MHz after an HfO$_2$ ALD covering of 5 nm per gap sidewall in air-gap resonators of 100 nm (final air-gap 90 nm).

- **Novel HfO$_2$ partially-filled gaps DETF and PBR resonators.** A DEFT resonator working at 11 MHz with 90 nm-air-gap and 10 nm-HfO$_2$-gap features amplified signal detection, Q-factor of 8433 and a reduction of 18 times the motional resistance in comparison with their air-gap counterpart. This is the first time in literature where flexural DETF HfO$_2$ partially-filled gaps MEMS resonators are fabricated and characterized, suggesting an interesting solution operating at high frequency for sensing applications.

- **Novel partially-filled gaps WGD resonator excited by multiple DC probes actuation and**

  piezoresistively detected. By means of a capacitive actuation based on four probes, combined with a piezoresistive readout, the transmission response of a HfO$_2$ partially-filled gaps WGD resonator with 90 nm-air-gap and 10 nm-HfO$_2$-gap has been characterized for the first time. The devices have demonstrated to accomplish a quality factor 11760 and a motional resistance as low as 874 Ω, being promising results to be exploiting in future mass sensing applications.

- **Mass sensing characterization of flexural and bulk MEMS resonators with**

  capacitively and piezoresistive detection methods. Experimental mass sensitivity and distributed mass sensitivity have been explored by extracting the mass load effect due to the deposited HfO$_2$ layer used to fill the air-gaps. Considering the fabricated 290 nm air-gap CCB vibrating at 5.72 MHz, and experimental point mass sensitivity of 15.81 kHz $\cdot pg^{-1}$ has been obtained, better result that the one presented in [116], which was reported to be 2.27 kHz $\cdot pg^{-1}$ for a WGD vibrating at 4 MHz. The 290 nm air-gap DETF (f$_0$ = 11.1 MHz) and the 90 nm air-gap PBR (f$_0$ = 23.6 MHz) have respectively shown experimental point mass sensitivities of 29.52 kHz $\cdot pg^{-1}$ and 0.67 kHz $\cdot pg^{-1}$, revealing the DETF has the best point mass sensitive for the devices fabricated in this work. A distributed mass sensitivity of 5273.5 kHz $\cdot \mu m^2 \cdot pg^{-1}$ has been achieved with a 90 nm

air-gap WGD (f_0 = 41.08 MHz), overperforming the 5.4 kHz $\cdot \mu m^2 \cdot pg^{-1}$ presented in [113] for a WGD vibrating at 66 MHz. These results experimentally confirm the good performances and feasibility of HfO_2 partially-filled gaps MEMS resonators in mass detection applications.

6.2   Future Work

This thesis shows that there are still a number of technological innovations, such as the use of high-k dielectrics in the air gaps, capable to improve the main figures of merit of MEMS resonators in designs covering a large range of frequencies (for MHz to hundreds of MHz). Nevertheless, due to the limited time of the project and the uncountable number of issues that have been overcome during these four years, there are a number of experiments, remaining challenges and open questions regarding the partially-filled gaps MEMS resonators presented in this thesis that would be worth to be investigated as future work.

The main standing challenges are summarised as follows:

- **Alternative high-k dielectrics.** Al_2O_3, TiO_2 or AlN, among other dielectrics with k varying from 10 to 40, are very interesting high-k materials to be investigated and compared in partially-filled gaps MEMS resonators configurations.

- **Co-integration of MEMS with CMOS for low power applications.** Power consumption is a critical requirement for the insertion of MEMS resonators into truly portable manufacturable systems. In capacitive MEMS resonators, motional resistance increases with increasing frequencies resulting in larger impedance mismatch and power consumption. In this work, a deeper understanding of how to achieve lower power consumption (<20V supply voltages) without heavily impoverishing output signal levels remains a future challenge in order to co-integrate this technology with CMOS to have device and interface circuitry on the same chip.

- **Temperature stability.** As MEMS resonators are less stable in temperature than quartz crystals (quartz stability below 1 ppm/°C depending on the crystal cut), temperature compensation remains as one interrogation, overall for devices destined to perform as mass sensors in ambient environments, which are subject to constant temperature drifts. This subject still needs to be further investigated in the presented devices.

- **Packaging.** Low cost high-yield hermetic packaging is essential for MEMS resonators for commercial applications. MEMS resonators would suffer less performance degradation due to air damping or contaminants if they are protected by enclosed vacuum packaging. This 0-level or on-wafer packaging needs to be co-design and compatible with the resonator fabrication process, as well as being designed to avoid additional parasitics or stress. Partially-filled gaps resonators, like the ones developed here, can pave the way for more relaxed packaging solutions.

- **Challenges for mass sensing applications.** As it has been presented in this work, MEMS resonators can achieve mass sensitivity orders of magnitude difficult to attend with other technologies. However, the ultimate success of MEMS resonators for commercial sensing applications should be preceded by studies of the maturity of the technology in terms of yield, variability, robustness, ageing and reliability. In the same way, functionalization of the microstructures at small scale to make them selective to particular inert or biological species without substantially change the devices performance is an open interrogation for future development steps. Last but not least, SOI integrated MEMS technology enables fabrication of arrays of resonators [105] [19] [129] that is the key to achieve better temperature compensation and trimming the resonators absolute frequency to (a) compensate non-idealities of individual devices; (b) overcome eventual poor output signal levels coming from standalone devices by processing multi-outputs arrays instead; (c) provide larger programmable bandwidth granularity coming from co-integrated devices and (d) increased mass sensors functionalized effective area to fulfil better mass resolution.

A Phase-Slope Approximation

The main method to calculate the quality factor of a resonator from the transmission scattering parameters (S_{21}) considers the bandwidth between the two cut-off frequencies at -3 dB from the magnitude peak:

$$Q = \frac{f_0}{BW} \tag{A.1}$$

where f_0 is the center-frequency of the peak and BW is the half-power or 3 dB bandwidth around f_0. When the measured resonance peak magnitude is lower than 3 dB, the previous equation cannot be used. In this case, Q-factor can be calculated from the phase measurements [54] [74] [75] as:

$$Q \approx Q_{ph} = \frac{\omega_0}{2} \frac{d\phi}{d\omega} = f_0 \frac{\pi}{360} \frac{d\phi}{df} \tag{A.2}$$

where ω_0 is the natural resonance frequency of the device and $\frac{d\phi}{df}$ is the slope of the phase at resonance. As example, the Q-factor of a square plate resonator has been calculated by means of both methods as shown in Figure A.1. A multi-peak Lorentz fitting and a linear fitting have been respectively applied on magnitude and phase of the measured signal with the aim of precisely measuring the needed parameters (resonance frequency, bandwidth and phase-slope). Q-factor calculated with the BW equation is $Q_{BW} = 844$ and the one approximated with the phase-slope method is $Q_{ph} = 784$, therefore, Q_{ph} matched Q_{BW} with a relative error around 7%.

(a) Magnitude (gray) measured data; (black) signal after Lorentz fitting.
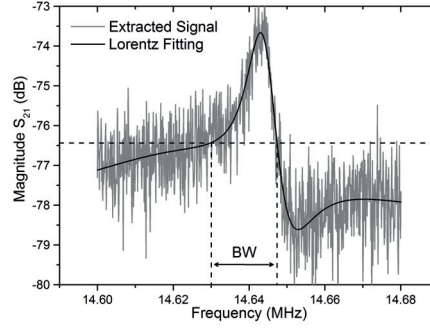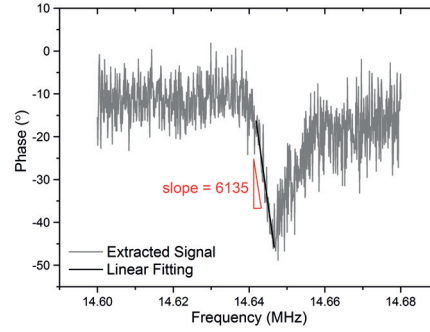
(b) Phase (gray) measured data; (black) signal after linear fitting.

Figure A.1 – Experimental S_{21} transmission parameter for a square plate resonator extracted by direct capacitive detection method (l_p = 20 μm, g = 100 nm, V_{bias} = 120 V).

Table A.1 – Experimental bias configuration and resulting parameters for the multi-gate actuated WGD resonator (RF power -20 dBm, V_{DC1} = 80 V, V_{DC2} = 1 V).

Parameter	Conf.1	Conf.2	Conf.3	Conf.4	Conf.5	Conf.6	Conf.7
V_{DC3}, (V)	0	40	80	80	0	80	-80
V_{DC4}, (V)	0	40	80	0	-80	-80	-80
f_0, (MHz)	41.2507	41.2487	41.2470	41.2412	41.2391	41.2331	41.2331
Q, (by BW)	7500	9015	7953	10815	7951	7950	11760
Q, (by phase-slope)	8006	9059	8192	9989	8025	8493	12163
R_m, (Ω)	1.49k	1.25k	1.41k	1.04k	1.41k	1.41k	874

Nevertheless, the phase-slope method is not accurate whenever the acquired S_{21} phase has not a clear transition at resonance. An illustration of this case is shown in Figure A.2, where the experimental magnitude and phase of the transmission parameter of a PBR (N = 12, l_b = 151 μm, w_b = 5 μm, g = 100 nm, V_{bias} = 70 V) acquired by direct capacitive detection is depicted. As it can be observed, noise transition of the phase at resonance affect the slope extraction,

A.152

leading to a mistaken calculation of Q = 38000, result that is clearly far from the bandwidth shown by the resonance peak.
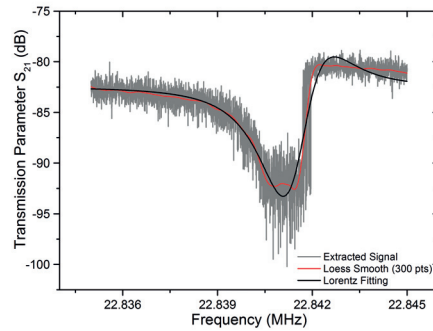
(a) Magnitude (gray) measured data; (black) signal after Lorentz fitting.
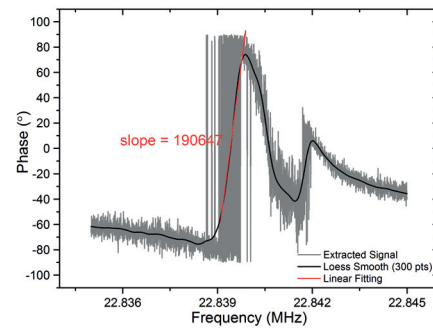
(b) Phase (gray) measured data; (black) signal after linear fitting.

Figure A.2 – Experimental S_{21} transmission parameter for a PBR extracted by direct capacitive detection method (N = 12, l_b = 151 μm, w_b = 5 μm, g = 100 nm, V_{bias} = 70 V).

During this work, a validation of the phase-slope approximation has been carried out for every fabricated resonator that exhibited resonance peaks above 3 dB. The resulting Q-factors calculated with both methods for several DETFs and WGD resonators in diverse bias configurations (consult Table A.1), can be seen below. The averaged relative error percent has been calculated and included in each plot, giving rise to a global averaged relative error of 8.1%.

Appendix A. Phase-Slope Approximation
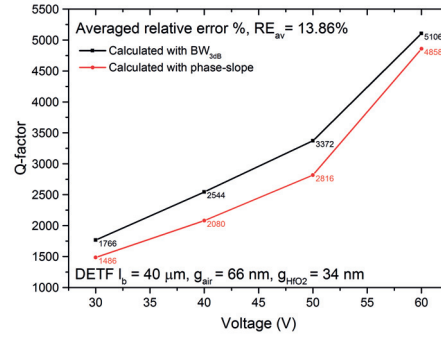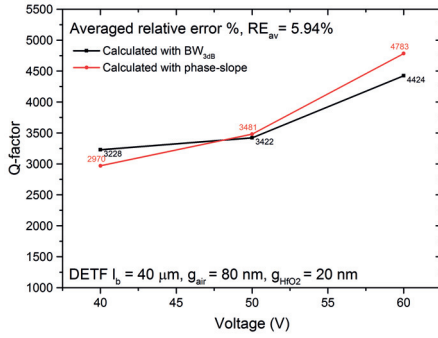
(a) Air gap g_{air} = 80nm. HfO$_2$ gap g_{HfO2} = 20nm.   (b) Air gap g_{air} = 66nm. HfO$_2$ gap g_{HfO2} = 34nm.

Figure A.3 – Q-factor experimentally extracted with the BW and the phase-slope methods for a DETF resonator (l_b = 40 μm).
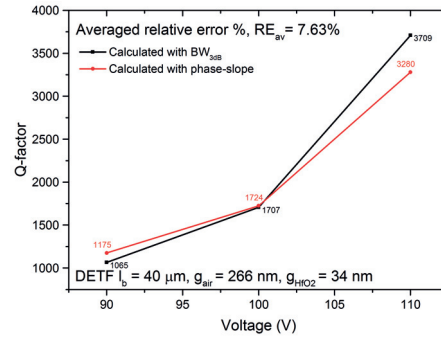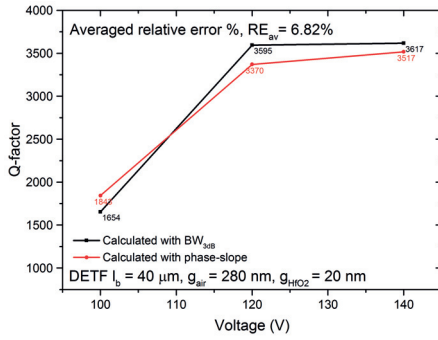
(a) Air gap g_{air} = 280nm. HfO$_2$ gap g_{HfO2} = 20nm.   (b) Air gap g_{air} = 266nm. HfO$_2$ gap g_{HfO2} = 34nm.

Figure A.4 – Q-factor experimentally extracted with the BW and the phase-slope methods for a DETF resonator (l_b = 40 μm).
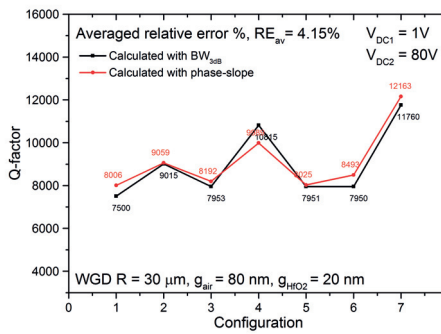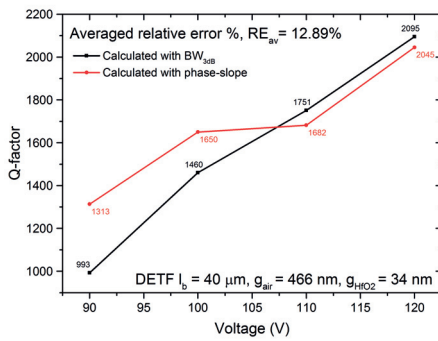
(a) Air gap g_{air} = 480nm. HfO$_2$ gap g_{HfO2} = 20nm.   (b) Air gap g_{air} = 80nm. HfO$_2$ gap g_{HfO2} = 20nm.

Figure A.5 – Q-factor experimentally extracted with the BW and the phase-slope methods for a WGD resonator (R = 30 μm).

A.154

B PVDF-TrFE Solid-Gap Resonators

Polyvinyledenedifluoride–trifluoroethylene (PVDF-TrFE) is a semi-crystalline ferroelectric copolymer that may exhibit α, β, γ and δ phases. Among these phases, β phase is important since it has an effective dipole moment. PVDF-TrFE films have been proven to by easily integrated in standard lithography fabrication processes in order to pursue cost-effective batches, film uniformity and high resolution polymer patterning [135]. PVDF-TrFE has a high-k dielectric constant and a Young's modulus around 2 GPa, therefore it is a flexible material, easy to deform by means of electromechanical forces. All these properties made it an encouraging option to be considered as the constitutive solid-gap material for resonators, willing to take advantage of an additional amplification of the output signal coming from the piezoelectric effect. In this section, first PVDF-TrFE preparation and characterization are presented. Coming up next, the fabrication process for PVDF-TrFE solid-gap resonators that was carried out during the course of this work is detailed.

B.1 PVDF-TrFE Preparation

Powder of PVDF-TrFE 70:30 was diluted to 3 w/v % in Methylethylketone (MEK), which provides the most consistent quality films with acceptable electric properties. PVDF-TrFE power and MEK were poured into a round-bottom flask that was firmly clamped and submerged into an oil bath heated at 55°C by a magnetic stirrer. A thermometer was introduced into the oil in order to control the temperature stability. The solution vapours were condensed and reflux

to the flask by means of a condenser connected to the tap. The solution was mixed during 24 hours by submerging a magnetic stir bar into the flask. The complete setup is depicted in Figure B.1.

Figure B.1 – PVDF-TrFE preparation setup: (left) complete setup (magnetic stirrer, round-bottom flask, oil batch, condenser and thermometer) and (right) details of the PVDF-TrFE power and the magnetic stir bar.

B.2   PVDF-TrFE Deposition

The deposition of the PVDF-TrFE solution was carried out by means of a spin coater [136].

The wafer (or chip) was placed on the spin coater plate and carefully covered with the solution in order to avoid air bubbles, which create inhomogeneities on the surface. The spin coating steps were the following:

(1) Coating for 15 seconds (velocity, v = 500 rpm and acceleration, a = 1000 rpm/s).

(2) Coating for 180 seconds (velocity, v = 4990 rpm and acceleration, a = 2000 rpm/s).

(3) Hot plate annealing for 45 minutes (temperature, T = 100°C).

(4) Hot plate annealing for 45 minutes (temperature, T = 120°C).

Longer annealing times/higher temperatures improve mechanical and electrical properties but also increase roughness as mesas form on the surface. In order to obtain the PVDF-TrFE layer thickness, a sharp step was created on the layer by covering an area of the wafer with
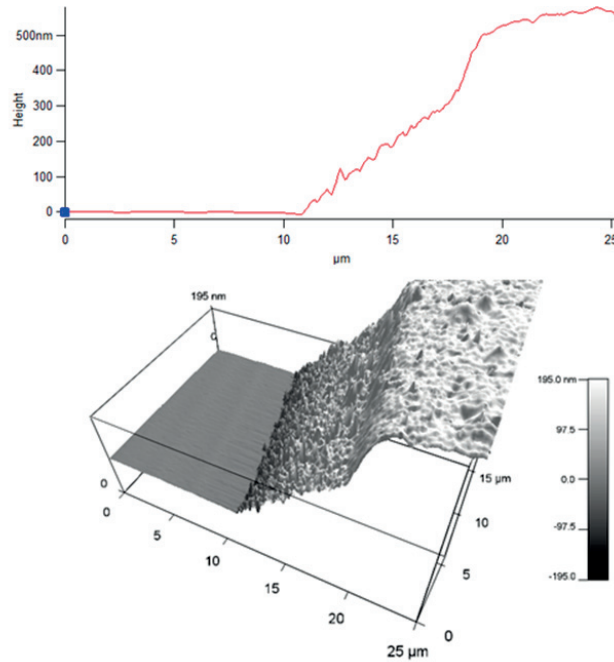
Figure B.2 – Step profile of the deposited PVDF-TrFE layer of 500 nm measured with an AFM.

a clean wafer die and performing an oxygen plasma etch. This step was measured with an Atomic Force Microscope (AFM). The resulting measured thickness was around 500 nm and can be observed in Figure B.2.

B.3 PVDF-TrFE Characterization

B.3.1 Polarization

The lateral actuation needed to completely polarize a gap of PVDF-TrFE was measured in a test structure consisting of two in-plane parallel electrodes of 3.5 mm side spaced 1 μm with a thickness of 200 nm (see Figure B.3). Both longitudinal parallel electrodes were contacted by means of metallic tips and a dynamic hysteresis parametric analysis was performed. The measurements evidence the quality of the PVDF-TrFE polarization and the possibility of actuate it laterally (see Figure B.3). The voltage needed to achieve a complete polarization of the PVDF-TrFE is expected to be scalable in function of the dimensions of the actuated structure.

B.3.2 Capacitance and Dielectric Constant

The relative dielectric constant for a 600 nm layer of PVDF-TrFE has been calculated from the capacitance measurements of a circular parallel plate capacitor made by sputtering Au (area, A = $3.2 \cdot 10^{-3}$ cm^2) on PVDF-TrFE as depicted in Figure B.4. Capacitance was measured by scratching and contacting the bottom electrode and the top circular electrode. As shown in Figure B.5 the dielectric constant decreases with frequency, triggering PVDF-TrFE to HF applications.

B.4 MEMS Resonators Gap-Filling with PVDF-TrFE

In order to check the PVDF-TrFE gap-filling of HARS gaps (depth of the order of μm and width from 100 nm to 1 μm), silicon gaps were etched and covered with PVDF-TrFE as describes above.

The resulting solid-gaps are shown in the FIB cut of Figure B.6 (left). As it is shown, the Pt hard mask that was used during the milling obscures the contrast needed to determined the amount of PVDF-TrFE present into the gaps. Nevertheless, if we focussed in the gap designed at 100 nm, the copolymer seems to fill the gap, despite the detachment shown on one of the sidewalls, which may coming from the FIB technique itself.

B.5 Fabrication Process

Fabrication steps (a-e) are detailed in Section 4.3.1. With the pursue of filling the gaps, PVDF-TrFE is deposited by the spin coating followed by a hard bake steps referred above (see Figure B.8.f). Titanium is sputtered (Figure B.8.g)and then E-beam patterned and dry etch (Figure B.8.g-i) to act as a hard mask for PVDF-TrFE etch by means of an O_2 DRIE process (Figure B.8.j). The Ti hard mask is removed in diluted HF (1:100) bath and then the structures are released with a vapor-phase HF etch (Figure B.8.k). Figure B.7 illustrates a FIB cut of a PVDF-TrFE solid-gap WGD resonator.

B.6 Critical Points

Some of the main issues found during this fabrication and characterization batch are:

- Needed PVDF-TrFE dissolutions were not available, therefore their manual preparation and the subsequent study of the basic properties of the material have to be done before starting the fabrication.

- PVDF-TrFE spin coating deposition rates cannot be predicted and they have to be extracted for every unique mix. Ellipsometer, reflectometer and profilometer-based techniques demonstrated not to be precise to measure the thickness. Measurements based on Atomic Force Microscopy (AFM) were taken into consideration with optimal results.

- PVDF-TrFE has a melting point around 177°C and a Curie temperature around 110°C, so many standard steps used in microfabrication that imply temperatures above those values had to be substituted. For example, RT Pt and Ti sputtering were used to not to damage the copolymer.

- PVDF-TrFE is incompatible with many standard solvents/developers/strippers used in microfabrication and they have to be avoided (acetone, etc.). Etching techniques of PVDF-TrFE have been hardly proposed in literature. Fabrication flows based on plasma and Ion-Beam etch, buffered HF and vapor HF were tested in order before arriving to RIE O_2 etch as the best solution.

- The electrical characterization (see Section 4.4) that followed the fabrication process presented above was unsuccessful: the devices did not exhibit resonance in a range of frequencies around ±50 MHz the designed resonance frequency. DC voltages up to ±200 and RF power between -30 and 10 dBm were evaluated without making vibrate the devices. The devices are too damped by the presence of the copolymer, not only into the gap but also on the electrodes and resonator body, as it is shown in Figure B.7.

- In order to decrease the damping and benefit from gap-filling effect (see Chapter 4), future MEMS resonators based on PVDF-TrFE gap-filling must be carried out by means of alternative deposition techniques, as the spray deposition [137].
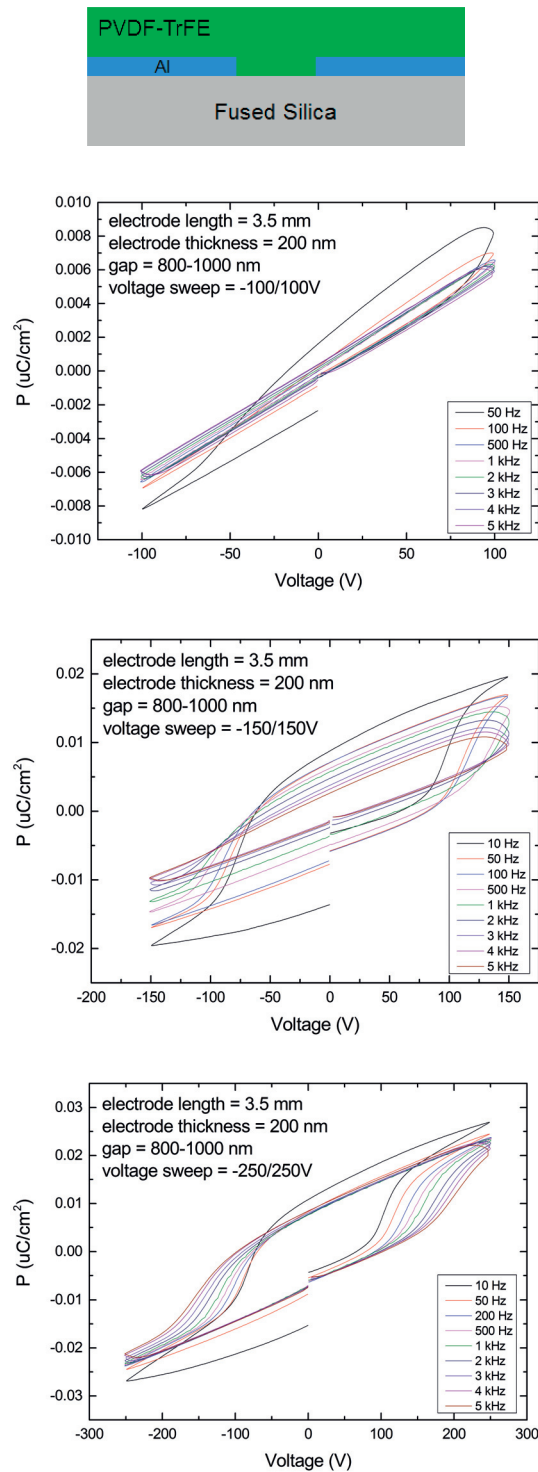
Figure B.3 – In-plane parallel electrodes of 3.5 mm side with a thickness of 200 nm spaced 1 μm used to carry out the hysteresis loops of PVDF-TrFE. and hysteresis loops for two in-plane parallel electrodes of 3.5 mm side with a thickness of 200 nm spaced 1 μm with different voltages sweeps.
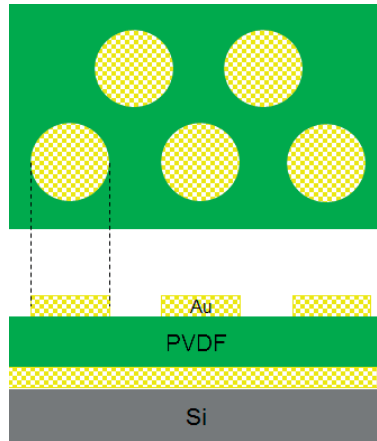
Figure B.4 – Parallel plate capacitor used to extract the relative dielectric constant of PVDF-TrFE.
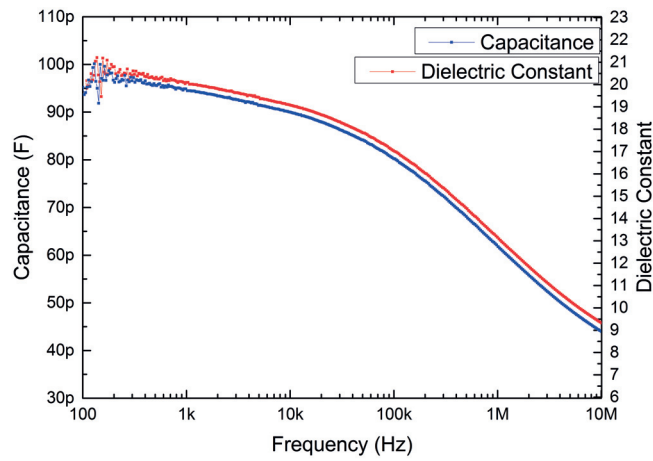
Figure B.5 – Experimental dielectric constant of PVDF-TrFE extracted from capacitance measurements a circular parallel plate capacitor made by sputtering Au (area, A = 3.2 $\cdot 10^{-3}$ cm^2) on PVDF-TrFE.
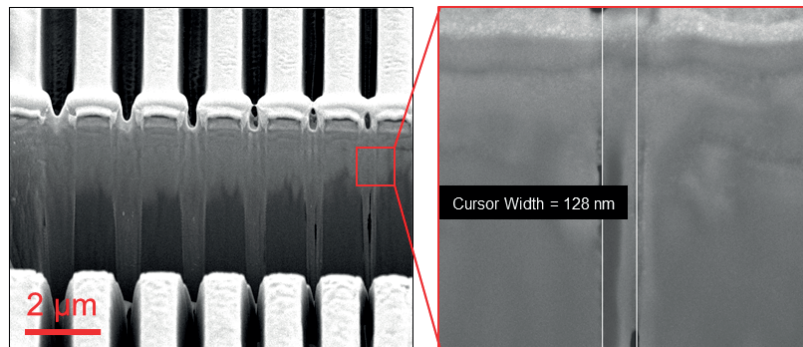
Figure B.6 – FIB cut of silicon gaps covered by PVDF-TrFE. Gaps width from right to left: 100, 200, 300, 400, 500, 700, 900, 1000 nm.
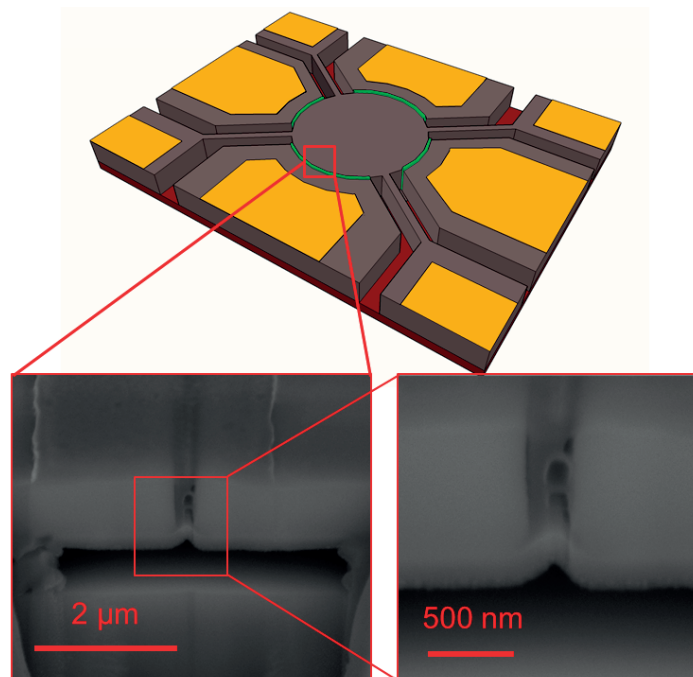
Figure B.7 – FIB cut of a PVDF-TrFE solid-gap MEMS resonator.

a. Doping/Deglazing/Extra Diffusion
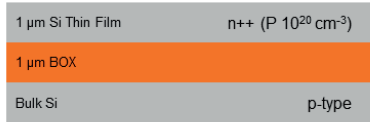
1 μm Si Thin Film   n++ (P 10^{20} cm^{-3})

1 μm BOX

Bulk Si   p-type

b. Alignment Marks

c. E-beam Patterning and Si Dry Etch

ZEP Resist

g. Ti Sputtering

75 nm
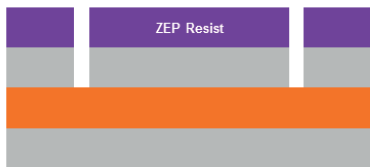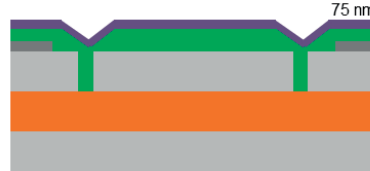
h. E-beam patterning

i. Ti Dry Etch

a. Doping/Deglazing/Extra Diffusion
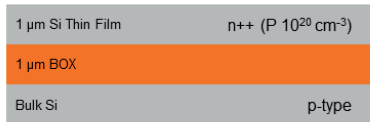
1 μm Si Thin Film   n++ (P 10^{20} cm^{-3})

1 μm BOX

Bulk Si   p-type

b. Alignment Marks

c. E-beam Patterning and Si Dry Etch

ZEP Resist

g. Ti Sputtering

75 nm
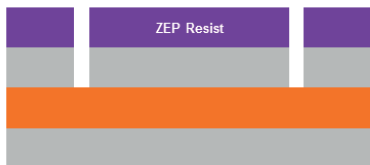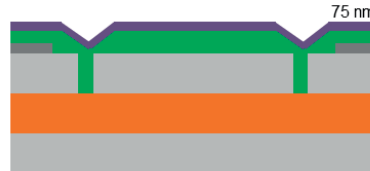
h. E-beam patterning

i. Ti Dry Etch

Figure B.8 – Schematic of the fabrication process used to create PVDF-TrFE solid-gap MEMS resonators.

C Parameters Extraction

C.1 Feedthrough Capacitance

Feedthrough capacitance C_0, is a physical capacitance formed by the terminal contacts and associated metals. Because the feedthrough capacitance is in parallel with the series resonance branch (see Figure C.1), it provides an additional current path between the terminals that takes current away from the resonance branch, which is equivalent to weakening the strength of resonance. In a resonator measurement, C_0 can drag down the measured response peak and change the resonant frequency or even obscure the resonator response altogether.
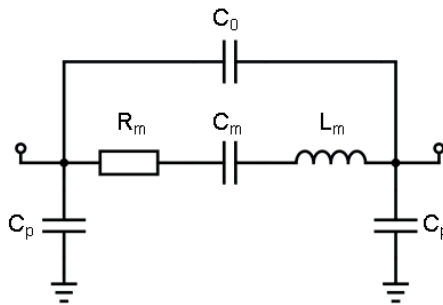
Figure C.1 – Simplified electrical circuit of a two-port capacitive MEMS resonator with feedthrough capacitance C_0.

The impedance of the feedthrough capacitance at resonance should be much larger than impedance of the resonance branch, such that the majority of the current goes through the resonance branch and not through the capacitance. This is why low-impedance resonators can accommodate larger feedthrough capacitance than high-impedance ones. However, if there is

excessive amount of feedthrough capacitance, more current flows through the capacitor than through the resonance branch.

The transmission through a 2-port network has a capacitive feedthrough floor which is proportional to both operating frequency and parasitic capacitance. More generally, any low impedance feedthrough path is harmful and should be eliminated as much as possible.

The combined frequency response of the device admittance Y_{res}, including feedthrough contributions, is given by:

$$Y_{res} = \frac{j\omega C_m}{1 - (\omega/\omega_0^2) + j(\omega/\omega_1)1/Q} + j\omega C_0 \tag{C.1}$$

At resonance, one can assume that the reactive impedances from C_m and L_m cancel out, leaving only the resulting admittance:

$$Y_{res} = \frac{1}{R_m} + j\omega_0 C_0 \tag{C.2}$$

The feedthrough capacitance is estimated using the off-resonance feedthrough level of S_{21} [138]:

$$S_{21}(f) = \frac{2Z_0}{2Z_0 + 1/(j\omega C_0)} \tag{C.3}$$

where Z_0 is the characteristic impedance. For high frequencies and small capacitances, feedthrough capacitance can be calculated as [138]:

$$C_0 = \frac{10^{S_{21}/20}}{2Z_0(2\pi f)} \tag{C.4}$$

C.2   Motional Resistance

Assuming that a resonator is represented by a two port network consisting of an impedance Z_{res} that connects ports 1 and 2, the measured transmission scattering parameter characteristic is

dependant on the measured resonator impedance as follows:

$$S_{21}(f) = \frac{2Z_0}{2Z_0 + Z_{res}(f)}$$

(C.5)

Considering Equation C.2, in the ideal case R$_m$ « $1/\omega$C$_0$ and the measured transmission S$_{21}$ parameter can be related with the motional resistance as:

$$S_{21}|_{f=f_0} = 20log\left(\frac{2Z_0}{2Z_0 + R_m}\right)$$

(C.6)

Loaded motional resistance can be calculated from the transmission peak height:

$$R_m = 2Z_0(10^{-(S_{21}|_{f=f_0})/20} - 1)$$

(C.7)

When R$_m$ > $1/\omega$C$_0$ de-embedding techniques are needed to remove the static signal component caused by C$_0$ [106] [107] [108].

C.3 Parameter Extraction: HfO$_2$ Gap-Filling of a DEFT

There are two important consequences of the feedthrough capacitance. First of all, it determines the noise floor level of the sweep measurement (minimum signal level). Secondly, the electrical measurement of the resonator differs significantly from the ideal response and C$_0$ introduces an antiresonance peak.

As C$_0$ determines the noise floor level of the signal, the motional resistance can be approximated by means of Equation C.7 whether the values of the parasitic capacitances (C$_0$ and C$_p$) can be neglected. Taking into account the extracted S$_{21}$ signals for the case of the gap-closing of the DETF presented in Section 4.6.1, we can see how the signal level changes with the depositions, being observed a lowering of the signal level of -12 dB after the first deposition (5 nm), +2 dB after the second deposition (5 nm), and -6 dB after the last deposition (10 nm).

Motional resistances have been extracted from the S$_{21}$ measurements included in Figure C.2 by means of Equation C.7 and they are included in Table C.1. As we can see, these calculations

(a) Air-gap

(b) HfO$_2$ ALD 5 nm

(c) HfO$_2$ ALD 10 nm

(d) HfO$_2$ ALD 20 nm
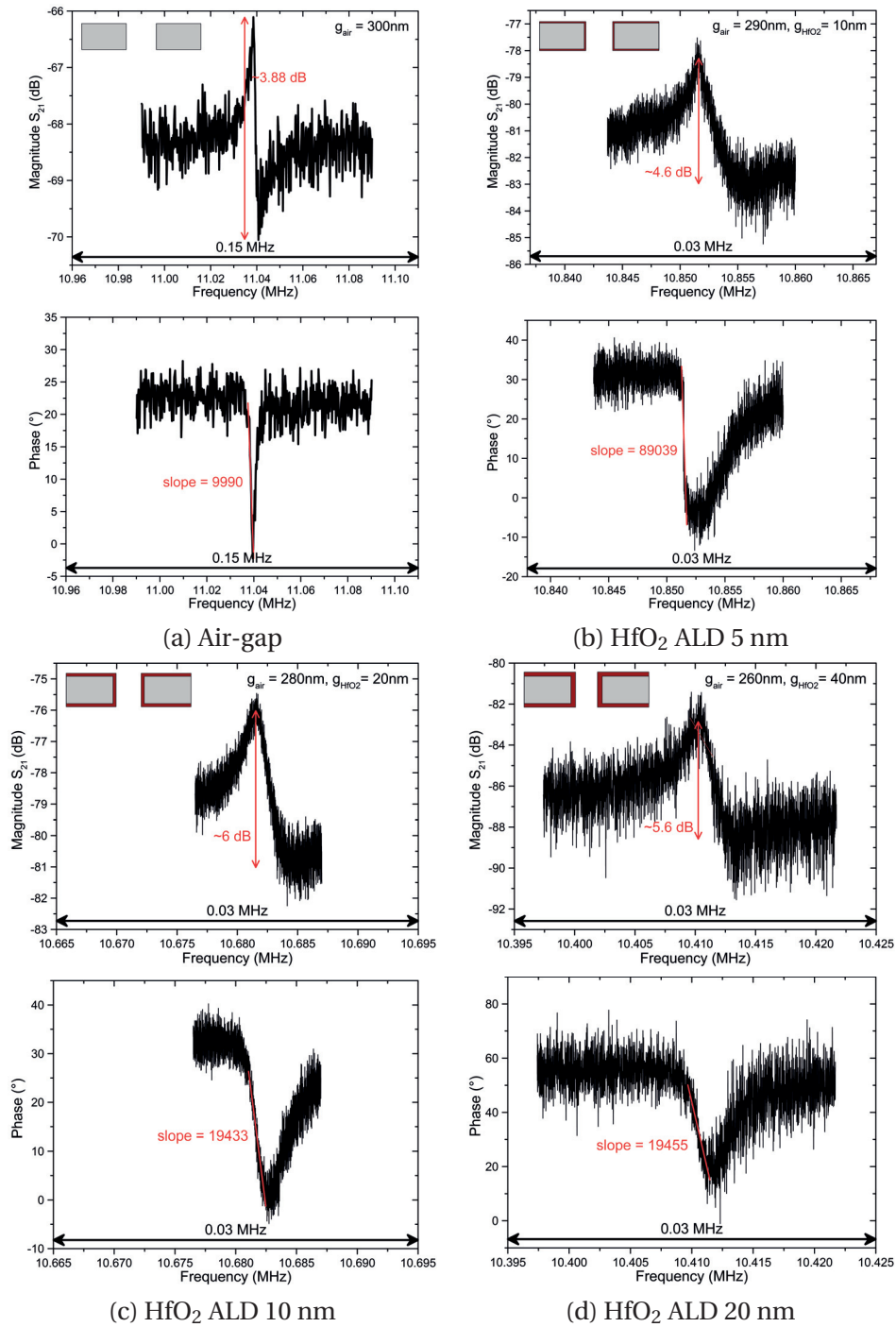
Figure C.2 – Experimental transmission parameters for a DETF (l_b = 40 μm and w_b = 3 μm), with an initial air-gap of 300 nm and three consecutive HfO$_2$ depositions of thickness 5 nm, 5 nm and 10 nm: (a) 300 nm air-gap; (b) 20 nm air-gap and 10 nm HfO$_2$; (c) 280 nm air-gap and 20 nm HfO$_2$ and (d) 260 nm air-gap and 40 nm HfO$_2$. The applied DC bias V_{DC1} = V_{DC2} = 90V and the RF power -20 dBm. Notice that the frequency scales are different for (a) and (b-d).

Table C.1 – Extracted motional parameters for a DETF (l$_b$ = 40 μm and w$_b$ = 3 μm), with an initial air-gap of 300 nm and three consecutive HfO$_2$ depositions of thickness 5 nm, 5 nm and 10 nm.

ALD layer	f$_0$ (MHz)	R$_m$ (Ω)	C$_0$ (F)	ω_0C$_0$ (S)	1/R$_m$ (S)
0	11.0387	199.4k	54.38f	$3.77 \cdot 10^{-6}$	$5.02 \cdot 10^{-6}$
5 nm	10.8516	794.2k	12f	$8.18 \cdot 10^{-7}$	$1.26 \cdot 10^{-6}$
10 nm	10.6816	630.9k	15f	$1.59 \cdot 10^{-6}$	$1.01 \cdot 10^{-6}$
20 nm	10.4105	1.3M	13f	$8.5 \cdot 10^{-7}$	$7.69 \cdot 10^{-7}$

depend on the levels of the signals and the levels change after each deposition, therefore the calculated R$_m$ change accordingly, not following the decreasing tendency that has been proven in literature [30] [31].

In order to check if this approximation fulfils the needed condition to be applied (R$_m$ « 1/ωC$_0$), Equation C.4 has been used in order to obtain a value for the feedthrough capacitance in a range between 10.3 and 11 MHz. As we can see in the last two columns of Table C.1, the admittances in both branches, ωC$_0$ and 1/R$_m$ (see Figure C.1) are very similar. Therefore, it can be concluded that in order to use Equation C.7 to calculate the motional resistance, a de-embedding of the signal in order to cancel the effect of C$_0$ in the calculations is needed [106] [107] [108]. This de-embedding will become even more critical for hishger freqeuncies (i. e. for the resonators measured with f$_0$ > 10 MHz).

In conclusion, in this work the reported motional resistances have been extracted by means of the expression (see Section 3.2):

$$R_m = \frac{1}{Q} \frac{kg^4}{\epsilon^2 \omega_0 A^2 V_{bias}^2} \qquad (C.8)$$

De-embedding remains a needed future step in the electrical characterization of the air and partially-filled gap MEMS resonators addressed during this work [106] [107] [108].

Bibliography

[1] N. Maluf and K. Williams, *Introduction to microelectromechanical systems engineering*, 2nd ed.   Artech House, 2004.

[2] H. C. Nathanson, W. E. Newell, R. A. Wickstrom, and J. R. Davis, "The resonant gate transistor," *IEEE Transactions on Electron Devices*, vol. 14, no. 3, pp. 117–133, 1967.

[3] G. T. A. Kovacs, N. I. Maluf, and K. E. Petersen, "Bulk micromachining of silicon," *Proceedings of the IEEE*, vol. 86, no. 8, pp. 1536–1551, 1998.

[4] H. van Heeren and P. Salomon, "Mems: recent developments, future directions," *Electronics Enabled Products Knowledge Transfer Network*, 2007.

[5] D. Grogg, "Active microelectromechanical resonator: The vibrating body field effect transistor," Ph.D. dissertation, EPFL, 2010.

[6] A. Samarao, G. Casinovi, and F. Ayazi, "Passive tcf compensation in high q silicon micromechanical resonators," in *IEEE International Conference on Micro Electro Mechanical Systems (MEMS)*, 2010, pp. 116–119.

[7] R. Cox, F. Josse, S. Heinrich, I. Dufour, and O. Brand, "Resonant microcantilevers vibrating laterally in viscous liquid media," in *IEEE International Frequency Control Symposium (FCS)*, 2010, pp. 85–90.

[8] J. Basu and T. K. Bhattacharyya, "Microelectromechanical resonators for radio frequency communication applications," *Microsystem Technologies*, vol. 17, no. 10, pp. 1557–1579, 2011.

Bibliography

[9] S. Pourkamali, G. K. Ho, and F. Ayazi, "Vertical capacitive sibars," in *IEEE International Conference on Micro Electro Mechanical Systems (MEMS)*, 2005, pp. 211–214.

[10] J. Van Beek, K. Phan, G. Verheijden, G. Koops, C. Van der Avoort, J. Van Wingerden, D. E. Badaroglu, J. Bontemps, and R. Puers, "A piezo-resistive resonant mems amplifier," in *IEEE International Electron Devices Meeting, (IEDM)*, 2008, pp. 1–4.

[11] J. Van Beek, G. Verheijden, G. Koops, K. Phan, C. Van der Avoort, J. Van Wingerden, D. E. Badaroglu, and J. Bontemps, "Scalable 1.1 ghz fundamental mode piezo-resistive silicon mems resonator," in *IEEE International Electron Devices Meeting (IEDM)*, 2007, pp. 411–414.

[12] D. Grogg, D. Tsamados, N. D. Badila, and A. M. Ionescu, "Integration of mosfet transistors in mems resonators for improved output detection," in *International Solid-State Sensors, Actuators and Microsystems Conference (TRANSDUCERS)*, 2007, pp. 1709–1712.

[13] D. Grogg, M. Mazza, D. Tsamados, and A. M. Ionescu, "Multi-gate vibrating-body field effect transistor (vb-fets)," in *IEEE International Electron Devices Meeting, (IEDM)*, 2008, pp. 1–4.

[14] A. M. Ionescu, "Resonant body transistors," in *Device Research Conference (DRC)*, 2010, pp. 181–182.

[15] M. Ziaei-Moayyed, P. Resnick, B. Draper, and M. Okandan, "Radial bulk-mode vibrations in a gate-all-around silicon nanowire transistor," in *IEEE International Conference on Micro Electro Mechanical Systems (MEMS)*, 2012, pp. 1340–1343.

[16] N. Abelé, V. Pott, K. Boucart, F. Casset, K. Séguéni, P. Ancey, and A. Ionescu, "Comparison of rsg-mosfet and capacitive mems resonator detection," *Electronics Letters*, vol. 41, no. 5, pp. 242–244, 2005.

[17] M. Saukoski *et al.*, "System and circuit design for a capacitive mems gyroscope," Ph.D. dissertation, Helsinki University of Technology, 2008.

[18] H. Ding, L. Fu, Y. Wang, and J. Xie, "Resonant frequency tunable silicon fishbone-shaped mems double ended tuning fork," in *International Conference on Nano/Micro Engineered and Molecular Systems (NEMS)*, 2016, pp. 233–236.

[19] C. T.-C. Nguyen, "Mems-based rf channel selection for true software-defined cognitive radio and low-power sensor communications," *IEEE Communications Magazine*, vol. 51, no. 4, pp. 110–119, 2013.

[20] W.-C. Chen, W. Fang, and S.-S. Li, "Vhf cmos-mems oxide resonators with q> 10,000," in *IEEE International Frequency Control Symposium (FCS)*, 2012, pp. 1–4.

[21] W. Zhang, H. Zhu, and J. E. Y. Lee, "Piezoresistive transduction in a double-ended tuning fork soi mems resonator for enhanced linear electrical performance," *IEEE Transactions on Electron Devices*, vol. 62, no. 5, pp. 1596–1602, 2015.

[22] Z. Xiong, B. Walter, E. Mairiaux, M. Faucher, L. Buchaillot, and B. Legrand, "Mems piezoresistive ring resonator for afm imaging with pico-newton force resolution," *Journal of Micromechanics and Microengineering*, vol. 23, no. 3, 2013.

[23] A. Rahafrooz and S. Pourkamali, "Active self-q-enhancement in high frequency thermally actuated m/nems resonators," in *IEEE International Conference on Micro Electro Mechanical Systems (MEMS)*, 2011, pp. 760–763.

[24] J. Van Beek, P. Steeneken, and B. Giesbers, "A 10 mhz piezoresistive mems resonator with high q," in *International Frequency Control Symposium and Exposition*, 2006, pp. 475–480.

[25] N. Badila-Ciressan, M. Mazza, D. Grogg, and A. Ionescu, "Nano-gap micro-electro-mechanical bulk lateral resonators with high quality factors and low motional resistances on thin silicon-on-insulator," *Solid-State Electronics*, vol. 52, no. 9, pp. 1394–1400, 2008.

[26] D. Grogg and A. M. Ionescu, "The vibrating body transistor," *IEEE Transactions on Electron Devices*, vol. 58, no. 7, pp. 2113–2121, 2011.

[27] T. Oka, H. Tanigawa, and K. Suzuki, "Characterization of four-points-pinned ring-shaped silicon microelectromechanical systems resonator," *Japanese Journal of Applied Physics*, vol. 49, no. 6S, 2010.

Bibliography

[28] A. V. Lim, T. Karacolak, J.-Y. Jiang, C.-F. Huang, and F. Zhao, "Electrostatically-actuated 4h-sic in-plane and out-of-plane high frequency mems resonator," *IEEE Microwave and Wireless Components Letters*, vol. 26, no. 1, pp. 28–30, 2016.

[29] T. J. Cheng and S. A. Bhave, "High-q, low impedance polysilicon resonators with 10 nm air gaps," in *IEEE International Conference on Micro Electro Mechanical Systems (MEMS)*, 2010, pp. 695–698.

[30] L.-W. Hung, Z. A. Jacobson, Z. Ren, A. Javey, and C. T.-C. Nguyen, "Capacitive transducer strengthening via ald-enabled partial-gap filling," *Hilton Head*, pp. 208–211, 2008.

[31] Y.-W. Lin, S.-S. Li, Y. Xie, Z. Ren, and C.-C. Nguyen, "Vibrating micromechanical resonators with solid dielectric capacitive transducer gaps," in *IEEE International Frequency Control Symposium and Exposition*, 2005, pp. 128–134.

[32] J. L. Lopez, J. Verd, A. Uranga, J. Giner, G. Murillo, F. Torres, G. Abadal, and N. Barniol, "A cmos–mems rf-tunable bandpass filter based on two high-q 22-mhz polysilicon clamped-clamped beam resonators," *IEEE Electron Device Letters*, vol. 30, no. 7, pp. 718–720, 2009.

[33] S. T. Bartsch, D. Grogg, A. Lovera, D. Tsamados, and A. M. Ionescu, "Very high frequency double-ended tuning fork nano-mechanical fin-fet resonator," in *16th International Solid-State Sensors, Actuators and Microsystems Conference*, 2011, pp. 938–941.

[34] S. Pourkamali, Z. Hao, and F. Ayazi, "Vhf single crystal silicon capacitive elliptic bulk-mode disk resonators-part ii: implementation and characterization," *Journal of Microelectromechanical Systems*, vol. 13, no. 6, pp. 1054–1062, 2004.

[35] D. Grogg, H. C. Tekin, N. D. Ciressan-Badila, D. Tsamados, M. Mazza, and A. M. Ionescu, "Bulk lateral mem resonator on thin soi with high q -factor," *Journal of Microelectromechanical Systems*, vol. 18, no. 2, pp. 466–479, 2009.

[36] J. E. Lee, J. Yan, and A. A. Seshia, "Study of lateral mode soi-mems resonators for reduced anchor loss," *Journal of Micromechanics and Microengineering*, vol. 21, no. 4, 2011.

[37] L. Wu, M. Akgul, Z. Ren, Y. Lin, W.-C. Li, and C. T.-C. Nguyen, "Hollow stems for higher micromechanical disk resonator quality factor," in *IEEE International Ultrasonics Symposium (IUS)*, 2011, pp. 1964–1967.

[38] T. L. Naing, T. Beyazoglu, L. Wu, M. Akgul, Z. Ren, T. O. Rocheleau, and C. T. C. Nguyen, "2.97-ghz cvd diamond ring resonator with q > 40,000," in *IEEE International Frequency Control Symposium (FCS)*, 2012, pp. 1–6.

[39] E. Colinet, J. Arcamone, A. Niel, E. Lorent, S. Hentz, and E. Ollier, "100 mhz oscillator based on a low polarization voltage capacitive lamé-mode mems resonator," in *IEEE International Frequency Control Symposium (FCS)*, 2010, pp. 174–178.

[40] A.-H. Lin, J.-Y. Lee, J. Yan, and A. Seshia, "Methods for enhanced electrical transduction and characterization of micromechanical resonators," *Sensors and Actuators*, vol. 158, no. 2, pp. 263–272, 2010.

[41] V. Agache, G. Blanco-Gomez, F. Baleras, and P. Caillat, "An embedded microchannel in a mems plate resonator for ultrasensitive mass sensing in liquid," *Lab on a Chip*, vol. 11, no. 15, pp. 2598–2603, 2011.

[42] J. E.-Y. Lee and A. A. Seshia, "Direct parameter extraction in feedthrough-embedded capacitive mems resonators," *Sensors and Actuators*, vol. 167, no. 2, pp. 237–244, 2011.

[43] L. W. Hung, C. T. C. Nguyen, Y. Xie, Y. W. Lin, S. S. Li, and Z. Ren, "Uhf micromechanical compound-(2,4) mode ring resonators with solid-gap transducers," in *IEEE International Frequency Control Symposium Joint with the European Frequency and Time Forum*, 2007, pp. 1370–1375.

[44] M. Ziaei-Moayyed, D. Elata, E. Quévy, and R. Howe, "Differential internal dielectric transduction of a lamé-mode resonator," *Journal of Micromechanics and Microengineering*, vol. 20, no. 11, 2010.

[45] S. Chandorkar, M. Agarwal, R. Melamud, R. Candler, K. Goodson, and T. Kenny, "Limits of quality factor in bulk-mode micromechanical resonators," in *IEEE International Conference on Micro Electro Mechanical Systems (MEMS)*, 2008, pp. 74–77.

Bibliography

[46] M. Tilli, T. Motooka, V.-M. Airaksinen, S. Franssila, M. Paulasto-Krockel, and V. Lindroos, *Handbook of silicon based MEMS materials and technologies*. William Andrew, 2015.

[47] W.-C. Chuang, H.-L. Lee, P.-Z. Chang, and Y.-C. Hu, "Review on the modeling of electrostatic mems," *Sensors*, vol. 10, no. 6, pp. 6149–6171, 2010.

[48] M. I. Younis, *MEMS linear and nonlinear statics and dynamics*. Springer Science Business Media, 2011.

[49] G. K. Fedder, C. Hierold, J. G. Korvink, O. Tabata, O. Brand, I. Dufour, S. Heinrich, and F. Josse, *Resonant mems: Fundamentals, implementation, and application*. John Wiley & Sons, 2015.

[50] V. Kaajakari, A. T. Alastalo, and T. Mattila, "Electrostatic transducers for micromechanical resonators: Free space and solid dielectric," *IEEE Transactions on Ultrasonics, Ferroelectrics, and Frequency Control*, vol. 53, no. 12, pp. 1–5, 2006.

[51] J. Arcamone, E. Colinet, A. Niel, and E. Ollier, "Efficient capacitive transduction of high-frequency micromechanical resonators by intrinsic cancellation of parasitic feedthrough capacitances," *Applied Physics Letters*, vol. 97, no. 4, 2010.

[52] J. Lopez, J. Verd, J. Teva, G. Murillo, J. Giner, F. Torres, A. Uranga, G. Abadal, and N. Barniol, "Integration of rf-mems resonators on submicrometric commercial cmos technologies," *Journal of Micromechanics and Microengineering*, vol. 19, no. 1, 2008.

[53] K. Tanaka, R. Kihara, A. Sánchez-Amores, J. Montserrat, and J. Esteve, "Parasitic effect on silicon mems resonator model parameters," *Microelectronic engineering*, vol. 84, no. 5, pp. 1363–1368, 2007.

[54] H. Bhugra and G. Piazza, *Piezoelectric MEMS Resonators*. Springer, 2017.

[55] A. A. Barlian, W.-T. Park, J. R. Mallon, A. J. Rastegar, and B. L. Pruitt, "Semiconductor piezoresistance for microsystems," *Proceedings of the IEEE*, vol. 97, no. 3, pp. 513–552, 2009.

[56] N. Maluf and K. Williams, *Introduction to microelectromechanical systems engineering*. Artech House, 2004.

[57] Y. Kanda, "A graphical representation of the piezoresistance coefficients in silicon," *IEEE Transactions on Electron Devices*, vol. 29, no. 1, pp. 64–70, 1982.

[58] S. Pourkamali, A. Hashimura, R. Abdolvand, G. K. Ho, A. Erbil, and F. Ayazi, "High-q single crystal silicon harpss capacitive beam resonators with self-aligned sub-100-nm transduction gaps," *Journal of Microelectromechanical Systems*, vol. 12, no. 4, pp. 487–496, 2003.

[59] J. Kiihamaki, V. Kaajakari, H. Luoto, H. Kattelus, and M. Yli-Koski, "Fabrication of single crystal silicon resonators with narrow gaps," in *International Conference on Solid-State Sensors, Actuators and Microsystems, (TRANSDUCERS)*, vol. 2, 2005, pp. 1354–1357.

[60] S. Pourkamali and F. Ayazi, "Fully single crystal silicon resonators with deep-submicron dry-etched transducer gaps," in *IEEE International Conference on Micro Electro Mechanical Systems (MEMS)*, 2004, pp. 813–816.

[61] Y.-W. Lin, S.-S. Li, Y. Xie, Z. Ren, and C. T. C. Nguyen, "Vibrating micromechanical resonators with solid dielectric capacitive transducer gaps," in *IEEE International Frequency Control Symposium and Exposition*, 2005, pp. 128–134.

[62] N. Tas, T. Sonnenberg, H. Jansen, R. Legtenberg, and M. Elwenspoek, "Stiction in surface micromachining," *Journal of Micromechanics and Microengineering*, vol. 6, no. 4, p. 385, 1996.

[63] M. Bao, *Analysis and design principles of MEMS devices.* Elsevier, 2005.

[64] V. Kaajakari. Mems tutorial: Pull-in voltage in electrostatic microactuators. [Online]. Available: http://www.kaajakari.net/~ville/research/tutorials/pull_in_tutorial.pdf

[65] B. Kim, R. H. Olsson, K. Smart, and K. E. Wojciechowski, "Mems resonators with extremely low vibration and shock sensitivity," in *Sensors*, 2011, pp. 606–609.

[66] K. Wang, A.-C. Wong, and C.-C. Nguyen, "Vhf free-free beam high-q micromechanical resonators," *Journal of microelectromechanical systems*, vol. 9, no. 3, pp. 347–360, 2000.

[67] N.-D. Ciressan, "Nanogap mem resonators on soi," Ph.D. dissertation, EPFL, 2009.

[68] S. Lee, "Anchor/support design for mems resonators," 2011, uS Patent 7,990,232.

[69] S. Kausinis, K. Yee, and R. Barauskas, "Estimation of thermo-elastic damping of vibrations in micro-electro-mechanical systems resonators: finite element modeling," *Journal of Micro/Nanolithography, MEMS, and MOEMS*, vol. 11, no. 3, 2012.

[70] H. Cho, B. Jeong, M.-F. Yu, A. F. Vakakis, D. M. McFarland, and L. A. Bergman, "Nonlinear hardening and softening resonances in micromechanical cantilever-nanotube systems originated from nanoscale geometric nonlinearities," *International Journal of Solids and Structures*, vol. 49, no. 15, pp. 2059–2065, 2012.

[71] H. Zhu and J. E.-Y. Lee, "Reversed nonlinear oscillations in lamé-mode single-crystal-silicon microresonators," *IEEE Electron Device Letters*, vol. 33, no. 10, pp. 1492–1494, 2012.

[72] K. E. Wojciechowski, R. Olsson, M. S. Baker, and J. W. Wittwer, "Low vibration sensitivity mems resonators," in *IEEE International Frequency Control Symposium joint with the European Frequency and Time Forum*, 2007, pp. 1220–1224.

[73] M. de Laat, H. P. Garza, J. Herder, and M. Ghatkesar, "A review on in situ stiffness adjustment methods in mems," *Journal of Micromechanics and Microengineering*, vol. 26, no. 6, p. 063001, 2016.

[74] C. Anthony, R. Turnbull, X. Wei, M. Ward, and S. Collins, "Fabrication and quality factor control of a microelectromechanical system resonator with linear differential drive," *IET Science, Measurement & Technology*, vol. 4, no. 4, pp. 206–213, 2010.

[75] B. Razavi, "A study of phase noise in cmos oscillators," *IEEE Journal of Solid-State Circuits*, vol. 31, no. 3, pp. 331–343, 1996.

[76] J. H. Ryou and J. J. Gorman, "Mode selection for electrostatic beam resonators based on motional resistance and quality factor," *Journal of Applied Physics*, vol. 120, no. 21, 2016.

[77] N. Kacem, S. Hentz, D. Pinto, B. Reig, and V. Nguyen, "Nonlinear dynamics of nanomechanical beam resonators: improving the performance of nems-based sensors," *Nanotechnology*, vol. 20, no. 27, 2009.

[78] R. Azevedo and J. Lippmann, "Design of dual ended tuning fork resonators for roller bearing microstrain measurement," 2017.

[79] N. Badila-Ciressan, M. Mazza, D. Grogg, and A. Ionescu, "Fragmented membrane mem bulk lateral resonators with nano-gaps on 1.5 μm soi," in *European Solid State Device Research Conference (ESSDERC)*, 2007, pp. 430–433.

[80] M. A. Abdelmoneum, M. U. Demirci, and C.-C. Nguyen, "Stemless wine-glass-mode disk micromechanical resonators," in *IEEE International Conference on Micro Electro Mechanical Systems, (MEMS)*, 2003, pp. 698–701.

[81] M. Onoe, "Contour vibrations of isotropic circular plates," *Journal of the Acoustical Society of America*, vol. 28, no. 6, pp. 1158–1162, 1956.

[82] Y.-W. Lin, S. Lee, S.-S. Li, Y. Xie, Z. Ren, and C.-C. Nguyen, "Series-resonant vhf microme-chanical resonator reference oscillators," *IEEE Journal of Solid-State Circuits*, vol. 39, no. 12, pp. 2477–2491, 2004.

[83] M. A. Abdelmoneum, M. U. Demirci, and C. T. C. Nguyen, "Stemless wine-glass-mode disk micromechanical resonators," in *IEEE International Conference on Micro Electro Mechanical Systems (MEMS)*, 2003, pp. 698–701.

[84] G. Wu, D. Xu, B. Xiong, and Y. Wang, "A high q micromachined single crystal silicon bulk mode resonator with pre-etched cavity," *Microsystem technologies*, vol. 18, no. 1, pp. 25–30, 2012.

[85] W. Brantley, "Calculated elastic constants for stress problems associated with semicon-ductor devices," *Journal of Applied Physics*, vol. 44, no. 1, pp. 534–535, 1973.

[86] V. Kaajakari, T. Mattila, A. Oja, J. Kiihamaki, H. Kattelus, M. Koskenvuori, P. Rantakari, I. Tittonen, and H. Seppa, "Square-extensional mode single-crystal silicon microme-chanical rf-resonator," in *International Conference on Solid-State Sensors, Actuators and Microsystems, (TRANSDUCERS)*, vol. 2, 2003, pp. 951–954.

[87] S. Pala and K. Azgın, "A mems square chladni plate resonator," *Journal of Micromechanics and Microengineering*, vol. 26, no. 10, 2016.

[88] M. A. Hopcroft, W. D. Nix, and T. W. Kenny, "What is the young's modulus of silicon?" *Journal of microelectromechanical systems*, vol. 19, no. 2, pp. 229–238, 2010.

[89] V. L. Rabinovich, R. K. Gupta, and S. D. Senturia, "The effect of release-etch holes on the electromechanical behaviour of mems structures," in *International Conference on Solid-State Sensors, Actuators and Microsystems, (TRANSDUCERS)*, vol. 2, 1997, pp. 1125–1128.

[90] L. Shao and M. Palaniapan, "Effect of etch holes on quality factor of bulk-mode micromechanical resonators," *Electronics Letters*, vol. 44, no. 15, pp. 938–940, 2008.

[91] A. Ayon, K.-S. Chen, K. Lohner, S. Spearing, H. Sawin, and M. Schmidt, "Deep reactive ion etching of silicon," in *MRS Proceedings*, vol. 546, 1998, p. 51.

[92] N. D. B. Ciressan, C. Hibert, M. Mazza, and A. M. Ionescu, "Fabrication of silicon-on-insulator mem resonators with deep sub-micron transduction gaps," *Microsystem Technologies*, vol. 13, no. 11-12, pp. 1489–1493, 2007.

[93] M. M. López, E. A. Casu, W. A. Vitale, and A. M. Ionescu, "Solid-gap resonators based on pvdf-trfe," in *IEEE Silicon Nanoelectronics Workshop (SNW)*, 2016, pp. 72–73.

[94] M. Martarelli, "Exploiting the laser scanning facility for vibration measurements," Ph.D. dissertation, University of London, 2001.

[95] A. Cagliani, "High frequency bulk resonators for bio/chemical diagnostics and monitoring applications," Ph.D. dissertation, Technical University of Denmark, 2012.

[96] C.-S. Li, C.-H. Chin, Y.-C. Liu, and S.-S. Li, "Capacitively-driven and piezoresistively-sensed cmos-mems resonators," in *IEEE International Conference on Micro Electro Mechanical Systems (MEMS)*, 2012, pp. 539–542.

[97] J. E. Lee and A. A. Seshia, "Enhanced electrical characterization of mems resonators using on-chip parasitic feedthrough self-cancellation," in *EUROSENSORS*, 2008, pp. 1349–1352.

[98] A. Bulusu, A. Singh, C.-Y. Wang, A. Dindar, C. Fuentes-Hernandez, H. Kim, D. Cullen, B. Kippelen, and S. Graham, "Engineering the mechanical properties of ultrabarrier films grown by atomic layer deposition for the encapsulation of printed electronics," *Journal of Applied Physics*, vol. 118, no. 8, 2015.

[99] C. Curtis, L. Doney, and J. Johnson, "Some properties of hafnium oxide, hafnium silicate, calcium hafnate, and hafnium carbide," *Journal of the American Ceramic Society*, vol. 37, no. 10, pp. 458–465, 1954.

[100] C. Swenson, "Recommended values for the thermal expansivity of silicon from 0 to 1000 k," *Journal of Physical and Chemical Reference Data*, vol. 12, no. 2, pp. 179–182, 1983.

[101] V. Kaajakari, T. Mattila, A. Oja, and H. Seppa, "Nonlinear limits for single-crystal silicon microresonators," *Journal of Microelectromechanical systems*, vol. 13, no. 5, pp. 715–724, 2004.

[102] M. Agarwal, K. Park, R. Candler, M. Hopcroft, C. Jha, R. Melamud, B. Kim, B. Murmann, and T. Kenny, "Non-linearity cancellation in mems resonators for improved power-handling," in *IEEE International Electron Devices Meeting (IEDM)*, 2005, pp. 286–289.

[103] W.-T. Chang and C. Zorman, "Electrical characterization of microelectromechanical silicon carbide resonators," *Sensors*, vol. 8, no. 9, pp. 5759–5774, 2008.

[104] W.-C. Li, Y. Lin, B. Kim, Z. Ren, and C. T.-C. Nguyen, "Quality factor enhancement in micromechanical resonators at cryogenic temperatures," in *International Conference on Solid-State Sensors, Actuators and Microsystems, (TRANSDUCERS)*, 2009, pp. 1445–1448.

[105] M. U. Demirci and C. T.-C. Nguyen, "Mechanically corner-coupled square microresonator array for reduced series motional resistance," *Journal of Microelectromechanical Systems*, vol. 15, no. 6, pp. 1419–1436, 2006.

[106] H. Cho and D. E. Burk, "A three-step method for the de-embedding of high-frequency s-parameter measurements," *IEEE Transactions on Electron Devices*, vol. 38, no. 6, pp. 1371–1375, 1991.

[107] M. Koolen, J. Geelen, and M. Versleijen, "An improved de-embedding technique for on-wafer high-frequency characterization," in *Bipolar Circuits and Technology Meeting, 1991., Proceedings of the 1991*, 1991, pp. 188–191.

[108] L. F. Tiemeijer, R. M. Pijper, J. A. van Steenwijk, and E. van der Heijden, "A new 12-term open–short–load de-embedding method for accurate on-wafer characterization of rf

mosfet structures," *IEEE Transactions on Microwave Theory and Techniques*, vol. 58, no. 2, pp. 419–433, 2010.

[109] A. Brenes, J. Juillard, F. V. Dos Santos, and A. Bonnoit, "Characterization of mems resonators via feedthrough de-embedding of harmonic and subharmonic pulsed-mode response," *Sensors and Actuators*, vol. 229, pp. 211–217, 2015.

[110] J. Fritz, "Cantilever biosensors," *Analyst*, vol. 133, no. 7, pp. 855–863, 2008.

[111] K. Park, N. Kim, D. T. Morisette, N. Aluru, and R. Bashir, "Resonant mems mass sensors for measurement of microdroplet evaporation," *Journal of Microelectromechanical Systems*, vol. 21, no. 3, pp. 702–711, 2012.

[112] T. Choudhury and G. R. Biswal, "Sf 6 density-and-viscosity sensing in gas insulated switchgear using mems resonator," in *IEEE International Conference on Power Electronics, Intelligent Control and Energy Systems (ICPEICES)*, 2016, pp. 1–6.

[113] A. Cagliani and Z. J. Davis, "Ultrasensitive bulk disk microresonator-based sensor for distributed mass sensing," *Journal of Micromechanics and Microengineering*, vol. 21, no. 4, 2011.

[114] A. Hajjam, J. C. Wilson, and S. Pourkamali, "Individual air-borne particle mass measurement using high-frequency micromechanical resonators," *IEEE Sensors Journal*, vol. 11, no. 11, pp. 2883–2890, 2011.

[115] M. Konno, T. Ikehara, S. Murakami, R. Maeda, M. Kimura, T. Fukawa, and T. Mihara, "Novel mems oscillator using in-plane disk resonator with sensing platform and its mass sensing characteristics," in *International Solid-State Sensors, Actuators and Microsystems Conference (TRANSDUCERS)*, 2011, pp. 518–521.

[116] M. H. Zarifi and M. Daneshmand, "Bulk disc resonators radial and wineglass mode resonance characterization for mass sensing applications," *Microsystem Technologies*, vol. 22, no. 5, pp. 1013–1020, 2016.

[117] B. P. Harrington, R. Abdolvand, A. Hajjam, J. C. Wilson, and S. Pourkamali, "Thin-film piezoelectric-on-silicon particle mass sensors," in *IEEE International Frequency Control Symposium (FCS)*, 2010, pp. 238–241.

C.182

[118] H. S. Wasisto, S. Merzsch, A. Waag, E. Uhde, T. Salthammer, and E. Peiner, "Airborne engineered nanoparticle mass sensor based on a silicon resonant cantilever," *Sensors and Actuators*, vol. 180, pp. 77–89, 2013.

[119] J. Chaste, A. Eichler, J. Moser, G. Ceballos, R. Rurali, and A. Bachtold, "A nanomechanical mass sensor with yoctogram resolution," *Nature nanotechnology*, vol. 7, no. 5, pp. 301–304, 2012.

[120] K. Jensen, K. Kim, and A. Zettl, "An atomic-resolution nanomechanical mass sensor," *Nature nanotechnology*, vol. 3, no. 9, pp. 533–537, 2008.

[121] E. Gil-Santos, D. Ramos, J. Martínez, M. Fernández-Regúlez, R. García, Á. San Paulo, M. Calleja, and J. Tamayo, "Nanomechanical mass sensing and stiffness spectrometry based on two-dimensional vibrations of resonant nanowires," *Nature nanotechnology*, vol. 5, no. 9, pp. 641–645, 2010.

[122] Y. Yang, C. Callegari, X. Feng, K. Ekinci, and M. Roukes, "Zeptogram-scale nanomechanical mass sensing," *Nano letters*, vol. 6, no. 4, pp. 583–586, 2006.

[123] M. Hanay, S. Kelber, A. Naik, D. Chi, S. Hentz, E. Bullard, E. Colinet, L. Duraffourg, and M. Roukes, "Single-protein nanomechanical mass spectrometry in real time," *Nature nanotechnology*, vol. 7, no. 9, pp. 602–608, 2012.

[124] M. Tang, A. Cagliani, Z. J. Davis, and L. He, "Pulse mode actuation-readout system based on mems resonator for liquid sensing," in *IEEE International Conference on Nano/Micro Engineered and Molecular Systems (NEMS)*, 2014, pp. 216–219.

[125] Z. Hu, J. Hedley, N. Keegan, J. Spoors, W. Waugh, B. Gallacher, F.-X. Boillot, J. Collet, and C. McNeil, "Design, fabrication and characterization of a piezoelectric mems diaphragm resonator mass sensor," *Journal of Micromechanics and Microengineering*, vol. 23, no. 12, 2013.

[126] "Mass sensing with optomechanical oscillation," *IEEE Sensors Journal*, vol. 13, no. 1, pp. 146–147, 2013.

[127] R. A. Barton, B. Ilic, S. S. Verbridge, B. R. Cipriany, J. M. Parpia, and H. G. Craighead, "Fabrication of a nanomechanical mass sensor containing a nanofluidic channel," *Nano Letters*, vol. 10, no. 6, pp. 2058–2063, 2010.

[128] S. Schmid, M. Kurek, J. Adolphsen, and A. Boisen, "Detection of airborne nanoparticles with mechanical systems," 2013.

[129] B. Kim, Y. Lin, W.-L. Huang, M. Akgul, W.-C. Li, Z. Ren, and C.-C. Nguyen, "Micromechanical resonant displacement gain stages," in *IEEE International Conference on Micro Electro Mechanical Systems (MEMS)*, 2009, pp. 19–22.

[130] B. Choubey and A. McEwan, "On mass sensing using micro/nano resonators-approaches, challenges and directions," *International Journal On Smart Sensing and Intelligent Systems*, vol. 9, no. 1, pp. 1–20, 2016.

[131] K. Ekinci, Y. Yang, and M. Roukes, "Ultimate limits to inertial mass sensing based upon nanoelectromechanical systems," *Journal of applied physics*, vol. 95, no. 5, pp. 2682–2689, 2004.

[132] A. Heidari, Y.-J. Yoon, and H.-J. Choi, "Analysis and design of a high performance and low cost bio-mass sensor based on the radial contour mode disk resonator," *Microelectronic Engineering*, vol. 88, no. 8, pp. 1730–1732, 2011.

[133] J. Arcamone, G. Rius, G. Abadal, J. Teva, N. Barniol, and F. Pérez-Murano, "Micro-/nanomechanical resonators for distributed mass sensing with capacitive detection," *Microelectronic Engineering*, vol. 83, no. 4, pp. 1216–1220, 2006.

[134] A. Cagliani and Z. J. Davis, "Bulk disk resonator based ultrasensitive mass sensor," in *SENSORS*, 2009, pp. 1317–1320.

[135] T. Sharma, S.-S. Je, B. Gill, and J. X. Zhang, "Patterning piezoelectric thin film pvdf–trfe based pressure sensor for catheter application," *Sensors and Actuators*, vol. 177, pp. 87–92, 2012.

[136] G. A. Salvatore, D. Bouvet, I. Stolitchnov, N. Setter, and A. M. Ionescu, "Low voltage ferroelectric fet with sub-100nm copolymer p(vdf-trfe) gate dielectric for non-volatile

1t memory," in *European Solid State Device Research Conference (ESSDERC)*, 2008, pp. 162–165.

[137] G. D. Kolev, M. P. Aleksandrova, and K. H. Denishev, "Spray deposition of pvdf layers with application in mems pressure sensors," *International Journal of Reasoning-based Intelligent Systems*, vol. 5, no. 3, pp. 177–182, 2013.

[138] R. A. Schneider, "High-q aln contour mode resonators with unattached, voltage-actuated electrodes," Ph.D. dissertation, University of California, Berkeley, 2015.

Mobile: +41 78 878 50 69
Email: mariazel.maquedalopez@epfl.ch

Mariazel Maqueda López

Work Experience		
2013 - present		***EPFL, Switzerland***
<u>Doctoral researcher</u>		
MEMS Design and Modelling for Sensing Applications		
Microelectronics Test and Characterization		
Experience in Nanofabrication within a class 100 cleanroom		

June - Sept 2012	***IMEC, Leuven, Belgium***
<u>Internship</u>	
Analog Electronics Design	

June - Aug 2011	***LIONIX , Netherlands***
<u>Internship</u>	
Characterization of Capillarity Electrophoresis and Integrated Optics Systems	

March - Aug 2010	***Parque de las Ciencias , Granada, Spain***
<u>Internship</u>	
Multidisciplinary Scientific Guide	

Oct - Apr 2010	***CSIRC, Granada, Spain***
<u>Internship</u>	
Wired and Wireless Networks: Incidences Management and Web Design	

Education	
2013 - present	***EPFL, Switzerland***
Doctoral researcher in Micro-Systems and Micro-Electronics	

2012 - 2010	***Politecnico di Torino, Italy***
	Institut Polytechnique de Grenoble, France
	EPFL, Switzerland
Master in Nanotechnologies for ICTs.	

2010 - 2004	***University of Granada, Spain***
Bachelor and Master in Telecommunications Engineering	

Languages		
English	fluent
French	fluent
Italian	fluent
Spanish	first language

Extracurricular Activities

Piano, professional Conservatory of Music "Ángel Barrios", Granada, Spain;
Student Staff Team Leader in Conference Organization of Micro and Nano
Engineering (MNE) and European Solid-State Device Conference (ESSDERC)
in 2014 and 2016, respectively;
NGO Volunteer;

Journals

[1] M. Maqueda López, M. Fernández-Bolaños, W. A. Vitale and A. M. Ionescu, "Solid-Gap Wine-Glass Mode Disks VB-FET Resonators applied to biomass sensing", *Microelectronic Engineering,* vol. 145, pp. 53-57, 2015.

Conferences

[1] M. Maqueda López, M. Fernández-Bolaños and A. M. Ionescu "Solid-Gap Wine-Glass Mode Disks VB-FET Resonators applied to biomass sensing", *International Conference of Micro and Nano Engineering (MNE),* 2014.

[2] M. Maqueda López, E. A. Casu, V. A. Vitale and A. M. Ionescu, "Solid-Gap Resonators Based on PVDF-TrFE", *Silicon Nanoelectronics Workshop (SNW),* 2016.

[3] E. A. Casu, M. Maqueda López, W. A. Vitale, M. Fernández-Bolaños and A. M. Ionescu, "Design and Fabrication of High-K Filled Sub-100 nm Gap Resonators with Embedded Dielectric Field Effect Transistor for Ultra High Frequency Applications", *Silicon Nanoelectronics Workshop (SNW),* 2016.

[4] M. Fernández-Bolaños, W. A. Vitale, M Maqueda López et al., "3D TSV Based High Frequency Components for RF IC and RF MEMS Applications", *IEEE International 3D System Integration Conference*, 2016.

[5] M. Maqueda López, E. A. Casu, A. M. Ionescu and M. Fernández-Bolaños, "Partially-filled HfO2 gap Double-Ended Tuning Fork MEMS resonators for enhanced sensing applications", *European Frequency and Time Forum and International Frequency Control Symposium (EFTF-IFCS)*, 2017 (Accepted).

[6] M. Maqueda López, E. A. Casu, M. Fernández-Bolaños and A. M. Ionescu, "Low Impedance ALD HfO2 Partially-Filled-Gap Flexural and Bulk MEMS Resonators Piezoresistively Detected for Distributed Mass Sensing", *EUROSENSORS*, 2017 (Accepted).

[7] E. A. Casu, W. A. Vitale, M. Tamagnone, M. Maqueda López et al., "Shunt Capacitive Switches Based on VO2 Metal Insulator Transition for RF Phase Shifter Applications", *European Solid-State Device Research Conference (ESSDERC)*, 2017 (Accepted).

C.190